DYNAMICS OF ORIENTABLE PARTICULATE SUSPENSIONS
CONTINUUM SIMULATIONS OF 'LIVING' FLUIDS
AND
MESO-SCALE SIMULATIONS OF ANISOTROPIC PARTICLE SUSPENSIONS

A Thesis

Presented to the Faculty of the Graduate School

of Cornell University

in Partial Fulfillment of the Requirements for the Degree of

Master of Science

by

Ling Qi

May 2014

© 2014 Ling Qi

ABSTRACT

Two simulation techniques that are used to approach two very different suspension problems – continuum scale ‘active fluids’ contain living cells that can respond to external stimuli such as light; and passive fluids contain anisotropic particles whose size is small enough that non-continuum effect caused by solvent needs to be accounted for.

In the first part, instability caused by hydrodynamic interaction between the living cells is probed by Fluid Particle Dynamics (FPD). In the second part, Coarse-Grained Molecular Dynamics (CGMD) simulation is applied to investigate the relation between microstructure of the suspension, such as orientation distribution function, particle moments to its rheological behavior, such as shear viscosity.

BIOGRAPHICAL SKETCH

Ling Qi has joined Chemical and Bimolecular Engineering department in Cornell University since Spring 2012. Prof. Donald Koch is her thesis advisor. She has studied dynamic behavior of orientable particulate suspensions with two simulation techniques. Her thesis is composed of two projects: one is to use coarse-grained molecular dynamics simulation to study the relation between microstructure and rheological properties of suspensions containing anisotropic particles; the other project is a continuum scale simulation which was used to study the behavior of 'living fluids'.

During her studies, she has been exchange scholar funded by CNRS (Centre national de la recherche scientifique) for four months, where she studied a continuum scale simulation technique to investigate the dynamic behavior of suspension containing living cells. This research was performed at LIPhy (Laboratoire interdisciplinaire de Physique), Joseph-Fourier University, Grenoble, France .This study was under the guidance of Prof. Philippe Peyla, and Dr. Salima Rafai. She has presented this work to 22nd Congress of the French Physics Society (SFP,2013) ; she was also awarded scholarship from Ecole Doctrale de Physique.

Ling Qi has been teaching assistant for polymeric materials for one semester.

Ling Qi earned her Bachelor of Science degree in Polymer and Textile Engineering in 2006 from Shanghai DongHua University. Her undergraduate research focused on understanding the crystallinity and what its impact on mechanical performance in porous fibrous medium.

During her undergraduate period, Ling has been awarded excellent academic awards, outstanding senior thesis.

Ling has been working for Corning Inc. as process modeling engineer since December, 2013.

To My Beloved Parents, Huili Sun, Zhi Qi

ACKNOWLEDGMENTS

My endless gratitude goes to my beloved family, my parents, who has never gave up faith on me, and supported me strongly both emotionally and financially.

I appreciate Dr.Yong Joo for offering me the opportunity to study in the Dept. of Chemical and Biomolecular Engineering. I also thank him for proposing the idea of CGMD, and for his patient guidance on transiting me from an experimentalist to a computationalist.

I am always deeply grateful to Dr. Donald Koch, for his consistently insightful discussion and inputs; for him unselfishly sharing his time in guiding me, for him being supportive for the research topic that I am interested in, for his extreme patience to explain every single concept that I had difficulty to understand. His attitude on carrying out excellent work always impressed me and exemplified me – it is very much like the process of creating an art piece. I thank him for taking me as him student, and thank him being such a great role model in my professional life. I feel so lucky to have met him in my life.

I also thank Dr. Paulette Clancy for being on my committee and provide very helpful comments on my thesis writing. I also thank her for being very supportive and understanding on professional development. Her leadership as a great woman role model enlightens my life.

I am very grateful to Dr. Matt DeLisa, for him being very supportive and helping me deal with difficult situations, and providing guidance on professional choices.

I thank Dr. Philippe Peyla, for his offering the opportunity to allow me to conduct research in an excellent institute abroad. I also thank him and his colleage Salima Rafai, for their consistent

guidance on my project, and for their strong support for my career development. Thanks CNRS for providing sufficient funding for me to conduct this period of research.

I thank my colleagues, Dr. An-Cheng Ruo, Sushmit Goyal, Bryan Rolfe, Hideyuki for their generous sharing of time in providing me constructive and concrete advice to help me get over the technical difficulties in my work. I also appreciate the discussion held with Dr. Jean-Louis Barrat and the very insightful comments he provided to my work.

Life without friends' accompanying is always not a colorful one – I thank my friends and colleagues, Kasyap, Hsiu-yu, Thomas, Hideyuki, Matthieu, Angela, Thibault, Olivier, Jian, Xiaohua, Haiyi, Sai Pooja, Poornima, Ashley, Vikram, Arijit, Mukul, Anubhab for their fun time, insightful conversations, for their exampling their strong working ethics and being my role models.

Life is a series of coincidences – I am thankful for the conversations held with Dr. Claude Cohen, Dr. Abraham Stroock, who inspired me thinking and whose thoughts lasted long time impression on my life.

Finally, to all those who have ever helped me, encouraged me, no matter on to personal life, or to my professional life, I thank you, for your appearances in my life that make it nicer.

TABLE OF CONTENTS

LIST OF FIGURES

LIST OF TABLES

1 DYNAMICS OF ANISOTROPIC PARTICLE SUSPENSION BY COARSE-GRAINED MOLECULAR DYANMICS

1.1 Introduction

The presence of prolate-shaped materials ranges from liquid crystal molecules, tobacco mosaic virus molecule to nano-rods, and rod-like glass fibers. Suspensions of these anisotropic molecules or particles have a variety of technological applications and significance. Owing to their anisotropy, they are capable of being involved in self-assembly processes leading to complex structures. [1–4] Moreover, this anisotropy has been taken advantage of in order to contribute to the performance attributes of products manufactured from these suspensions. Examples of these products include enhanced mechanical performance in fiber-reinforced composites,[5] and electronic displays made from liquid crystals[6]. The emergence of nanotechnology has also prompted the use of nano-rods in various emerging nano-scale electronic devices, such as solar cells, [7] field-effect transistors,' ultraviolet photo-detector, [8] and ultra-bright light-emitting diodes [9]. These nano-rods can be elongated particles made from zinc oxide or gold, whose aspect ratio is in the range 3-5 and size ranges from 1-100 nm. [10]

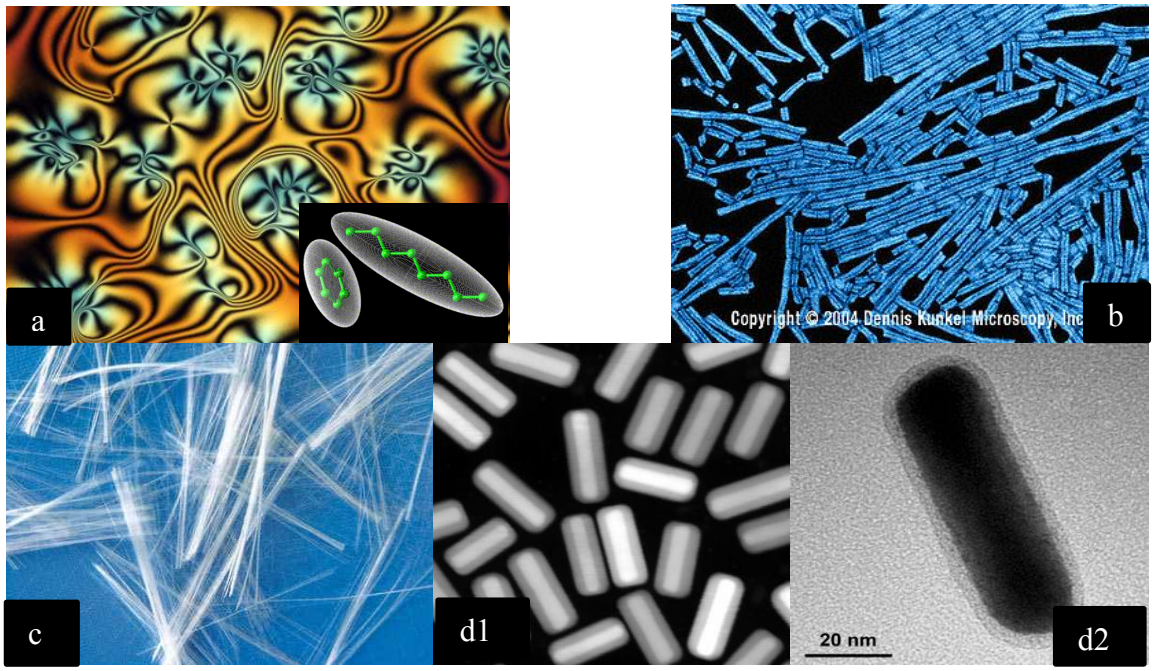

Figure 1-1 Examples of anisotropic particles. a) liquid crystal b) tobacco mosaic virus c) glass fiber d1, d2) nano-rod

Control of the structure and flow properties of suspensions is often vital to the commercial success of the product or of its manufacture. The ability to transform a liquid, moldable suspension into a solid-like one that retains its shape when removed from the mold is crucial to the success of the processing. Due to its anisotropy, particle motion and suspension rheology is

largely determined by particle orientation distribution, even in the dilute regime.

The orientation distribution in anisotropic particle suspensions is especially important in controlling transport properties in the final product; the orientation also contributes additionally to the viscosity. Bricker and Butler[11] compared relative viscosity of spheres to that of prolate spheroids with two aspect ratios at same volume fraction and found an obvious increase in viscosity for prolate spheroids case. In this study, prolate spheroids were made from polystyrene. The length of the spheroid particles is about 2~3 μm, the width is about 0.55~0.65μm. This study clearly indicates that with the same volume fraction, the one more degree of freedom, orientation, which is induced by particle anisotropy, alters the flow behavior much more significantly than the non-orientable ones. This experimental study is used in this work to compare simulation results to experiment.

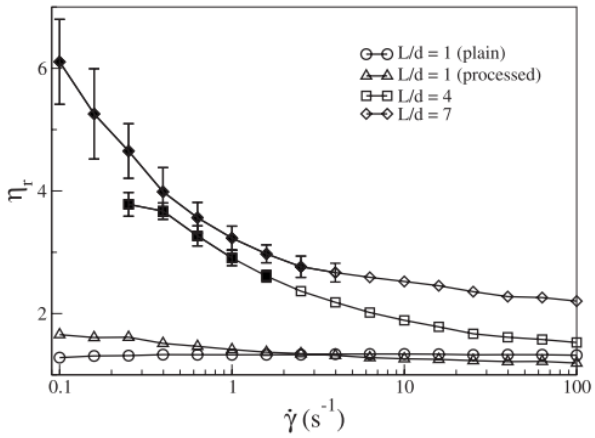

Figure 1-2 Relative viscosity as a function of shear rate and aspect ratio at volume fraction ~ 0.07 for different suspension systems. Adapted from original work[11].

In Butler's work, it is observed that shear thinning of particulate suspension exists for four orders of magnitude, while for suspensions containing similar loading of spheres, shear thinning lasts for less than one order of magnitude.

In this work, our interest is to understand the relation between microstructure and rheology, and to further explicate the origin of shear-thinning in rod-like particle suspensions. Over the past decades, tremendous efforts in research have been made to understand the relation between rheology and its microstructure, in terms of theory, [12,13] simulation,[14–17] or experiments. [18–20] However, shortcomings from theory and experiments largely prevented this problem to be well-addressed. In terms of theory, underlying assumptions usually facilitates understanding in extreme scenarios rather than moderate particle geometry;[12,21] Experimental research on the other hand often times call for sophisticated techniques to establish a direct visualization between bulk flow behavior and microstructure. [19,22] Fortunately, with the aid of computational research, the relation between microstructure and flow behavior has been well studied. [17,23] Nevertheless, the prevailing computational research dealing with suspension problems where a clear separation exists in the length scale of the particles and the solvent. As such, it allows one to treat the solvent as a continuum. As the size of the particles scales down to the point where this clear separation is no longer very distinct, knowledge of the non-continuum effect on the rheology of particulate suspensions is needed. Due to the need to approach this limit, we adopted a statistical mechanical approach, coarse-grained molecular dynamics (CGMD), to probe the dynamics of a suspension containing rod-like particles. Due to the fact that the length scale of the particles is comparable to that of solvent molecule, CGMD allows one to treat the solvent in an explicit manner. The necessity of treating the background solvent medium explicitly is demonstrated by In't Veld et al.[24]

As the microstructure of a suspension is a complicated function of particle geometry (aspect ratio, shape, and polydispersity), particle volume fraction, particle interaction, Brownian and hydrodynamics forces, the advantage of using CGMD to address this problem is at least two-

fold. First, the flexibility in varying experimental conditions with no raw-material input means that the shape and size can be well-defined based on the length scale of the introduced solvent model, hence avoiding the poly-dispersity issue usually associated with empirical research. Similarly, the effect of the suspending medium on rheology can be finely resolved when treating the solvent medium explicitly since volume fraction can be varied easily. If in need, the interparticle interaction can be tuned such that it is geared toward certain aggregational states. [25] Secondly, the power of CGMD also allows one to access microscopic particle information, which can be used to explain the rheological behavior of suspensions.

In the following text, I will briefly review some of the efforts that have been carried out in terms of theory, simulation, and experiments to address the orientation distribution problem with regarding to its rheology.

Theoretical studies on the suspension rheology problem begin with dilute systems with non-interacting particles. To account for the contribution to local viscosity from particle orientation, Jeffery[13] first analytically solved the motion of a single prolate spheroid in a viscous fluid subject to a shear flow. The specific orientation trajectory of orientation is known as the Jeffery orbit.

In the absence of Brownian motion, the orientation distribution function for force-free, torque-free particles in simple shear flow has been computed. [26]. In the circumstances where only weak Brownian motion exists, Leal and Hinch studied the orientation distribution function of dilute suspensions with weak Brownian motion, where they found that a stochastic contribution affects the orientation distribution through small shifts in the orbits of the particles. [27] Eventually a steady- state orientation distribution is established after the Brownian motion and hydrodynamic effect reach equilibrium. In their following work, [12] where stronger Brownian motion is taken

into account, Brownian stress and viscous stress can be computed based on the average particle orientation.

For spheroidal particles, the equation for the stress tensor contains an elastic term from Brownian motion:

$$\boldsymbol{\sigma^e} = 3\left(\frac{p^2-1}{p^2+1}\right)\boldsymbol{\nu} k_B T < \boldsymbol{uu} > \qquad 1\text{-}1$$

The viscous stress has been given by Hinch and Leal [28] as

$$\boldsymbol{\sigma^v} = 2\eta_s\phi\,\{A < \boldsymbol{uuuu} > : \boldsymbol{D} + B[< \boldsymbol{uu} > \cdot \boldsymbol{D} + \boldsymbol{D} \cdot < \boldsymbol{uu} >] + C\boldsymbol{D}\} \qquad 1\text{-}2$$

where the coefficients A, B, and C depend on the particle aspect ratio, p. $\boldsymbol{D}$ represents symmetric strain rate tensor. $\boldsymbol{u}$ represents orientation of axis of symmetry and $\boldsymbol{\nu}$ being number density of suspension. Brownian stress relaxes gradually, as flow-induced orientation disappears by Brownian motion, while viscous stress goes to zero immediately when flow ceases. The stress from the Newtonian solvent is given by $\boldsymbol{\sigma^s} = 2\eta_s\boldsymbol{D}$. Hence the total stress is the sum of the elastic and viscous contributions, as well as that from the Newtonian solvent $\boldsymbol{\sigma} = \boldsymbol{\sigma^e} + \boldsymbol{\sigma^v} + \boldsymbol{\sigma^s}$.

There is a long-standing interest to relate bulk phenomena with microstructural information. In terms of experiments, Stover and Cohen, [19] and Iso and Cohen [18] observed semi-dilute fiber suspensions in both Newtonian and non-Newtonian fluids subject to a simple shear flow. Their work provided experimental evidence of fiber orientation under the control of a dynamic process. Moreover, they elucidated the factors that control the structure in theoretical predictions of fiber suspensions. Petrich and Cohen[20] have established a relationship between stress and

microstructure in experiments of fiber suspensions. Jogun[29] has studied shear rate- dependent orientation distribution of suspensions containing plate-like particles of aspect ratio of 10-12 up to a volume fraction of 0.39.

Scientific interest has also steered researchers toward exploring the microscopic origin of rheological phenomenon, such as shear thinning and shear thickening associated with colloidal suspensions through direct visualization. [30,31] For sphere case, very recent work reported by Xu and Cohen employed confocal microscopy technique to image the microstructure associated with shear thinning. [22] Recent work reported by Xu and Dinner [32] used a Stokesian dynamics simulation with a non-equilibrium umbrella sampling technique and found a strong correlation between shear thinning and a two-particle measure of the shear stress.

Computational simulation has contributed greatly to suspension problems. Typical methods include Stokesian dynamics, [15,17] Brownian dynamics,[33] the Lattice Boltzmann method, and dissipative particle dynamics.[14] Claeys and Brady [34] studied suspensions of spheroidal particles in Stokes flow by Stokesian dynamics; Yamane and Dio[35] studied a semi-dilute suspension of non-Brownian rod particles by numeric simulation. The viscosity of a dilute suspension of rod-like particles has been numerically studied by Yamamoto and Matsuoka. [36]

Löwen studied spherocylinder particle of moderate aspect ratio (4-6) by Brownian dynamics.[37] Dynamic problems approached through molecular dynamics so far to our knowledge are by Grest group, where they have explicitly treated solvent and studied the rheological behavior of suspensions contain sphere particles.[24] The novelty of our study is that not only we take into account both Brownian forces and hydrodynamic interaction, but we can also address suspensions that contain non-spherical particles, of which the solvent effect has to be treated explicitly as the continuum approximation is no longer valid. With the power of molecular

dynamics that allows one to access to molecule information, one can then utilize these microscopic information and explain the observed flow behavior by relating to its microstructure.

To fulfill our research interest, we need to create a prototype system with a homogeneous dispersion state at equilibrium by avoiding particle-particle interactions. This goal is going to be implemented by assigning interaction potential in a certain manner that results in a zero Hamaker constant within the suspension. In the current work, the Hamaker constant is not yet zero. Note, however, a depletion interaction might still cause some attraction even though the van der Waals attraction between the particles has been avoided.

1.2 Methodology: Coarse-Grained Molecular Dynamics

1.2.1 Brief Introduction to Molecular Dynamics

1.2.1.1 Equations of Motion and Verlet Algorithm

In Molecular Dynamics simulations, the motion of molecules is generally represented by Newton's equations of motion. For a single molecule *i*, whose mass is denoted as m_i, and the force acting on molecule *i* by the ambient molecules denoted by $\boldsymbol{f_i}$, then the translational motion of that molecule can be described by Newton's equation of motion:

$$m_i \frac{d^2 \boldsymbol{r_i}}{dt^2} = \boldsymbol{f_i} \qquad 1\text{-}3$$

The rotational motion of that molecule is governed by the torque $\boldsymbol{\tau_i}$ about the centre of mass, and it is simply defined

$$\boldsymbol{\tau_i} = \sum_a (\boldsymbol{r_{ia}} - \boldsymbol{r_i}) \times \boldsymbol{f_{ia}} = \sum_a \boldsymbol{d_{ia}} \times \boldsymbol{f_{ia}} \quad \text{1-4}$$

Here $\boldsymbol{f_{ia}}$ is the force acting on sites $\boldsymbol{r_{ia}}$ in the molecule. $\boldsymbol{d_{ia}}$ is the positions of atoms relative to the molecular center of the mass. In LAMMPS, this calculation is activated by imposing a rigid body constraints on the subparticles that compose the molecule.

If a system is composed of N particles, then there are N sets of similar equations, and the motion of N molecules interacts through forces acting among all the molecules in the system.

To solve this differential equation, we expand the second-order differential term into an algebraic expression using a Taylor series expansion with a time increment equal to *h*, referred to as the "time step" in the simulation.

$$x(t+h) = x(t) + h\frac{dx(t)}{dt} + \frac{1}{2!}h^2\frac{d^2x(t)}{dt^2} + \frac{1}{3!}\frac{d^3x(t)}{dt^3} + \ldots \quad \text{1-5}$$

In a similar fashion, the motion can be also expanded into another form that moves the system backwards in time by the same time step, h:

$$x(t-h) = x(t) - h\frac{dx(t)}{dt} + \frac{1}{2!}h^2\frac{d^2x(t)}{t^2} - \frac{1}{3!}h^3\frac{d^3x(t)}{dt^3} + \ldots \quad \text{1-6}$$

To acquire the second-order differential term, we can sum these two equations to remove the first- and third-order differential terms, and the second-order differential term can be solved as

$$\frac{d^2x(t)}{dt^2} = \frac{x(t+h) - 2x(t) + x(t-h)}{h^2} + O(h^2) \quad \text{1-7}$$

This equation is of second-order accuracy.

With this so-called "central difference" approximation, we can express the *x*-component of Newton's equation of motion of a particle that is located at $\boldsymbol{r_i} = (x_i, y_i, z_i)$, acted upon by a force $\boldsymbol{f_i} = (f_{xi}, f_{yi}, f_{zi})$ in this way,

$$x_i(t+h) = 2x_i(t) - x_i(t-h) + \frac{h^2}{m_i} f_{xi}(t) \qquad 1\text{-}8$$

Similar equations can be expressed in the same way for the other two Cartesian components of the particle's motion. If a system is composed of *N* particles, then there are *3N* algebraic equations to specify the motion of molecules.

Hence, with this scheme, the molecule's position at the next time step can be evaluated from the current and the previous step in combination with the requisite forces at the current step, leading to second-order accuracy.

1.2.1.2 Interaction Potential: Lennard-Jones Potential

In order to determine the forces in a Molecular Dynamics simulation, we require a description for the underlying intermolecular interactions in the form of a potential model. Here, we introduce the one of the most commonly used potentials in Molecular Dynamics simulations, namely the Lennard-Jones potential. As simple as its expression is, it can nevertheless capture the essential interaction taking place between a pair of molecules as:

$$U_{ij} = 4\varepsilon \left[\left(\frac{\sigma}{r_{ij}} \right)^{12} - \left(\frac{\sigma}{r_{ij}} \right)^{6} \right] \qquad 1\text{-}9$$

where σ is a length-scale parameter represents the particle diameter, ε the energy scale parameter, and r_{ij} the separation distance between molecules.

Figure 1-3 represents the Lennard-Jones potential, in which U_{ij} and r_{ij} is non-dimensionalized by ε and σ.

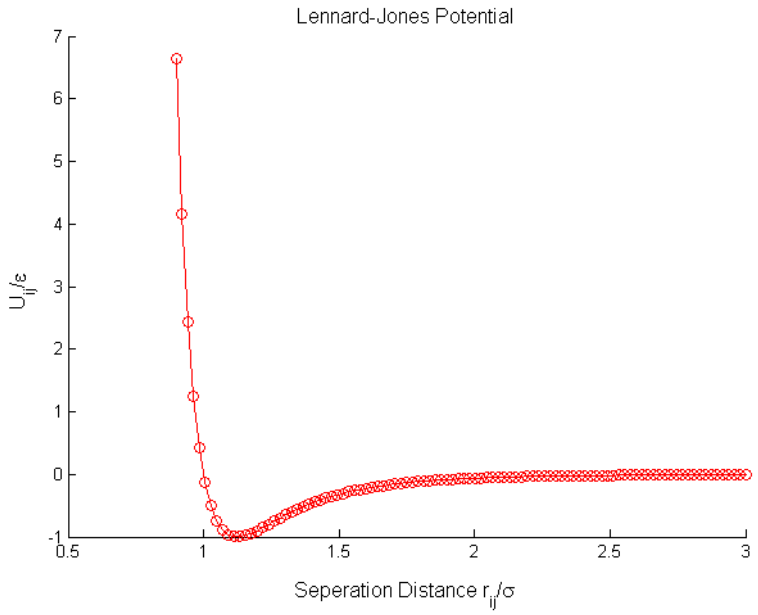

Figure 1-3 Lennard Jones Potential

There are a few distinct features about this potential:

- In the range of r $\leq \sigma$, this very steep potential causes particles to strongly repel each other.
- The potential minimum occurs at $2^{\frac{1}{6}}\sigma$, and U_{min} = - ε**,** where the repulsive force and attractive force cancels out.
- Beyond the potential minimum, the particles start to interact with attractive potential.
- As $r \to \infty$, as the potential decays as r^{-6}, U is asymptotic to zero.

1.2.1.3 Force Evaluation

Suppose we need to compute the x-component of the interaction force due to the contribution of the potential,

$$f_x(r) = -\frac{\partial U(r)}{\partial x} = -\left(\frac{x}{r^2}\right)\left(\frac{dU(r)}{dr}\right) \quad \text{1-10}$$

For a Lennard-Jones system, in reduced units, this can be written as:

$$f_x(r) = \frac{48x}{r^2}\left(\frac{1}{r^{12}} - 0.5\frac{1}{r^6}\right) \quad \text{1-11}$$

1.2.1.4 Boundary Conditions

1.2.1.4.1 Equilibrium – Periodic Boundary Conditions

It is, of course, ideal to study a system that includes the actual number of particles in the real physical system that we wish to represent. However, computation-wise, it is unrealistically expensive to do so. Hence, the use of periodic boundary conditions allows us to perform a simulation with a relatively small amount of particles that represent the behavior of much larger systems. The main idea behind periodic boundary conditions that fulfills this requirement is that, as a particle leaves the main simulation box, an image of this particle enters the simulation box at an equivalent position on the other side of the box to replace the leaving one. This conserves the number of particles in the simulation box.

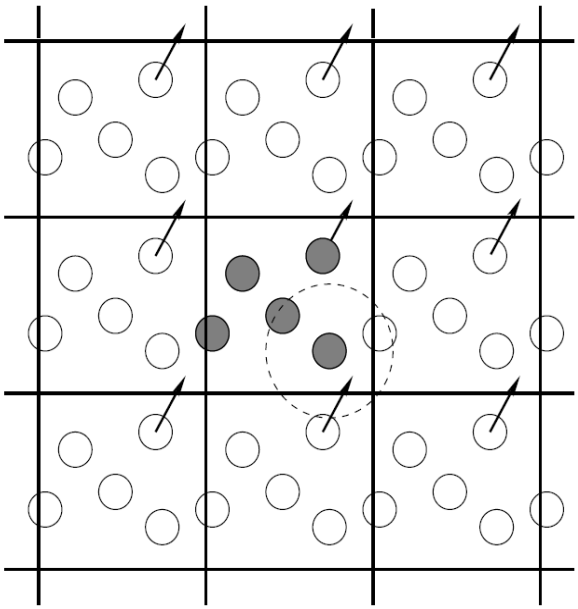

Figure 1-4 Schematic drawing of periodic boundary conditions

1.2.1.4.2 Under shear : Lees-Edwards Boundary Conditions

While periodic boundary conditions are useful for molecular simulations of a system intended to represent thermodynamic equilibrium, for a system under shear, we also need to take into account the velocity gradient induced by the shear flow. Take simple shear flow as an example; the velocity profile varies linearly from $-U$ at the lower boundary to U at the upper boundary. In generating such a flow profile in Molecular Dynamics simulation, the upper- and lower-replicated simulation boxes, are made to slide in different directions with a constant speed. This sliding boundary conditions is the so-called 'Lees-Edwards boundary condition. Figure 1-6 depicts the concept of this boundary condition: replicated boxes in the upper and lower layers slide in each direction by a distance, ΔX. If particles move out of the simulation box normal to the x-axis, they return into the simulation box through the opposite boundary, in a similar manner to periodic boundary conditions.

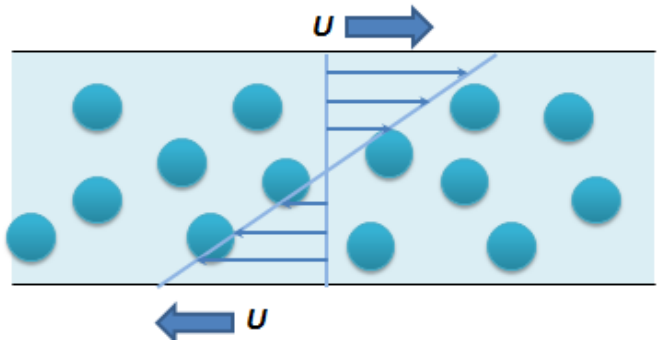

Figure 1-5 Schematic drawing of a simple shear flow

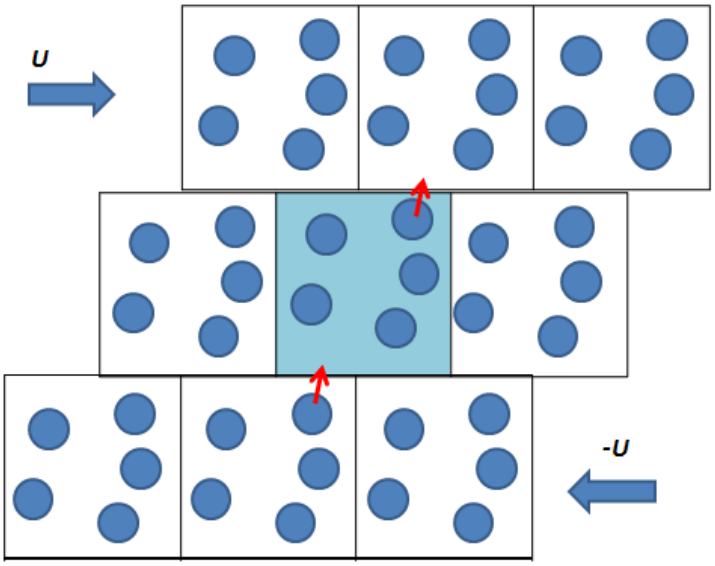

Figure 1-6 Schematic drawing Lees-Edwards boundary conditions

However, if the particles cross the boundary normal to the *y*-direction, the same treatment of the periodic boundary condition is applied to the *y*-coordinate of such particles, but the *x*-coordinate should be shifted from *x* to *(x - ΔX)*. In addition, the *x*-component v_x of these particles needs to be modified to $(v_x - U)$, but the *y*-component v_y can be used without modification.

1.2.1.5 Reduction in Computation Time

1.2.1.5.1 Cut-off Distance

In the course of a traditional Molecular Dynamics simulation, the most time-consuming procedure is invariably the calculation of forces between particles. For a system containing N particles, the calculation scales as $\sim N^2$. Fortunately, many particle-particle potentials exhibit short-range order. As the interaction energy decays very rapidly with the particle-particle separation over a distance only several times the particle diameter, it is reasonable to consider interactions only within this range. This introduces the concept of a "cut-off" distance after which the force is zero. Considering the Lennard-Jones potential as a typical example.,we can estimate how fast $U(r)$ decays, noting that $U(r = 2.5\sigma) = -0.0163\ \varepsilon$, $U(r = 3\sigma) = -0.00548\varepsilon$, and $U(r = 3.5\sigma) = -0.00217\ \varepsilon$. Thus, since the energy at a cut-off 2.5 times the collision diameter has fallen to just 1% of its maximum attractive value at epsilon, cut-off values of this order are typically employed.

1.2.2 Coarse-Graining: The concept

In traditional Molecular Dynamics, the typical length scale associated with atomic motion is of the order of 1 $\dot{A}$, and the typical time step is around 0.1 picosecond for simple systems (but frequently less than this, around 1 fs, for more complex molecular systems). With detailed information regarding position, velocity, and force as a function of time provided by Molecular Dynamics simulations, one can relatively easily calculate a wide variety of thermodynamic and kinetic properties. Molecular Dynamics is especially useful in its ability to approach local problems, for example inhomogeneities, defects and clustering configurations, that are not easily

accessible by physical macroscopic measurements in a lab frame. However, on the other hand, the very small length scale and short time scale make this method cumbersome if not impossible to study properties that require a very long time to equilibrate, such as viscosity. This has led to the idea of "coarse-graining" the system to remove some of the explicit so-called "all-atom" representations in an effective manner to retain the advantages of traditional Molecular Dynamics, but to offset the disadvantages of this method by enlarging the length- and time-scales that can be represented.

Let us compare an all-atom model to a coarse-grained model to see its advantage in effectively increasing length- and time- scales. If we define R to be the degree of coarse-graining, where $\boldsymbol{R}$ represents the number of molecules that are included in one coarse-grained "bead," then the length scale $L \sim R$, and the time scale, $\Delta t = L\sqrt{\frac{m}{kT}} \sim R^{1.5}$.

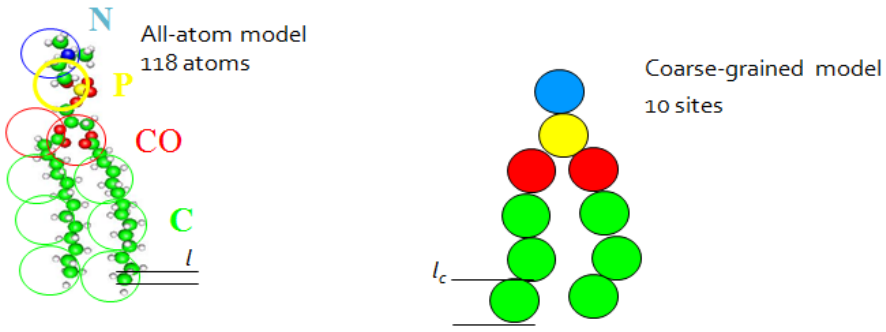

Figure 1-7 Coarse-graining concept: from an all-atom model to a coarse-grained model

Table 1-1 lists the increments in both length- and time- scales comparing an all-atom model to a coarse-grained model applied to cases involving a polymer molecule and water molecules.

Table 1-1 Comparison in time and length scale

Type	Length-scale ($\dot{A}$)	Time-scale $\times 10^{-12}$ sec
Atoms	1	0.1
Poly-styrene(PS)	17.18	19.4
Poly-Isoprene(1,4 PI)	8.22	5.56

1.3 Benchmark Validation

The LAMMPS Molecular Dynamics Simulator developed by Sandia National Lab [38] is employed in this work. In order to validate the applicability of this simulator, I reproduced Vibha Kalra's published work, who was a PhD students a benchmark check. In this reproduction study, good agreement was obtained between their original work and the results described here.

1.3.1 Reproduction work - Effect of shear on nanoparticle dispersion in polymer melts: A Molecular Dynamics Study [25]

1.3.1.1 Validation on potential computation by LAMMPS

A custom potential was employed for nanoparticle interaction in the original work; its expression is as follows:

$$
\begin{aligned}
u^{\mathrm{ATT}}[k] &= 4\varepsilon\left[\left(\frac{\sigma}{r}\right)^{12}-\left(\frac{\sigma}{r}\right)^{6}\right]+ecut, \quad r \le 2^{1/6}\sigma \\
&= k^{*}\left\{4\varepsilon\left[\left(\frac{\sigma}{r}\right)^{12}-\left(\frac{\sigma}{r}\right)^{6}\right]+u^{\mathrm{LJ}}(2.5)\right\}, \\
& 2^{1/6}\sigma \le r \le 2.5\sigma \\
&= 0, \quad r > 2.5\sigma,
\end{aligned}
\qquad \text{1-12}
$$

There is no such exact potential expression in LAMMPS package, but the 'table' potential allows one to explicitly tabulate a custom potential at each point of interest. Figure 1-8 shows the good agreement we obtained between a LAMMPS- tabulated potential to its analytical form in the original work.

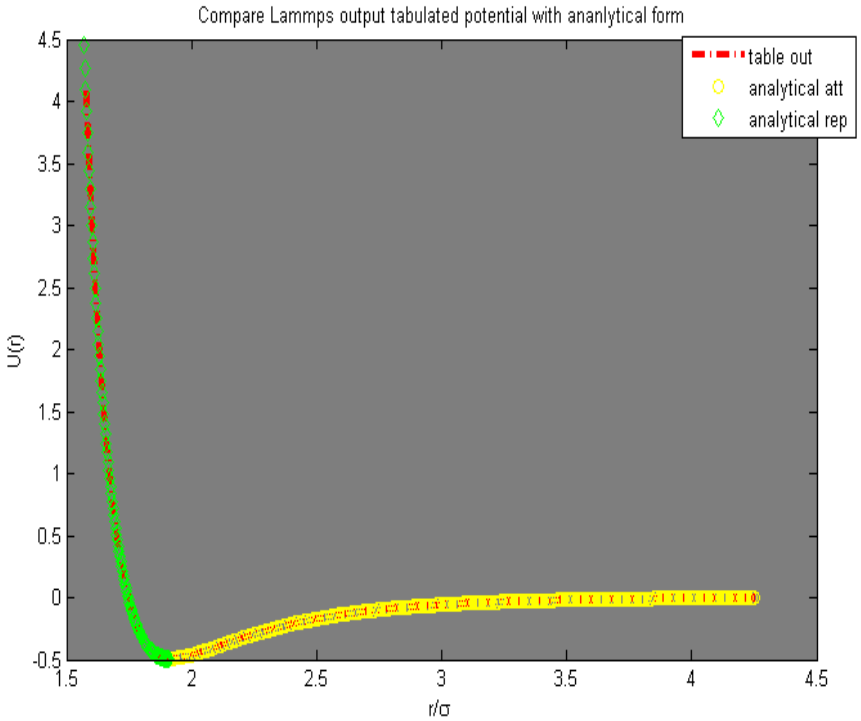

Figure 1-8 Analytical expression and LAMMPS tabulated potential

1.3.1.2 Effect of shear on suppression the onset of nanoparticle clustering

In the original work, shear is found to be an effective tool to distribute the nanoparticles randomly by suppressing the formation of clusters caused by the attractive potential used. Comparing $\dot{\gamma} = 0.1$ to the case where $\dot{\gamma} = 0$, it is found that a high shear rate is effective in suppressing the clusters even after only 3000 MD time units.

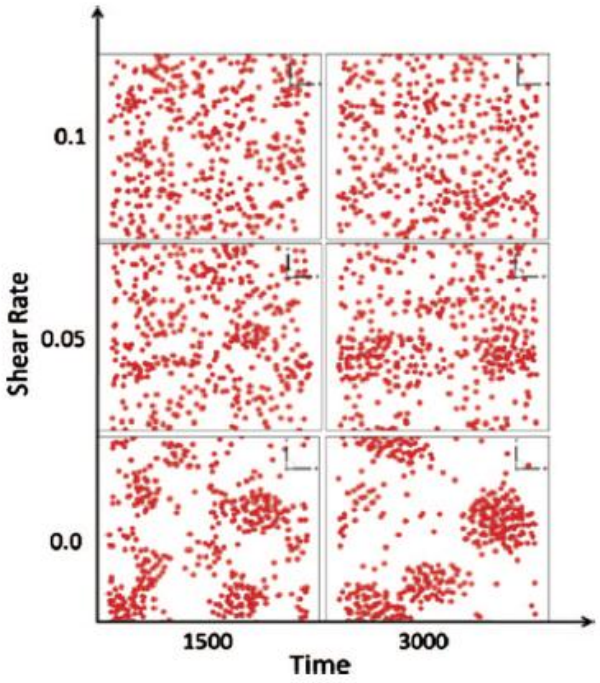

Figure 1-9 Snapshots of nanoparticle placement from original work [25]

In order to further validate the reproduction of this earlier published work, we computed the radial distribution function G(r) of nanoparticles as a quantitative analysis for the local clustering configurations. As shown in Figure 9, it is found from both original work and the reproduction study here that, in the zero shear case, there is an increment in the second peak of G(r) which provides strong evidence for the formation of clusters. When the shear rate is elevated even to a moderate value, the increment of second peak in G(r) is no longer as distinct as in the zero shear case.

This effect can be well reproduced under the same conditions, as shown in the snapshots shown in Figure 1-10. The local configuration from these snapshots is visually comparable to the quantitative analysis obtained from the radial distribution function. .

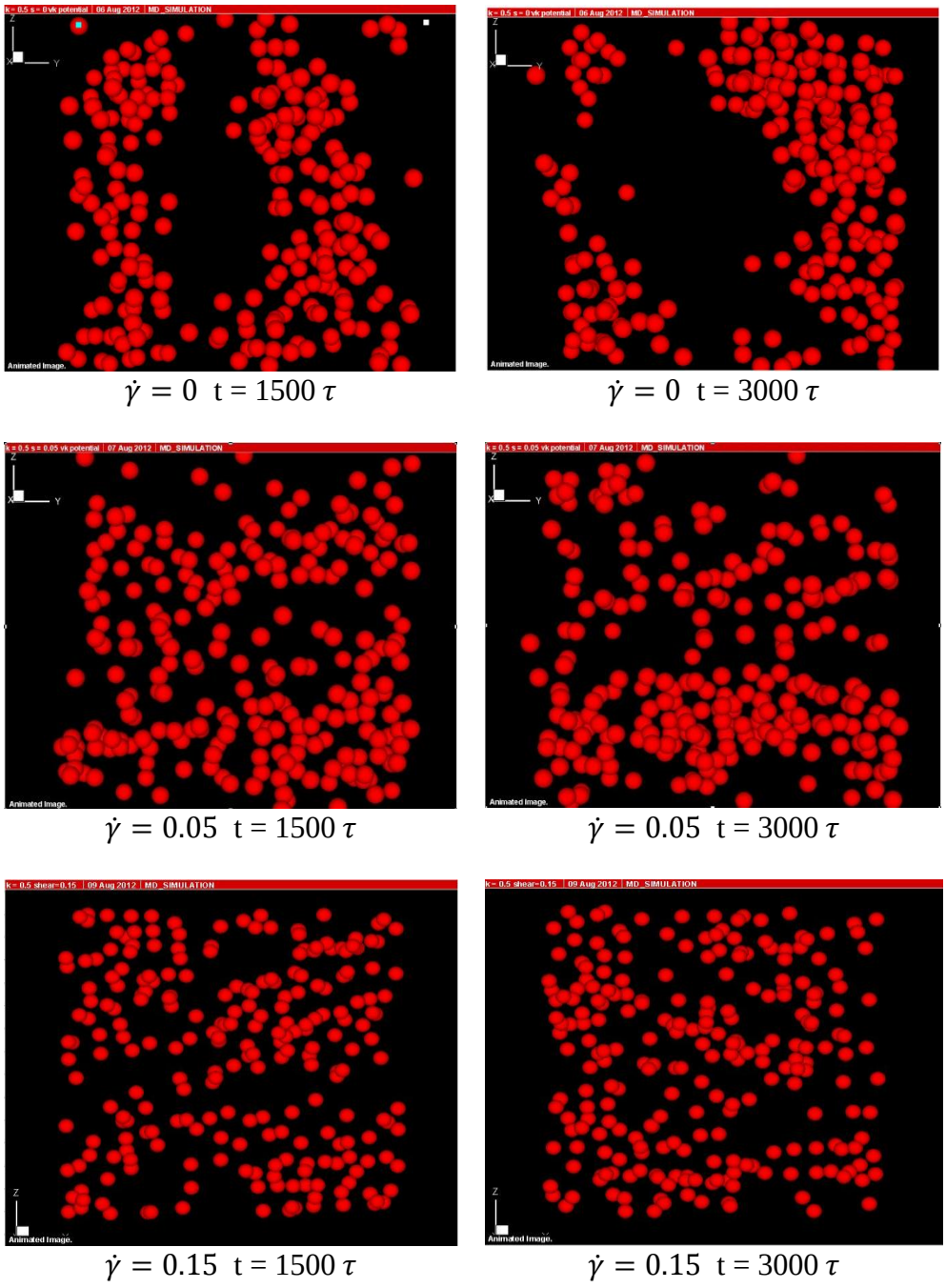

Figure 1-10 Reproduction work: effect of shear on nanoparticle placement

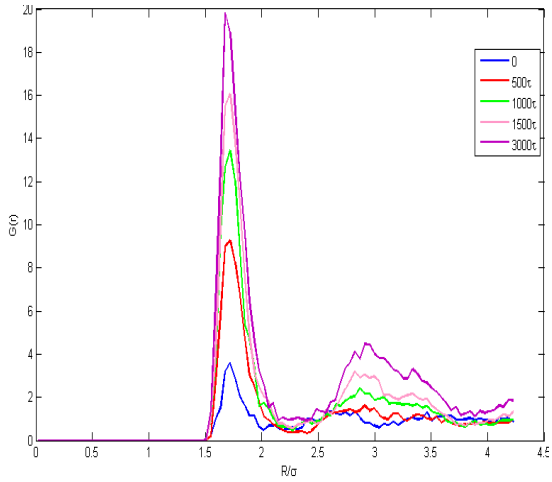

This Study: $\dot{\gamma} = 0$

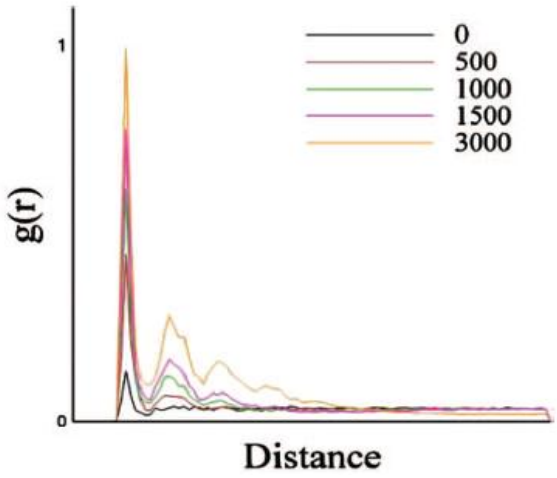

Original Study: $\dot{\gamma} = 0$

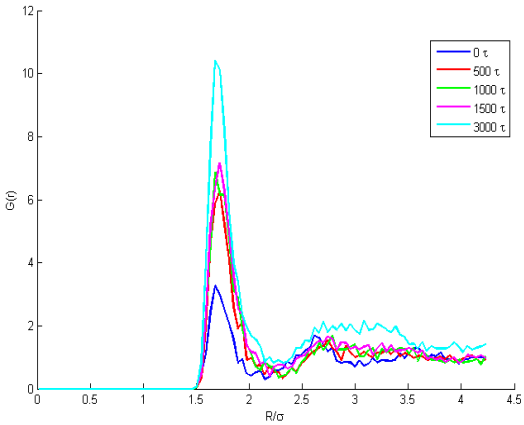

This study: $\dot{\gamma} = 0.05$

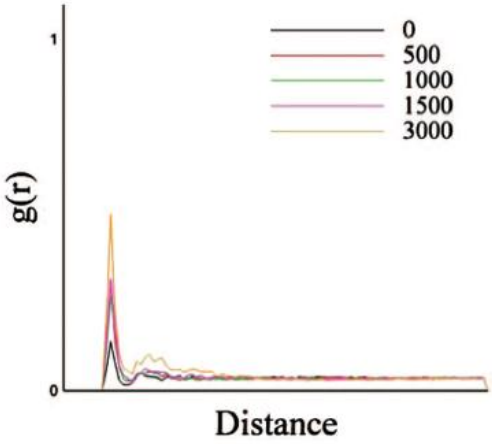

Original study: $\dot{\gamma} = 0.05$

Figure 1-11 Comparison in Radial Distribution Function G(r) between earlier published work[25] and this study.

Next, I validated the effect of polymer chain length on the translational diffusivity of the nanoparticles.

1.3.1.3 Effect of polymer chain length on nanoparticle diffusion

In this section, I varied the polymer chain length of suspending medium to probe its effect on nanoparticle diffusion under an equilibrium case.

As found in the original work, the nanoparticle diffusion converged to a limit where the diffusion is no longer dependent on the suspending medium. This can be seen clearly from the mean squared displacement plot, where beyond a certain polymer chain length, the curves overlapped. This effect can also be further confirmed if the diffusivity of nanoparticles is plotted as a function of polymer chain length, where a distinct plateau region can be pinpointed after the polymer chain length is increased beyond a certain critical length. In my reproduction of the earlier published study, I was able to reproduce similar behavior.

Nanoparticle Diffusion as a function of polymer chain length

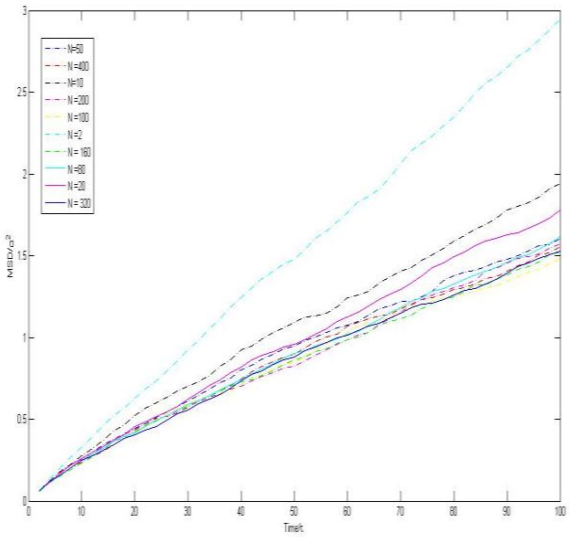

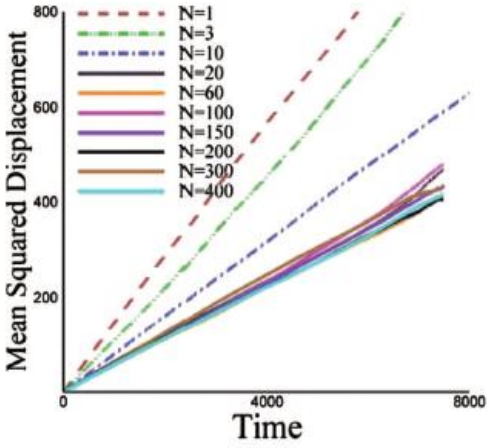

Reproduction work

Original Work

Nanoparticle diffusivity as a function of polymer chain length

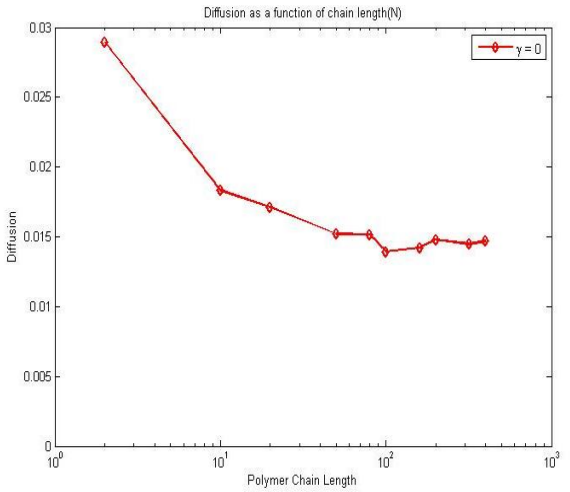

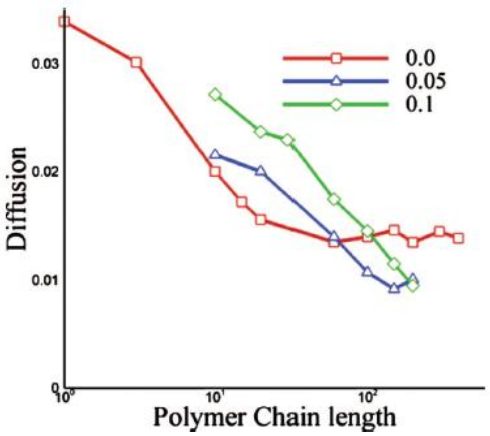

This study

Original study

Figure 1-12 Effect of polymer chain length on nanoparticle diffusion in this study compared to earlier published work [25]

Based on this validation work, we are confident that LAMMPS is an effective tool for our future studies on suspensions containing anisotropic particles.

1.4 Understanding Flow Behavior of Spherocylinder Nanoparticle Using Coarse-Grained Molecular Dynamics Simulation

1.4.1 Model and System

1.4.1.1 Solvent model, length scale, and time scale

The solvent model is based on a coarse-grained model[39] for water, where one interaction site represents four water molecules. Although this is a solvent model based on published work, a choice of four in coarse-grained molecular dynamics is a compromise between computation efficiency and model accuracy.

Since we are interested in dynamic properties, our main concern is to obtain a good reproduction of some typical dynamic properties. Hence, we chose two fundamental transport properties to study: translational diffusivity and the zero-shear viscosity of the water model.

Based on this coarse-grained model, the characteristic length- and time- scales associated with this model are listed in Table 1-2.

Table 1-2. Length and time scale based on four water molecule model

	CGMD value	CGMD units	Real value	Real units
Length Scale	1	σ	4.7×10^{-10}	m
Time Scale	1	$\sigma\sqrt{m/kT}$	1.78×10^{-12}	sec
Mass	1	m	1.19×10^{-25}	kg

Based on these two basic scales, the simulation can be mapped back to a physical lab frame with a suitable conversion factor.

A pure solvent system with the specific simulation characteristics listed in Table 1-3 has been carried out for the computation of translational diffusivity.

Table 1-3 System specifics for pure solvent system

Number density (ρ^*)	0.868
Box Length (L)	8.3205
Time step Size (δt)	0.005
Temperature (kT/ε)	0.5

The translational diffusivity for pure solvent system is calculated by Einstein formula for diffusivity, which is given by

$$D_t = \lim_{\Delta t \to \infty} \frac{1}{6\Delta t} < r^2(\Delta t) > \qquad 1\text{-}13$$

where $< r^2(\Delta t) >$ is the translational mean square displacement (MSD) of the solvent molecules

$$< r^2(\Delta t) > \equiv \frac{1}{N} \sum_{i=0}^{N} |\vec{r}_i(t') - \vec{r}_i(t)|^2 \qquad 1\text{-}14$$

Here, $\vec{r}_i(t')$ and $\vec{r}_i(t)$ are the positions of solvent molecule, *i*, at times *t* and t', respectively, and $\Delta t = t' - t$.

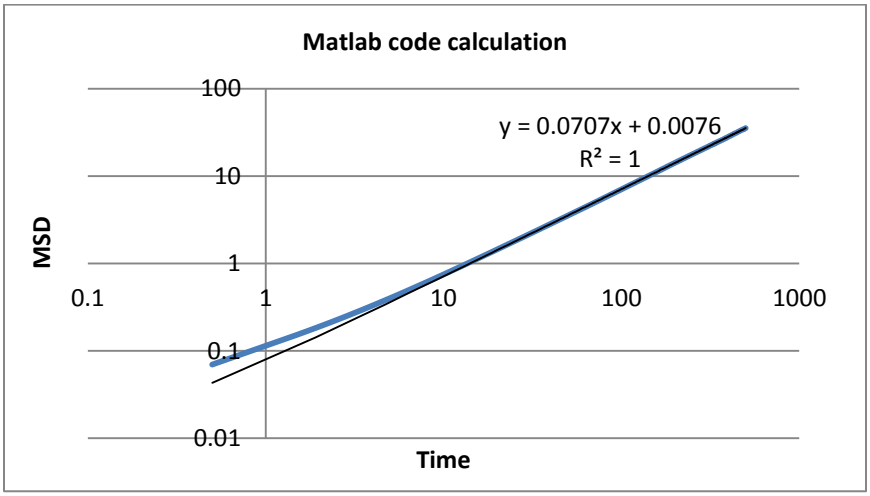

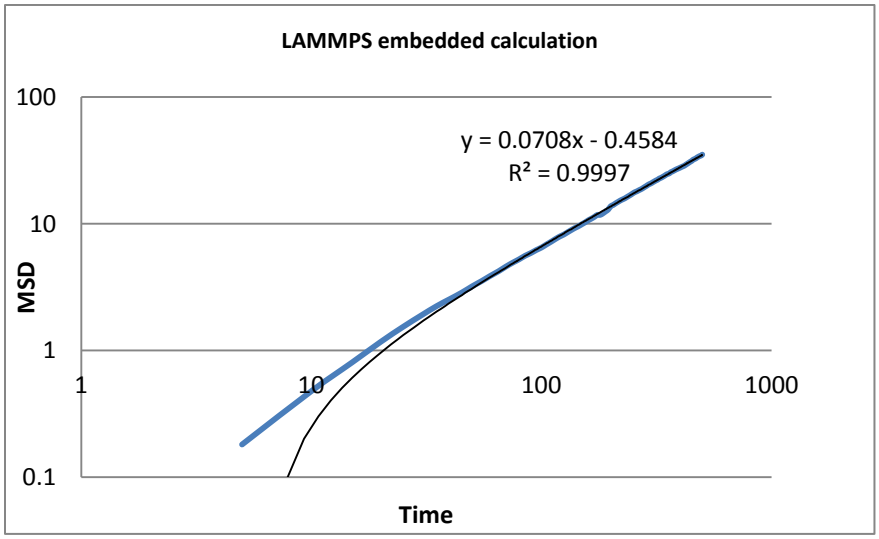

Figure 1-13 Diffusivity computation based on developed codes and embedded computation in LAMMPS

Comparison between solvent translational diffusion coefficients obtained from simulation to that in physical situation is tabulated in Table 1-4. The physical diffusion coefficient is obtained by converting simulation value based on the conversion factor.

Table 1-4 Diffusion coefficient calculated from simulation and from physical situation

Diffusion coefficient obtained from MD simulation (σ^2/τ)	Physical diffusion coefficient based on conversion factor (m^2/s)	Physical diffusion coefficient from reference[39] (m^2/s)	Water diffusion coefficient 300K (m^2/s)
0.012	1.5×10^{-9}	2.0×10^{-9}	2.3×10^{-9}

The physical diffusion coefficient acquired from simulation gives back a close value with reference value. The comparison in diffusivity here served as a legitimate check that the coarse-grained model design is an appropriate model to use. On the other hand, viscosity of this solvent medium has also been computed to compare to its physical value.

Table 1-5 Comparison in solvent viscosity between coarse-grained solvent model and physical value

MD value ($P\tau$)	Physical value based on convertion ($Pa \cdot s$)	Physical value of water at 300K ($Pa \cdot s$)
8.41	12×10^{-4}	8×10^{-4}

The simulation results of viscosity calculation turned out to be very comparable to that of physical value. As viscosity is not an enforced by the coarse-grained model adopted in this work, it is still comparable to a certain extent that this model works for properties that are not built-in.

Upto the fair enough comparison in diffusivity and viscosity, the coarse grained model referred by this work serves as a reasonable model for further studies.

1.4.1.2 Particle Model

In the course of this study, several particle models have been evaluated. However, due to technical limitations, as well as limited time and computer resources, some of these options have been set aside for now. They can be revisited later.

At the beginning of this project, the effect of anisotropy was taken into account by using a single site orientation dependent potential an orientation-dependent potential, the Gay-Berne potential. At the beginning of this project, a single site, orientation dependent Gay-Berne potential was used for anisotropic Lennard-Jones potential between pairs of ellipsoidal particles. Since the computation of distance is orientation-dependent in the Gay-Berne, use of this potential is not compatible when coupling with a thermostat adapted from Dissipative Particle Dynamics (DPD), which is critical in preserving hydrodynamic interactions, a very important long- range interaction in suspension problems.

In addition, we would like to introduce a homogeneous suspension state by avoiding particle-particle interaction. Hence several particle models have been devised to circumvent the incompatibility issue as well as provide an ability to supply a repulsive potential to the system.

Therefore, several particle models composed of sub-particles whose size are the same as solvent particles have been devised to circumvent the incompatibility issue, arising from distance calculation.

1.4.1.2.1 Spheroid

A first spheroid model can be constructed by placing constituent particles that are of the same size as the coarse-grained solvent bead on an ellipsoid surface. In other words, the positions of the constituent particles suffice the ellipsoid surface equation.

$$\frac{x^2}{a^2}+\frac{y^2}{b^2}+\frac{z^2}{c^2}=1 \qquad \text{1-15}$$

where a is the semi-length of the major axis, and b and c are the semi-lengths of the minor axis. A single spheroid particle model and a suspension containing spheroids are shown in Figure 1-14.

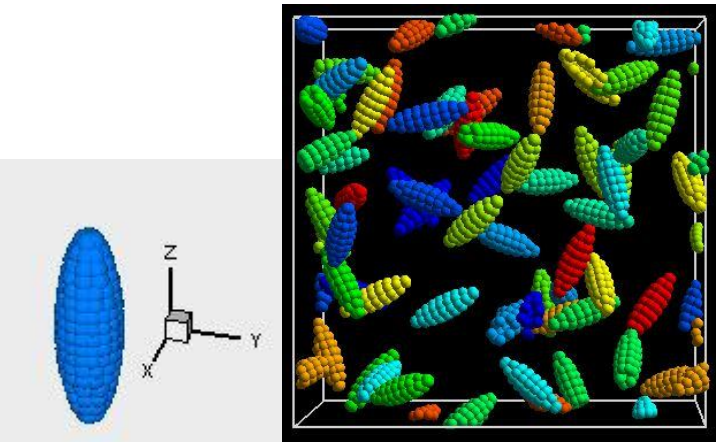

Figure 1-14 (Left) Prolate particle of aspect ratio 3, with the length of long axis being 9, and the minor axis being 3, composed of sub-particles whose size is equal to that of the solvent molecule. (Right) A suspension containing such prolate particles.

Although this spheroid model fully suffices the geometry requirement, it is a computational very expensive model to adopt. Therefore, in order to keep the anisotropy feature while being computationally affordable, we chose to work with a simplified model – a linear overlapped sphero-cylinder particle model.

1.4.1.2.2 Sphero-cylinder

An overlapped sphero-cylinder model[40] referred to the initial formulation of the Gay-Berne potential is built to construct an aspect ratio of 3 for the sphero-cylinder model, whose length of major axis is 3, and of minor axis is 1. The length in the minor axis direction is comparable to the solvent size. The model is built by placing constituent particles in an overlapped fashion: the distance between two adjacent beads is $^{2}/_{3}\,\sigma$. By repeating this pattern, the length of major axis can be extended to build elongated particles with various aspect ratio.

To have a neutrally buoyant system, the mass of the sub-particle is assigned to match the density of the solvent bead.

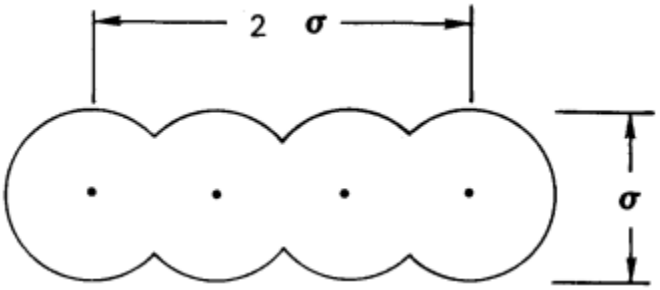

Figure 1-15: A four-site molecule used by Gay and Berne to derive Gay-berne Potential.[40]

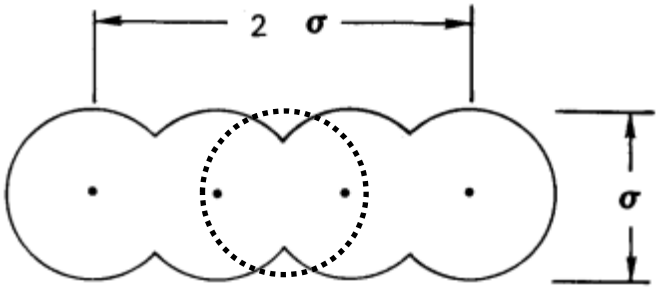

Figure 1-16 Schematic drawing of particle model adopted in this work.

Referring to this linear overlap model, different aspect ratios of elongated particles can be modeled based on simply placing more particles on each end.

1.4.1.3 Interaction Potential

To study the contribution of particle anisotropy to flow behavior and induced microstructure, it is desired to introduce a homogeneous suspension state at equilibrium.

1.4.1.3.1 Simple solvent medium particulate suspensions

In the pilot system, the interaction between solvent molecules is assigned to be a Lennard-Jones potential, with a cut-off distance of 3.0 σ. The interaction between constituent particles of nanoparticles is assigned to be a purely repulsive potential, the well-known Weeks-Chandler-Anderson potential. The interaction between solvent molecules and constituent particles of nanoparticles is assigned to be Lennard-Jones potential with a cutoff distance at 3.0 σ.

A pure repulsive system can be characterized by zero Hamaker constant, which is proportional to $n_p^2\varepsilon_{pp} + n_s^2\varepsilon_{ss} - 2n_p n_s\varepsilon_{sp}$, where n_p is bead number density per nanoparticle, n_s is bead number density per solvent molecule, $\varepsilon_{pp}, \varepsilon_{ss}, \varepsilon_{sp}$ is interaction energy per unit volume between nanoparticle and nanoparticle, solvent and solvent, solvent and nanoparticle, respectively.

In this work, bead number density for nanoparticle and for solvent molecule is defined as number of beads composing per particle/volume of particle, the volume of particle is defined as Eqn..1-25.For simplicity, we for now neglect the effect of overlapping. Therefore, for five-bead nanoparticle with aspect ratio 3, n_p is found to be 2.387. Solvent number density is defined as $n_s = \frac{N_s}{(Vcell - V_p)}$, where N_s being total number of solvent beads, V_p represents the total volume occupied by the particles.

Based on the system specifics, n_s is tabulated as following.

Table 1-6 solvent number density at each volume fraction of suspensions

φ	1.52%	4.97%	9.16%
n_s	0.86	0.85	0.84

The Hamaker constant for this pilot system resulted from potential assignment is -3.65. To result in a zero Hamaker constant with bead number density adopted by this work, a better choice would be to assign interaction energy parameters as tabulated in

Table 1-7 Interaction energy assignment for different suspension systems

φ	1.52%	4.97%	9.16%
$\varepsilon_{ps}/\varepsilon_{ss}$	5.53	5.61	5.71

1.4.1.4 Initialization Scheme

In order to incorporate non-spherical particles, as well providing fast equilibration, an initial configuration with a low number density is preferred. Ellipsoidal particles are placed in the middle of the medium, in a manner resembling a sandwich. The positions of the solvent particles were generated by MATLAB in a random, overlapped configuration. However, the ellipsoidal particles are placed in the middle of two layers of solvent and in an ordered configuration. This initialization scheme facilitates introducing complex medium as well as leading to a fast diffusion of nanoparticles. The starting number density is about 0.3; after applying a soft potential to the solvent particles, any slight overlaps between particles can be removed and in this way obtain an initial configuration without any overlaps.

$$E = A\left[1 + \cos\left(\frac{\pi r}{r_c}\right)\right] \qquad r < r_c \qquad \text{1-16}$$

The prefactor A in 1-16 is an energy parameter that can be made to vary in time from the start to the end of the run, e.g. to start with a very soft potential and slowly harden the interactions over time. r_c is the cutoff distance, and it is set to be 1.12246 σ, which is the minimum of Lennard-Jones potential.

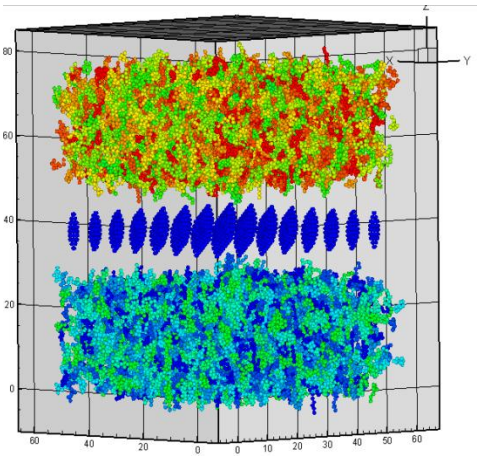

Figure 1-17 Scheme designed to initialize large system to accommodate complex particle geometry and suspending medium.

The next step is to compress the system until the solvent number density reaches a density that is lower than, but closer to, the desired number density.

At this step, time integration is performed on Nosé-Hoover style non-Hamiltonian equations of motion which are designed to generate positions and velocities sampled from isothermal-isobaric (NPT) ensemble.

The third step is to slightly vary the box size until it reaches the desired solvent number density.

1.4.1.5 Thermostat: DPD thermostat

In the studies of colloidal suspension, hydrodynamic interaction plays a critical role. To preserve this important feature, we adopted 'Dissipative Particle Dynamics' (DPD) as a thermostat.[41] Originally devised to simulate fluids on a mesoscopic scale with 'soft' particles, DPD, on the other hand, is suitable to be used as a thermostat for simulations with hard potentials. One distinct advantage of coupling a DPD thermostat to a standard MD system is that it allows the

system to accommodate a substantially larger time step compared to pure MD, thus facilitating long-time behavior observations, and nevertheless preserving hydrodynamic behavior correctly. Soddemann et al.[42] has demonstrated that DPD thermostat outweighs Nosé-Hoover thermostat as well as a stochastic dynamics Langevin thermostat in the dynamics studies.

The DPD equations of motion are given by

$$\frac{d\overrightarrow{\boldsymbol{r_i}}}{dt} = \frac{\overrightarrow{\boldsymbol{p_i}}}{m_i} \tag{1-17}$$

$$\frac{d\overrightarrow{\boldsymbol{p_i}}}{dt} = \sum_{i \neq j} \vec{\boldsymbol{F}}_{\boldsymbol{ij}}^{\boldsymbol{C}} + \sum_{i \neq j} \vec{\boldsymbol{F}}_{\boldsymbol{ij}}^{\boldsymbol{D}} + \sum_{i \neq j} \vec{\boldsymbol{F}}_{\boldsymbol{ij}}^{\boldsymbol{R}} \tag{1-18}$$

where $\vec{\boldsymbol{F}}_{\boldsymbol{ij}}^{\boldsymbol{D}}$ denotes thedissipative force and $\vec{\boldsymbol{F}}_{\boldsymbol{ij}}^{\boldsymbol{R}}$ corresponds to the random force, these two terms act as heat source and drain, therefore regulating the simulation cell temperature $\vec{\boldsymbol{F}}^{\boldsymbol{c}}$ is the conservative force that acts between two particles.

The dissipative force can be expressed as follows, based on work by Espanol and Warren [43]

$$\vec{\boldsymbol{F}}_{\boldsymbol{ij}}^{\boldsymbol{D}} = -\zeta w^{D}(\boldsymbol{r_{ij}})\widehat{(\boldsymbol{r}_{\boldsymbol{ij}}} \cdot \vec{\boldsymbol{v}}_{\boldsymbol{ij}})\hat{\boldsymbol{r}}_{\boldsymbol{ij}} \tag{1-19}$$

where ζ is a friction parameter and $w^{D}(r)$ is a weight function.

Here, $\vec{\boldsymbol{v}}_{\boldsymbol{ij}} = \vec{\boldsymbol{v}}_{\boldsymbol{i}} - \vec{\boldsymbol{v}}_{\boldsymbol{j}}$ is the relative velocity between particles *i* and *j*, while $\hat{\boldsymbol{r}}_{\boldsymbol{ij}}$ denotes the unit vector of the interatomic axis.

And the random force is given by

$$\vec{\boldsymbol{F}}_{\boldsymbol{ij}}^{\boldsymbol{R}} = \sigma w^{R}(\boldsymbol{r_{ij}})\theta_{ij}\hat{\boldsymbol{r}}_{\boldsymbol{ij}} \tag{1-20}$$

where σ is a noise parameter and θ_{ij} is a white noise variable.

From the fluctuation-dissipation theorem, we have

$w^D(r), w^R(r)$ are weight functions that vary between 0 and 1. As reported by Fraser et al., the weight function has the form:

$$\sigma = (2k_B T\zeta)^{1/2} \tag{1-21}$$

$$w^D(r) = [w^R(r)]^2 \tag{1-22}$$

$$w^D(r) = w^R(r) = w(r) \tag{1-23}$$

$$w(r) = \begin{cases} 1, & r < r_c \\ 0, & r \geq r_c \end{cases}$$

1.4.1.6 Issues to watch for future work

In the preliminary set-up, there are some issues that are worth watching:

1) Ensemble choice: an NPT ensemble is preferred over an NVE ensemble in the stage of equilibration. In order to maintain the constant liquid density while varying particle loading, it is essential to operate under a constant pressure. The problem with current work using an NVE ensemble is that it brought large fluctuations in pressure, this brought extra concern on if the liquid density is well maintained at a constant.
2) Zero Hamaker constant: to result in a homogenous, well-dispersed system, Hamaker constant of the suspension has to be zero. This can be done either by assigning interaction energy of solvent-solvent interaction and solvent particle interaction at certain ratio, tabulated in Table 1-7; or to match the density of solvent bead with that of the particle.
3) Friction coefficient for DPD thermostat: it is preferred to set the friction coefficient ζ to be 1.0. See section 1.4.2.1 for reasoning.

1.4.2 Results

1.4.2.1 Solvent Environment

Our first investigation concerns the solvent environment. In order to control temperature at high shear rates, a friction coefficient , ζ , of the DPD thermostat is taken to be 5.0.

The equilibrium diffusivity is found through calculations based on the mean-squared displacement, using the Einstein relationship described in equation 1-14 above. The equilibrium diffusion coefficient for the solvent is found to be $0.0065\sigma^2/\tau$, with friction coefficient for the DPD thermostat to be 5.0.

In order to determine the zero-shear viscosity, a series of non-equilibrium dynamic simulations is applied to the solvent cell with dimensionless shear rates ranging from 1×10^{-3} to $1\ \tau^{-1}$The time step size is set to be 0.01τ, with τ being simulation time. A fixed amount of strain $\Gamma = \int_0^T \dot{\gamma} dt$, which is defined as shear rate × time step size × total number of steps is applied to the system. For solvent environment investigation, this amount is set to be 50 to the simulated solvent cell at all shear rates. From the viscosity plot, we can determine the zero- shear viscosity from the Newtonian plateau, which is found to be $22.41\sqrt{\varepsilon^3 m\sigma^4}$.

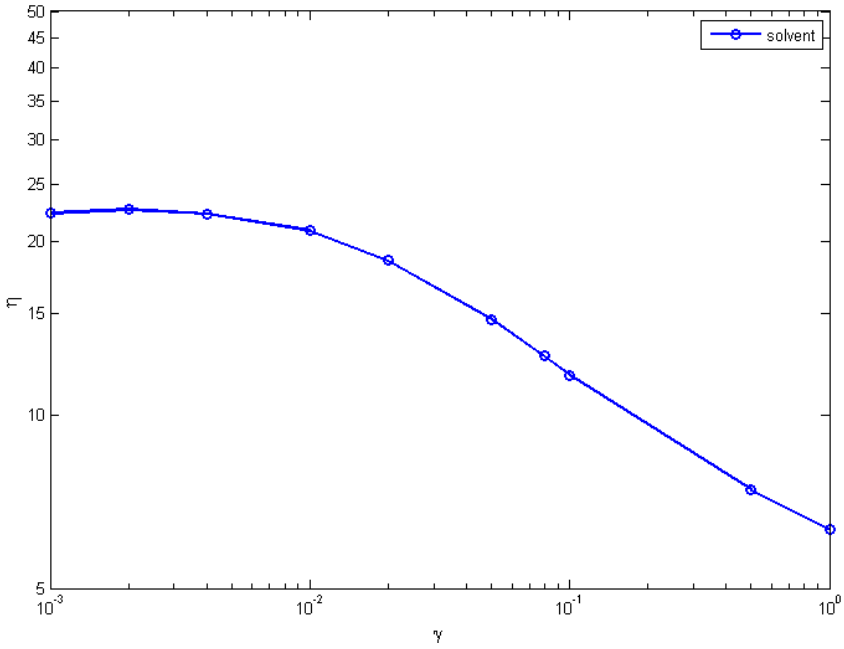

Figure 1-18 Apparent viscosity as a function of shear rate for solvent medium

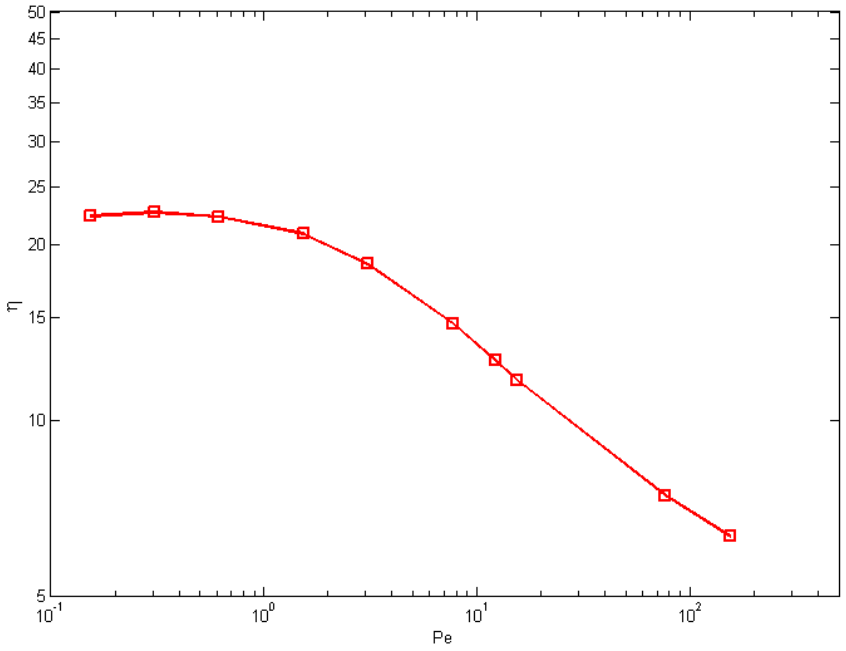

Figure 1-19 Apparent viscosity as a function of Peclet number for solvent environment

Although in this work, the friction coefficient used for DPD thermostat is set to be 5.0 throughout all calculations, it is worth mentioning that a friction coefficient of 1.0 has been studied for background solvent dynamic behavior. For both friction coefficient values used, we calculated the equilibrium diffusivity and zero-shear viscosity. As these solvent beads are Lennard-Jones point particles, therefore Stokes-Einstein relation with a slip boundary condition is applied to compare the hydrodynamic radius of the solvent bead. The comparison is tabulated in

Stokes-Einstein relationship with slipping boundary condition is

$$D_0 = \frac{k_B T}{4\pi\eta R_H} \qquad 1\text{-}24$$

where D_0 is equilibrium diffusivity, η is zero shear viscosity, R_H is hydrodynamic radius. For slip boundary condition, a coefficient of 4 is used rather than 6.

Table 1-8 Comparison in equilibrium diffusivity, viscosity, hydrodynamic radius when using two different fricition coefficient for DPD thermostat

Friction Coefficient	D_0	η	R_H	$R_{geometric}$
1.0	0.0117	8.41	0.405	0.5
5.0	0.0065	22.41	0.273	0.5

It is found that hydrodynamic radius is closer to its geometrical radius if friction coefficient is assigned to be 1. From the perspective of implementation, the effect of using a larger friction coefficient helps to control the temperature of simulation cell more effectively under high shear rates than a smaller one. But the consequence of a smaller hydrodynamic radius remains to be elusive.

Based on this investigation of the solvent medium, we then suspend nanoparticles at three volume fractions into the solvent cell. We began by suspending ellipsoidal particles, with a major axis of 9, and a minor axis of 3. Such aspect ratios proved to be too time-consuming to simulate in a reasonable time; therefore, to obtain preliminary results, a sphero-cylinder model is adopted to allow consideration of a smaller system size. The particles we used initially have an aspect ratio of 3, with the length of the major axis set to be 3, and the length of minor axis set to be 1.

1.4.2.1.1 Volume fraction definition

For a spherocylinder of aspect ratio p, the volume of a sphero-cylinder is defined based on the particle geometry according to the following definition:

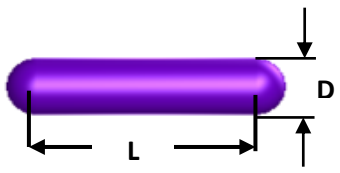

Figure 1-20 Schematic drawing for a sphero-cylinder particle with aspect ratio of 3

$$v_0 = \pi \left(\frac{LD^2}{4} + \frac{D^3}{6}\right) \quad \text{1-25}$$

where D is the diameter of the hemisphere, and L is the length of the spherocylinder body.Hence, the definition of the volume fraction is defined as

$$vol\% = \frac{Nv_0}{V_{box}} \quad \text{1-26}$$

where N stands for total number of sphero-cylinders.

The solvent number density within fluid phase is kept to a value of 0.868 throughout the simulation systems, as the effect of changing the volume fraction is investigated, as the same osmotic pressure needs to be maintained throughout. This is achieved by dividing the number of solvent beads by the volume after deducting the particle volume from the total volume of the simulation cell.

Table 1-9 System specifics for three systems investigated

Volume fraction	**1.52%**	**4.97%**	**9.16%**
No. spherocylindrical particles	200	688	1350
No. solvent beads	23436	23436	23436
Simulation cell length	30.21	30.72	31.37
Particle number density	0.007	0.024	0.044

Three systems corresponding to different volume fractions have been investigated: one contains 1.52% of spherocylinders, one contains 4.97%, and the other contains 9.16% of spherocylinders. These choices of volume fractions are explained below. The medium is composed of a simple solvent. In order to be consistent with Doi and Edward's theory, we compare the particle number density with the concentration regime defined by Doi and Edward. For 1.52%, the number

density results in a dilute suspension, defined as $< \frac{1}{L^3}$, whereas at 9.16% the system results in a so-called semi-dilute regime, defined as $\frac{1}{L^3} \ll \nu \ll \frac{1}{dL^2}$.

Table 1-10 Particle number density and its concentration regime

Volume fraction	Particle number density (ν)	νL^3	$\nu L^2 d$
1.52%	0.007	0.19	0.06
4.97%	0.024	0.65	0.22
9.16%	0.044	1.19	0.40

The system is updated by the microcanonical NVE ensemble at a temperature of $T^* = kT/\varepsilon$ = 0.5. A range of shear rates from 5×10^{-4} to 0.5 were investigated. Similar to the method described above for the solvent system, a fixed amount of strain is applied to each volume fraction at all shear rates. A good reference point at which to stop shear would be the moment when a linear velocity profile has been established across the simulation cell. In this work, a strain of 50 is applied to the lowest volume fraction, and a deformation amount of 200 is applied to both the 4.97% and 9.16% volume fraction systems.

The viscometric functions, such as shear viscosity and the normal stress differencesN_1, $N_2$are extracted from the pressure tensor as computed by LAMMPS,

$$P_{ij} = -\frac{1}{V}\left(\sum_k^n m_k \boldsymbol{v_{ki}} \boldsymbol{v_{kj}} + \sum_k^n \boldsymbol{r_{ki}} \boldsymbol{f_{kj}}\right) \quad \text{1-27}$$

where V is the system volume, *i j,k = x,y,z*.

For accuracy, the stress tensor data are only used when a linear velocity profile has been established. Based on the following viscometric functions, I obtained the results in the following section.

$$\eta(\dot{\gamma}) = -\frac{P_{12}(\dot{\gamma})}{\dot{\gamma}} \quad \text{1-28}$$

Shear viscosity data are plotted against the dimensionless shear rates applied to the system. Then the data are fit into Carreau-Yasuda model.

$$\eta = \eta_0/[1 + (\lambda\dot{\gamma})^2]^{(1-n)/2} \quad \text{1-29}$$

where η is apparent viscosity, η_0 is zero shear viscosity, λ is relaxation time, p is shear thin index. Table 1-11 shows the fitting results of zero shear viscosity η_0, relaxation time λ, and shear thin index p for each suspension, as well as for suspending medium. Figure 1-21 shows both simulation results, as well as the fitting results.

Table 1-11 Fitting parameters for Carreau-Yasuda model of apparent viscosity and apparent shear rate

ϕ	η_0	λ	n
Solvent	22.6	87.1	0.71
0.0152	29.6	193.9	0.71
0.0497	62.2	678.1	0.66
0.0916	151.4	1499.0	0.56

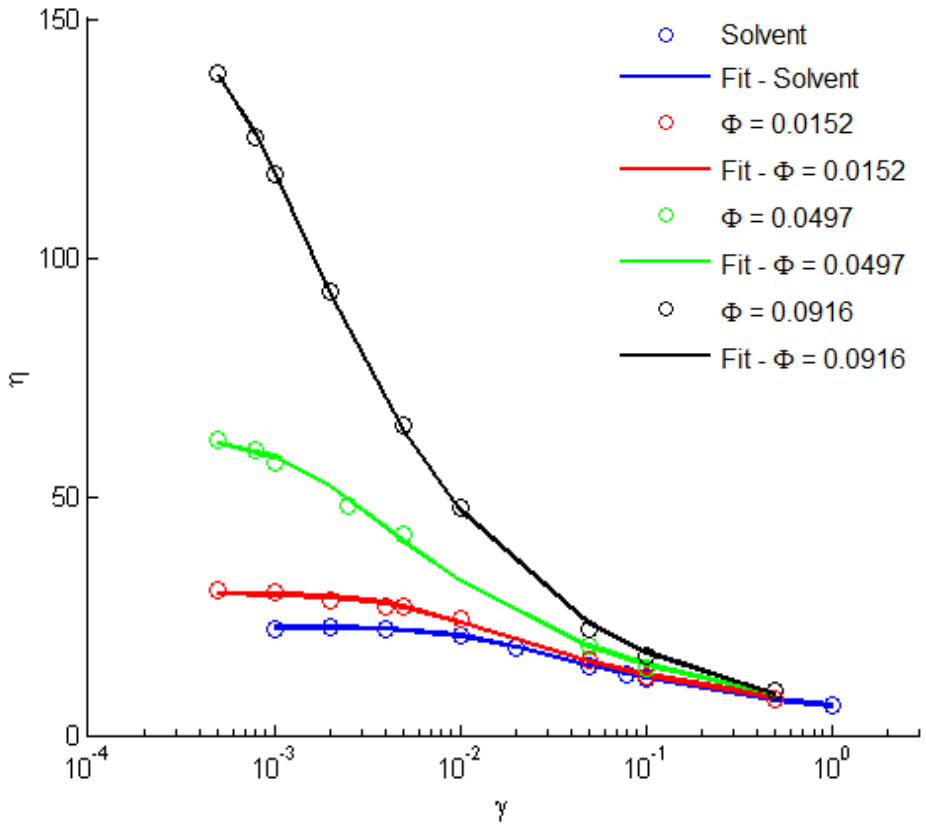

Figure 1-21 Apparent shear viscosity as a function of apparent shear rate for suspensions containing particle loadings of volume fraction 1.52%, 4.97%, and 9.16% (circles). Lines show the fitted results for Carreau-Yasuda model. The data agrees very well with Carreau-Yasuda model.

In order to compare our results to other literature findings, relative viscosity is obtained by rescaling apparent viscosity data at each shear rate by the zero shear viscosity of suspending medium at corresponding shear rate, and the dimensionless shear rates are rescaled by rotational Peclet number Pe_r, which is a quantity that controls the cross-over from Brownian behavior to non-Brownian behavior of a fluid suspension. It is also a measure for the flow intensity with respect to perturbation from Brownian motion.

A rotational Peclet number is defined as

$$Pe_r = \frac{\dot{\gamma}}{D_r} \quad (1\text{-}30)$$

where $\dot{\gamma}$ is apparent shear rate, and D_r is rotational diffusivity.

A rotational diffusivity of a spherocylinder [44] is defined as

$$D_r = \frac{3D_0}{\pi L^2}\left(lnp - 0.662 + \frac{0.917}{p} - \frac{0.05}{p^2}\right) \quad (1\text{-}31)$$

where p is the aspect ratio of a spherocylinder and L being the length of the cylindrical body part of the spherocylinder. D_0 is defined as

$$D_0 = \frac{k_B T}{\eta_s L} \quad (1\text{-}32)$$

where η_s the zero shear viscosity of suspending medium, and L being the length of cylindrical part of a spherocylinder.

We then plot relative viscosity as a function of rotational Peclet number at different volume fractions at the regime where solvent does not exhibit as non-Newtonian fluid. Deborah number can be used to quantify the non-Newtonian nature of a suspension. Deborah number is the product of relaxation time λ and apparent shear rate $\dot{\gamma}$. Fluids exhibit shear thin behavior when Deborah number is greater than 1. Therefore, to exclude the non-Newtonian effect of suspending medium on the rheological behavior of particulate suspensions, the data is plotted upto a shear rate of 0.01, corresponding to a solvent Deborah number of 0.871. This regime guarantees us a Newtonian behavior of the suspending medium.

By fitting the data into Carreau model, fitting parameters are obtained and tabulated in Table 1-12.

$$\frac{\eta - \eta_0}{\eta_0 - \eta_\infty} = [1 + (\lambda Pe_r)^2]^{\frac{n-1}{2}} \quad (1\text{-}33)$$

Figure 1-22 shows relative viscosity of particulate suspension containing three different amounts of particle loadings plotted against rotary Peclet number.

Table 1-12 shows the fitting results for relative viscosity and rotary Peclet number for Carreau model.

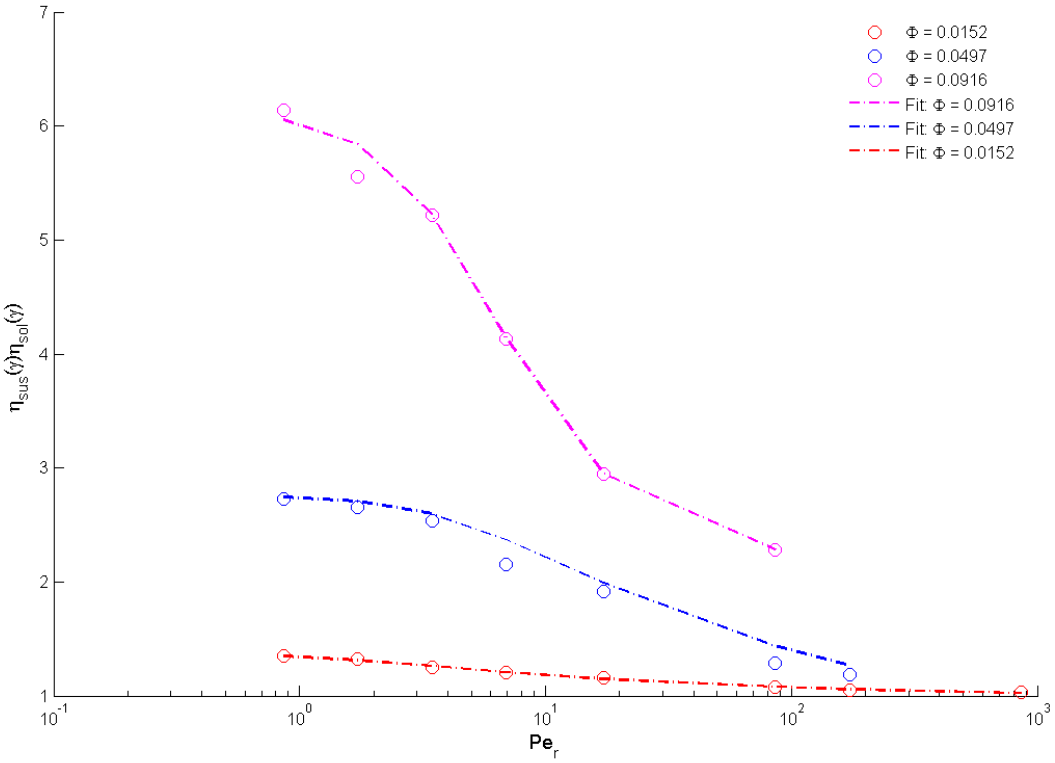

Figure 1-22 Relative viscosity as a function of rotary Peclet number for suspensions containing different amounts of particle loadings.

Table 1-12 Fitting parameters for Carreau model of relative viscosity and apparent shear rate

φ	η_0	η_∞	λ	n
0.0152	1.37	0.98	1150	0.94
0.0497	2.80	0.46	409	0.71
0.0916	6.13	2.17	362	0.56

From the fitting, we can see a more distinct shear thin phenomenon indicating by the decrease in shear thin index n. This finding is consistent with the observations from the early work of fiber suspension Gannani and Powell[45] , an increase in spherocylinder particle loadings in suspensions increased the shear thinning nature of the fluid; in addition, the relaxation time also increases when particle loading increases, as rods introduce a relaxation time $^1/_{D_r}$.

To validate our simulation results, it is worthwhile to compare viscosity measurement from simulation results to experimental studies. Fiber suspensions contain high aspect ratio particles; hence a more interesting comparison is going to be made by comparing particulate suspensions containing elongated particles with

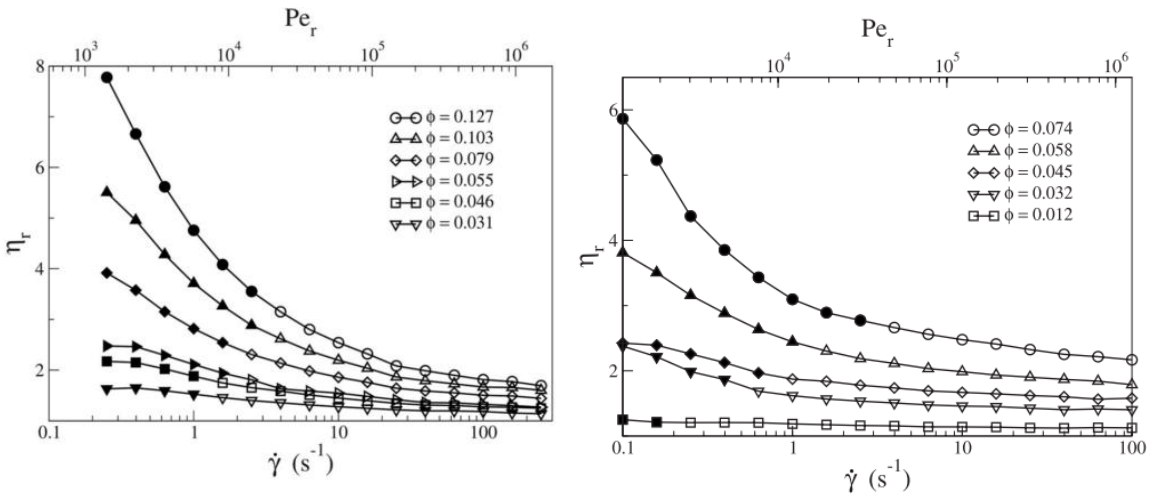

Figure 1-23 Relative viscosity as function of apparent shear rate, and rotational Peclet number for suspensions containing ellipsoidal particles of aspect ratio 4 (left) and aspect ratio 7 (right) at various volume fraction. Adapted from Bricker and Butler, 2008[11]

moderate aspect ratio. In Bricker and Butler's[45] studies, relative viscosity measurements containing polystyrene particles at multiple volume fractions with aspect ratio of 4 and 7 have been carried out. Figure 1-23 shows the results from his work that we would further compare our results to.

One thing to notice is that the rotary Peclet number range is complementary to the range of Peclet number that we have studied. To compare results from our work to Butler's work, we first fit his data into a model that describes both power law behavior of the suspension as well as the second Newtonian plateau. Secondly, we plot the viscosity measurement results in a same plot with Butler's experiment results. By doing so, we can have a general idea between simulation results and experimental studies.

First, we fit our data into the following model

$$\mu(\gamma) = \mu_{inf} + bPe_r^{n-1} \qquad 1\text{-}34$$

This fitting helps us to find out the value of the second Newtonian plateau, as well as the shear thin index n. The shear thin index n can be used to compare with the fitting with Carreau model for the simulation results. This model gives very good fitting for both particulate suspensions, as shown in Figure 1-24**.**

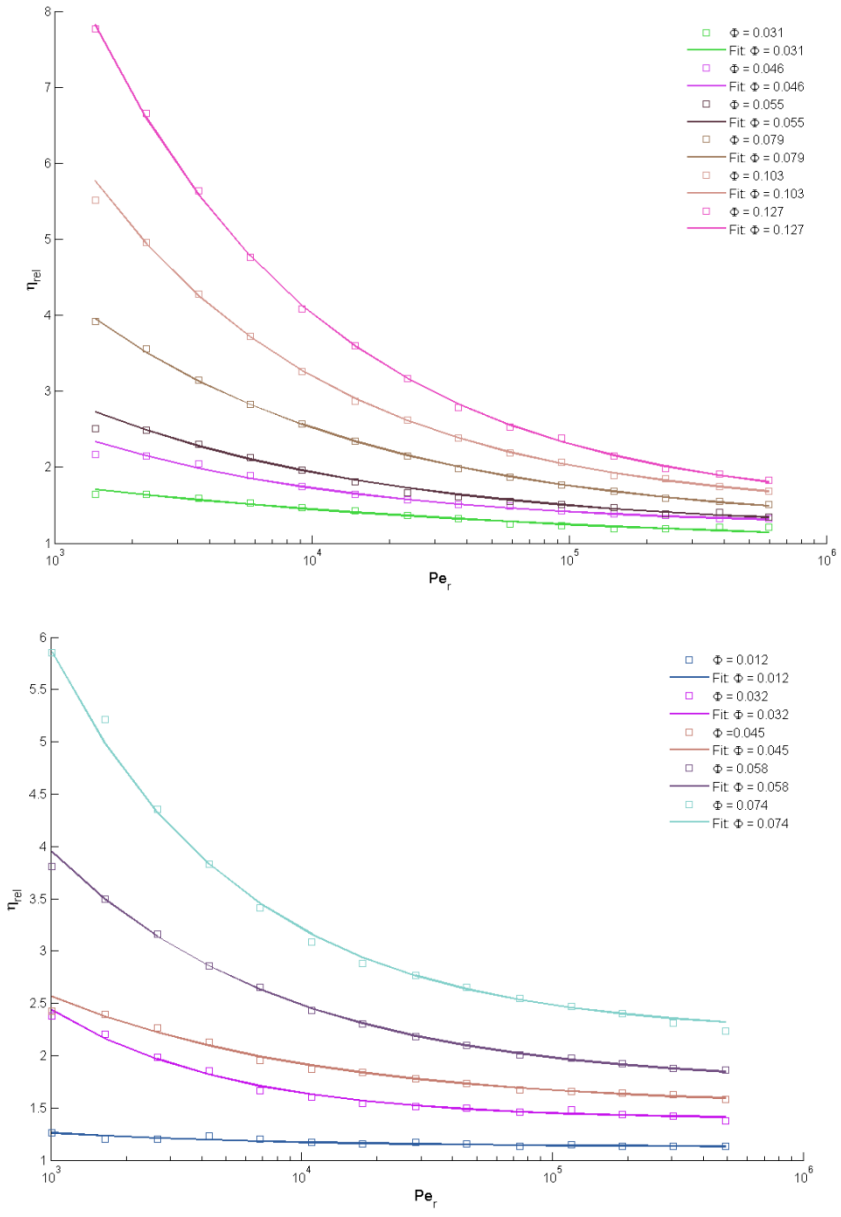

Figure 1-24 Data adapted from Bricker and Butler's results suspension relative viscosity as a function of shear rate of suspension containing aspect ratio 4 (upper plot), and aspect ratio 7 (lower plot). Lines show the fitting results.

Table 1-13 Fitting parameters for Butler's data

Aspect Ratio	φ	μ_{inf}	b	n	R^2
4	0.031	0.9108	3.532	0.79	0.98
	0.046	1.214	21.51	0.59	0.98
	0.055	1.176	23.28	0.63	0.98
	0.079	1.216	43.68	0.62	0.99
	0.103	1.407	122.6	0.54	0.99
	0.127	1.414	186.2	0.54	0.99
7	0.012	1.125	3.384	0.54	0.94
	0.032	1.388	74.37	0.38	0.99
	0.045	1.510	18.18	0.59	0.99
	0.058	1.720	56.29	0.53	0.99
	0.074	2.207	178.6	0.44	0.99

By comparing the shear thin index from the results of Butler's work and this work, Figure 1-25,we can see the shear thin behavior of suspensions from this work is comparable to Butler's with suspensions containing particles with aspect ratio 4.

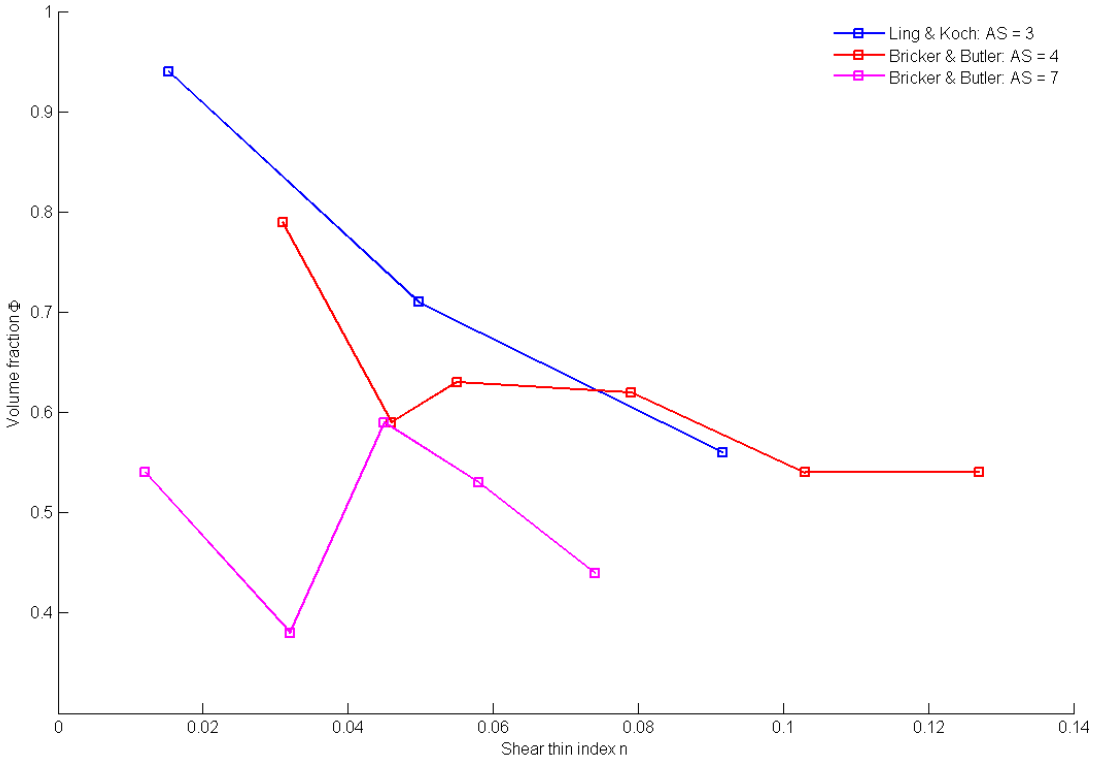

Figure 1-25 Comparison of shear thin index at various volume fraction. Data is plotted with data from Bricker and Butler.

Also, it appears that relative viscosity in this study levels off at high rotary Peclet number on order 10-100, which contradicts Butler's observation that suspension exhibit shear thinning for much higher rotary Peclet number.

For the suspension containing the lowest volume fraction, we also compared our data to theoretical calculation. The theoretical work that have been compared to are H. Brenner's[46] and I.Claeys and JF Brady's[47], where both of them have studied dilute particulate suspension containing particles' aspect ratio of 3, which is the same as this work.

By fitting relative viscosity and apparent shear rate into Carreau model, we obtained relative viscosity at the low shear rate plateau. The Brownian stress contribution to zero shear rate viscosity results from an O(Pe) perturbation to the orientation distribution. This small deviation

from isotropic is important for getting low Pe viscosity. Therefore, it is comparable to Claeys and Brady's calculation of homogenous anisotropic particle suspension.

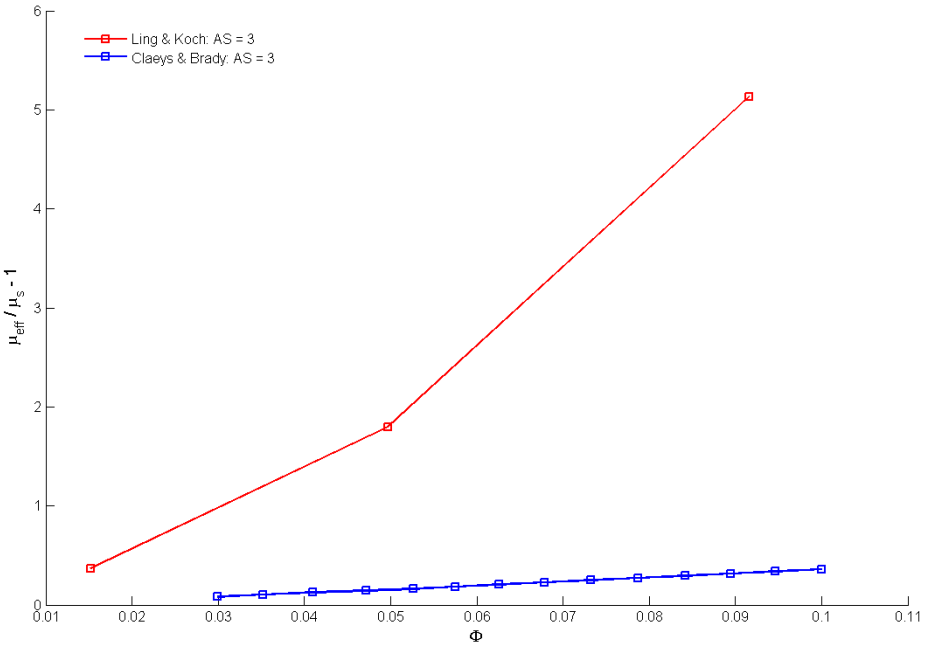

Figure 1-26 Comparison of reduced viscosity from this simulation work and to Claeys and Brady,1993[47]

In Claeys' study, Brownian motion is not taken into consideration; hence, the contribution of Brownian stress is zero, while in our scenario, Brownian motion is accounted for. Therefore, it is expected to see a larger value in our data with respect to Claeys' data. However, we do not have sufficient data to see the linear relationship as a function of volume fraction as seen by Claeys at low volume fraction.

Brenner calculated the intrinsic viscosity of dilute suspension, taking Brownian motion into consideration. Therefore we compare the intrinsic viscosity data from the lowest volume fraction to Brenner's results of suspension containing particles with aspect ratio of 3 from the roatry Peclet number range from 0 to 60. Our data is much larger than that of Brenner's over the same range of Peclet number.

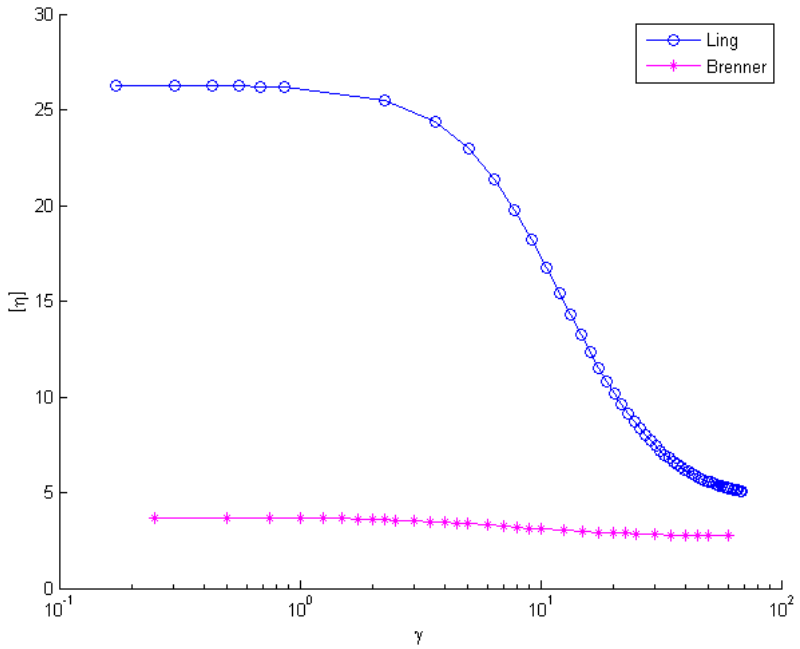

Figure 1-27 Intrinsic viscosity as a function of apparent shear rate, comparing to Brenner's [46] dilute theory

The intrinsic viscosity value from our simulation is much larger than the theoretical prediction from Brenner's dilute theory. It could be attributed for the following three reasons: 1) a non-continuum effect caused by a comparable size between suspending particle and solvent molecule size, this aspect is discussed in section 1.4.2.2.2); DPD thermostat has been given a too high friction coefficient, which artificially increased the value of viscosity; 3) particles aggregation caused by either shear effect or by the mis-assignment on interaction energy parameter.

In this work, the author is interested in relating the microstructure of the particulate suspension, such as particle alignment, orientation distribution function (ODF) and how to use them to account for its rheological behavior, such as shear viscosity. In addition, we would like to additionally investigate the existence of non-continuum effect on rheological behavior that could be possibly caused by a comparable size between suspending particle and solvent molecule.

The first aspect is studied by obtaining positional information of molecules from simulation to post process these information to get snapshots of particle alignment, orientation distribution

function, as well as average moments information. On the other hand, the second aspect of this study is informed from comparing moments calculation from simulation with Brenner's dilute theory prediction.

1.4.2.2 Particle alignment and Orientation Distribution Function (ODF)

As discussed in the Introduction to this thesis, chapter one, the particle orientation has a significant effect on the rheology of the suspension. A direct visualization of particle alignment within the same suspension system establishes a self-explanatory relationship between microstructure and its effect on rheology.

1.4.2.2.1 Particle alignment

The competition between Brownian forces and hydrodynamic forces determines particle alignment. It is significant to identify the particle alignment in a quiescent environment. For concentrated systems, depending on the volume fraction, a quiescent suspension undergoing Brownian motion may still exhibit complex structure and ordering. In contrast, for dilute suspensions, Brownian motion should result in a random state. Accordingly, we examine particle alignments in two conditions, at $Pe_r = 0$ and at finite Pe_r.

Both dilute and semi-dilute suspensions at $Pe_r \to 0$ are expected to exhibit a random distribution state. As Pe_r increases, hydrodynamic force will begin to dominate, and hence particles will tend to become more aligned. We observed that, at each volume fraction, we can see more particle alignment along the flow field as Pe_r increases. Comparing the change in particle alignment from Pe_r from 0 to 8, corresponding to the dilute and semi-dilute regimes respectively, we observe more alignment associated with a semi-dilute suspension.

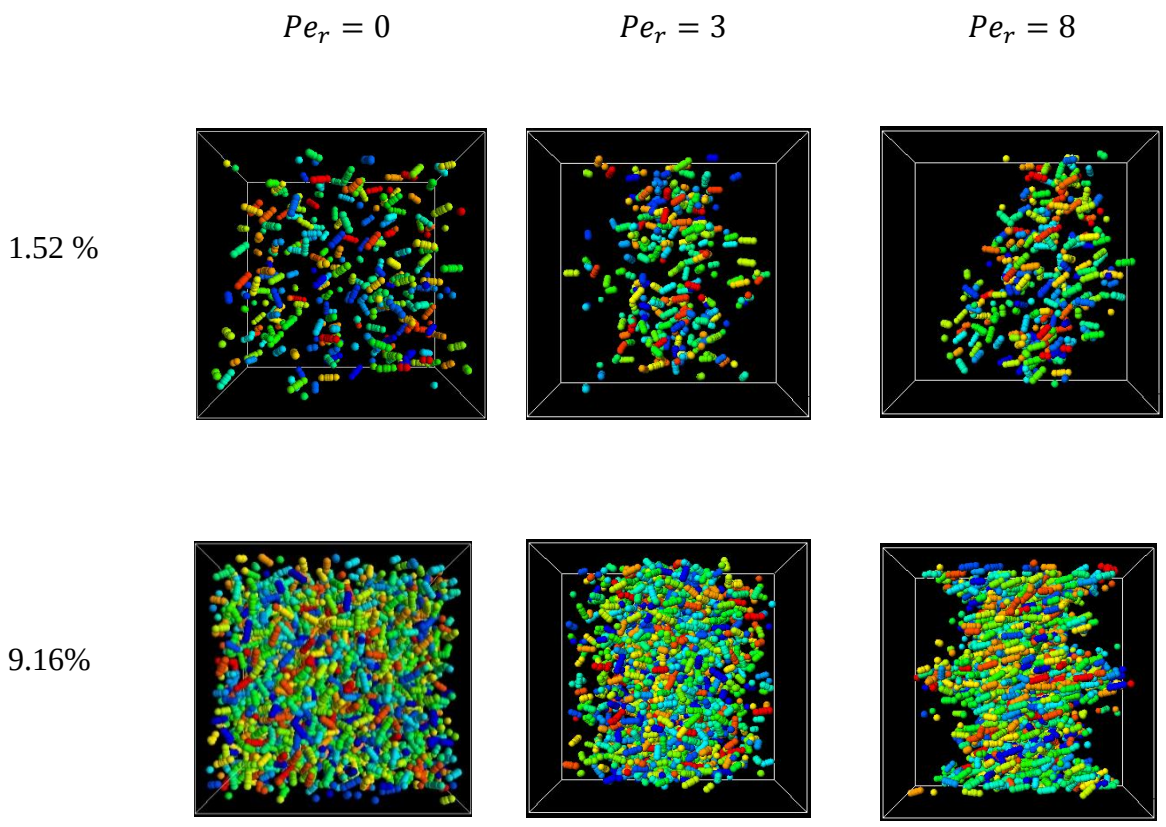

Figure 1-28 Particle alignment in two volume fractions at $Pe_r = 0$ and finite Pe_r

1.4.2.2.2 Orientation Distribution Function (ODF)

In order to further quantify the change in shear-induced microstructure, we plotted the unit principal vector on a unit sphere. The unit principal vector is defined as the vector pointing from the center of mass of the particle toward the tip of the particle. To allow fair comparison, each orientation distribution function plot contains 4000 particles.

Each ODF is plotted in three views, which are flow-gradient, flow-vorticity, gradient-vorticity, so as to compare the effect of flow on particle orientation. By comparing ODF at the same volume fraction but different shear rates, see Figure 1-29, we can tell by ODF the effect of flow enhances the migration of particles to direction of flow.

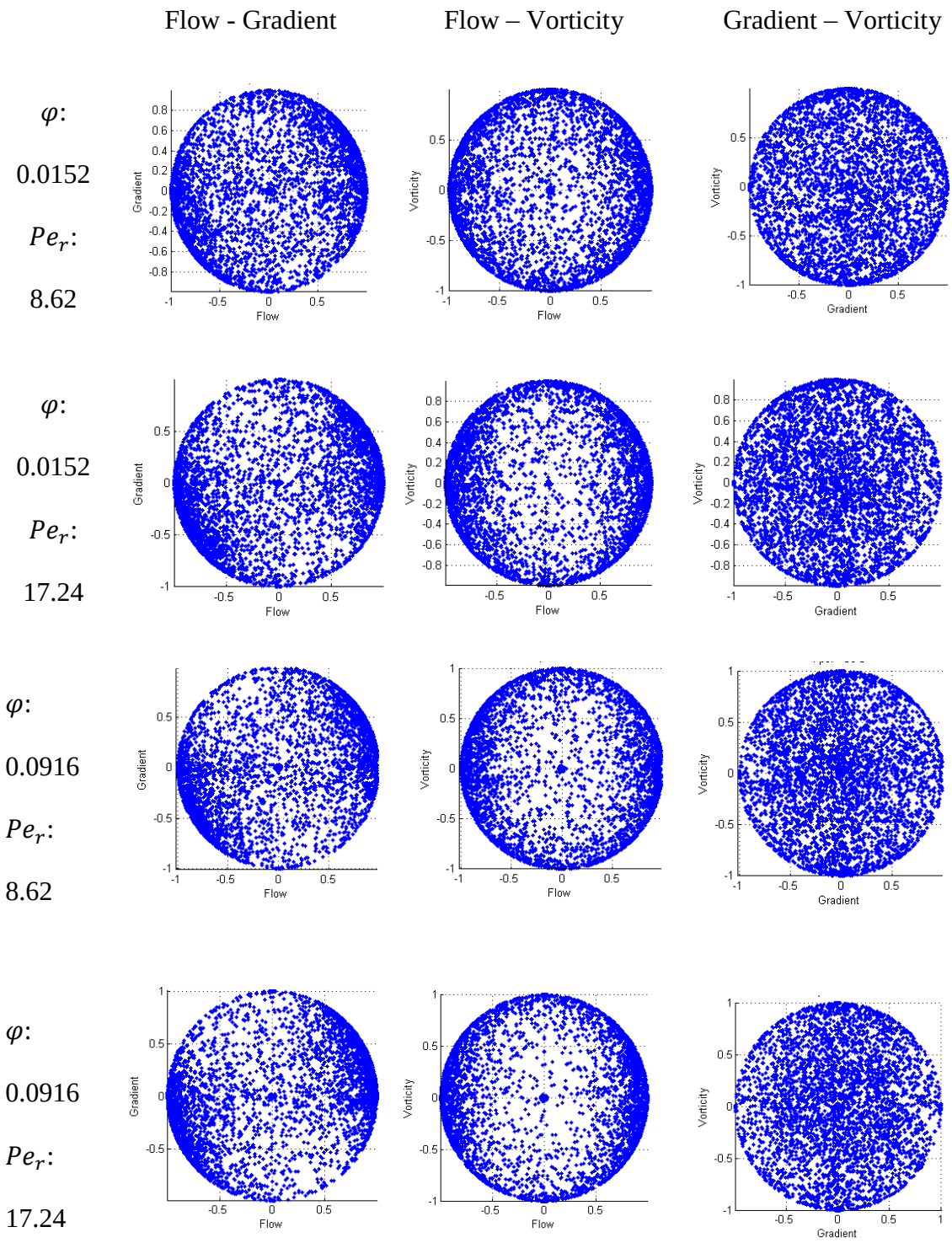

Figure 1-29 Orientation distribution function (ODF) for suspensions containing 1.52% and 9.16% particle loadings at Pe_r of 8.62 and 17.24. The ODFs are plotted in three views, flow-gradient, flow-vorticity, and gradient voritcity. They are used to observe the effect of shear on particle alignment at different volume fractions.

The effect of concentration on particle orientation can be extracted by comparing ODF of three particulate suspensions under the same shear rate. As shown in Figure 1-30, although quite subtle, it could still be told that 9.16% volume fraction are the most susceptible to the flow effect: it exhibits the most migration of particles toward the flow direction.

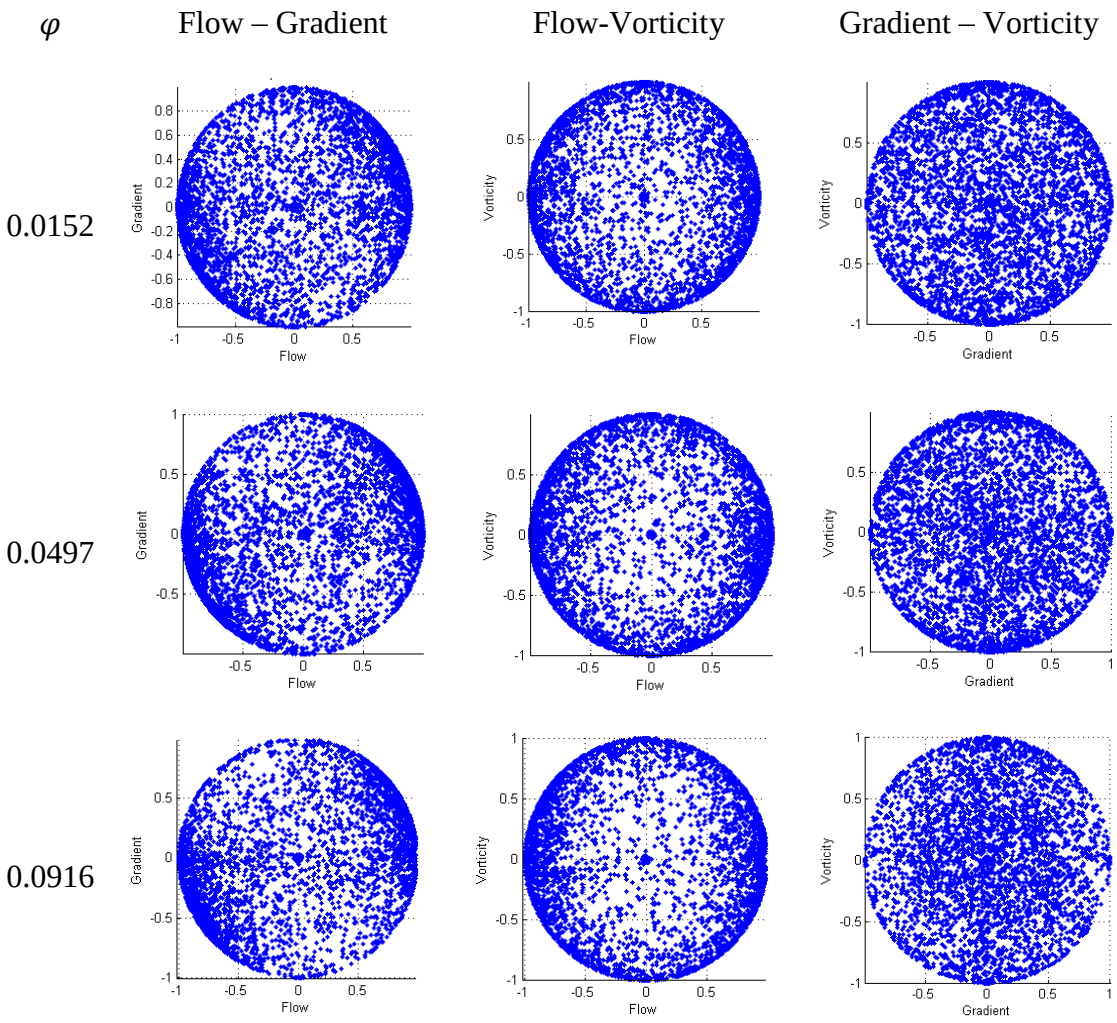

Figure 1-30 Orientation distribution function for suspensions containing volume fraction at 1.52%, 4.97%, 9.16% at the same shear rate $Pe_r = 8.62$. This is used to see how concentration regime would contribute to particle alignment

This observation is consistent with Doi-Edward theory, as nL^2 increases up to a value larger to 1, the particles interact with each other through steric interaction, therefore causing a decrease in rotary diffusivity, and this decrease in diffusivity gives more alignment. The increased alignment increases the Brownian stress which results in a higher zero shear viscosity. However, the increased particle alignment reduced the hydrodynamic stress. This is again consistent with the

visualization from Figure 1-28, where at high Peclet number, the particles are more aligned along the flow field than its counterpart at lower volume fraction.

We then non-dimensionalize the relaxation time $\boldsymbol{\lambda}$ by the rotary diffusivity D_r for an isolated particle. Since $\langle \boldsymbol{u}(t)\boldsymbol{u}(t+\tau)\rangle = \exp(-4D_r\tau)$, $0.25/D_r$ is therefore the rate of decay of orientation correlation function for dilute rods.

Table 1-14 $\boldsymbol{\lambda D_r}$ at each volume fraction $\boldsymbol{\varphi}$

ϕ	λD_r
0.0152	0.112
0.0497	0.393
0.0916	0.840

From 4.97% suspension, we can see the value of λD_r is larger than 0.25. This indicates that the particles do not rotate freely, whose motion rather are interfered by additional disturbances, could be steric interaction, or could be due to aggregation effects caused by either shear or simulation artifacts.

1.4.2.2.3 Average Orientation Moments

Moments are computed first to further quantify the orientation of spherocylinder particles. This is done by taking the ensemble average of principal unit vector p, which is defined as the vector pointing from center of mass of each particle to the front tip of the spherocylinder.

$$< p_i p_j > = \frac{1}{N}\sum_{1}^{N}(p_i^N)(p_j^N) \qquad 1\text{-}35$$

$$< p_i^2 p_j^2 > = \frac{1}{N} \sum_{1}^{N} (p_i^N)^2 (p_j^N)^2 \quad \text{1-36}$$

In addition, as we would also like to address the question how the effect of non-continuum would affect the flow behavior, if ever existing. Therefore, first of all, it is necessary to first check if the non-continuum effect exists. We then compared our computation to the orientation calculation from Brenner's dilute theory. Brenner has computed not only intrinsic viscosity of a dilute suspension of axisymmetric Brownian particles, but also the goniometric factor which can be converted in terms of orientation moment information.

$$p_x = 2\, sin\theta cos\varphi \quad \text{1-37}$$

$$p_y = \ 2\, sin\theta\ sin\varphi \quad \text{1-38}$$

$$p_z = cos\theta \quad \text{1-39}$$

The quantities that we have compared to with Brenner's results are intrinsic viscosity, which is defined as

$$[\eta] = \lim_{\varphi \to 0} \frac{\eta - \mu_0}{\varphi \mu_0} \quad \text{1-40}$$

where η is the apparent viscosity of the dilute particulate suspension, μ_0 being the solvent medium viscosity, and φ being the volume fraction of the dilute suspension.

The goniometric factors from Brenner's work that we have compared to are $< sin^2\theta\ sin2\varphi >$and $< sin^2\theta >$, and these two quantities can be converted to moments information based on the following trigonometric relationship:

$$< p_z^2 > = 1 - < sin^2\theta > \quad \text{1-41}$$

$$< p_x p_y > = \frac{1}{2} < sin^2\theta\ sin2\varphi > \quad \text{1-42}$$

Assuming 1.52% particulate suspension is a dilute suspension, therefore, by applying the definition of intrinsic viscosity to this particulate suspension.

The data is also plotted with Brenner's data on a same plot to see the deviation from theoretical prediction, as shown in Figure 1-27.

From the plot we can see a large discrepancy from Brenner's work and results from this work. The origin of this large discrepancy could be due to either simulation artifacts such as a too large DPD friction coefficient, a mis-assignment of interaction potential that could very likely cause aggregation during the shear flow, or it could be caused by non-continuum effect.

To investigate the effect of non-continuum effect, we compare our moments' information to Brenner's calculation on goniometric factor. Figure 1-31 and Figure 1-32 show these two comparisons. The data from this simulation work align quite well with Brenner's work at especially low Peclet number very well. This being said, the particles are aligned in a right way under Brownian motion as well as hydrodynamic stress even when the continuum hypothesis even holds. It further implies any non-continuum effect does not seem to influence the orientation moments – or in other words the suspension structure. It is possible that non-continuum could have more effect on the stress for a given structure than it does on the structure itself. Therefore, the discrepancy can then be attributed to the simulation artifacts. Future work needs to be carried out more carefully to obtain more reliable rheological results.

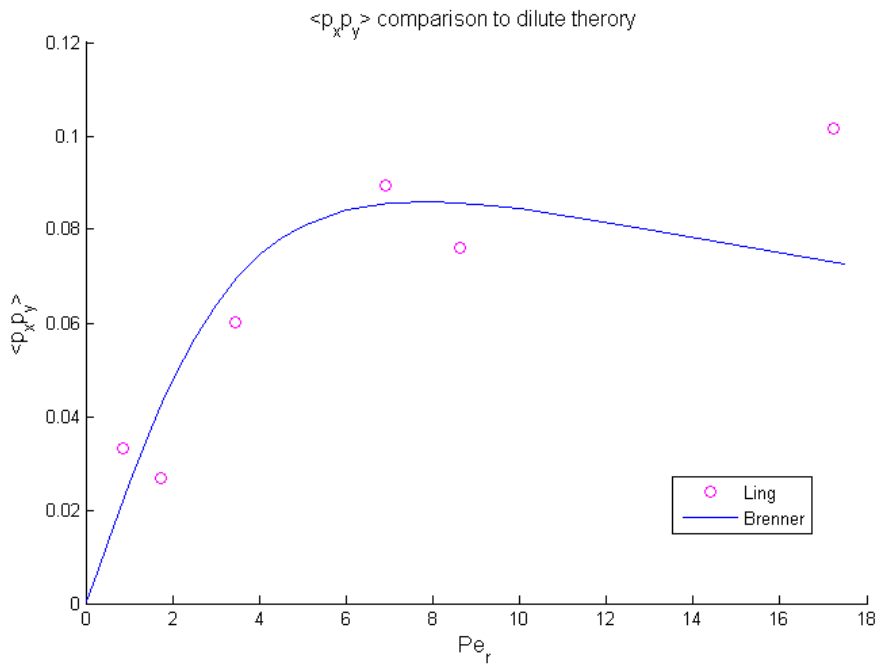

Figure 1-31 Comparison on $\langle p_x p_y \rangle$ of this simulation work and Brenner's calculation based on dilute theory

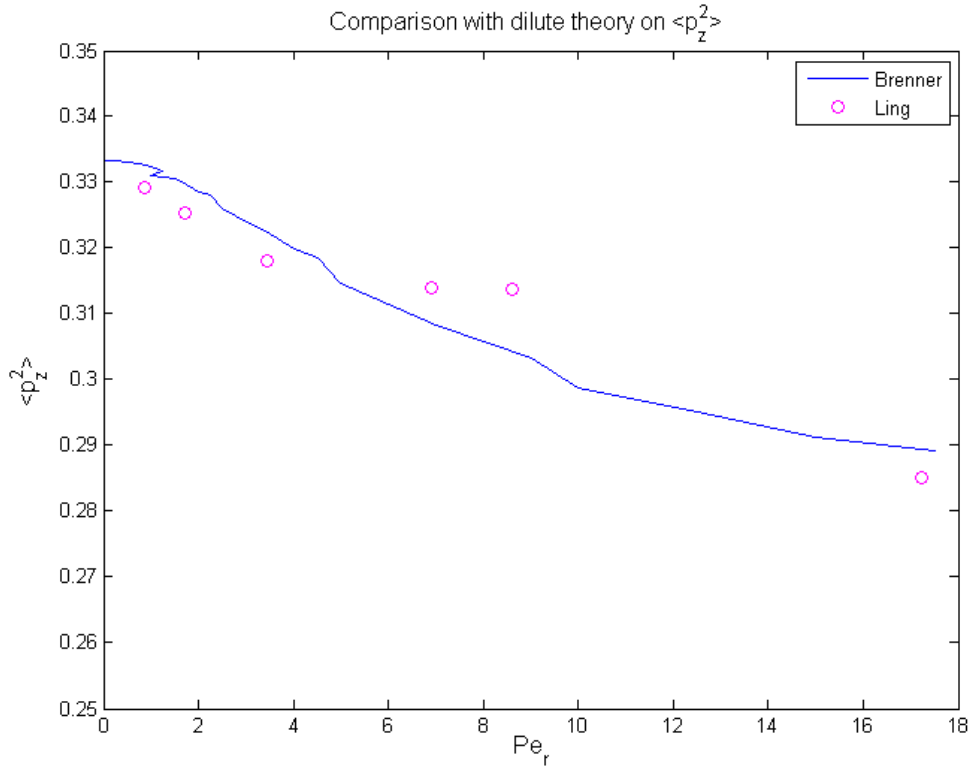

Figure 1-32 Comparison on $< p_z^2 >$ of this simulation work and with Brenner's calculation based on dilute theory

1.4.3 Suggestions for future studies

The motivation for this study would be to see the discrete solvent and particle orientation effects in a simulation where there is no particle-particle interaction or aggregation. Therefore, the interaction potential parameters will be modified to result in a zero Hamaker constant. To result in a zero Hamaker constant, a simple way is to assign the interaction energy between solvent and particle one half of that between solvent and solvent.

On the other hand,in order to conserve the available time and computer resources, rather than running multiple-particle simulations, we designed systems containing one single particle with volume fractions in the dilute regime. In this regime, since the particles do not interfere with each other, running a single-particle simulation is the same as running multiple-particle simulations, but the average period should be extended to long enough to obtain good statistical data for stress computation. For non-equilibrium simulations, each simulation cell is applied with an amount of deformation equal to 1000.

1.4.3.1 Non continuum effect

In our simulation, due to the fact that the size of the particles is comparable to that of the solvent molecules, treating solvent as a continuum is no longer an appropriate assumption. Therefore, it is interesting to investigate the effect of non-continuum fluid behavior on suspension rheology.

We designed our study to first investigate how intrinsic viscosity deviates from continuum prediction due to the impact of a discrete solvent environment. We designed suspension systems containing only a single sphere[48] at volume fractions up to 0.03. For each suspension, we imposed a simple shear flow and determined the zero-shear viscosity corresponding to that volume fraction. Therefore, the slope of the relationship between the reduced shear viscosity and

the volume fraction will inform us of the intrinsic viscosity. As the size of the particle increases, the non-continuum effect should get weaker, and hence it is more appropriate to treat the solvent as a continuum. We then increase the size of the suspending particles and expect the difference between the intrinsic viscosity in the simulation and the theoretical prediction to become smaller.

1.4.3.2 Particle moments calculation from single particle system

The following chart tabulated the systems and particle specifications we have designed.

We also designed systems containing non-spherical particles of different shapes and aspect ratios. The same protocol applied previously to the case for spheres is adopted to study prolate particle suspensions. **Table 1-15** summarizes the systems that we have designed to conduct this study.

Table 1-15 Single particle suspension designed to study non-continuum effect

Particle Shape	Size Specifics	Aspect Ratio	Volume Fraction	Shear rate
Sphere	Diameter: 3 Diameter: 5	1	0.5%, 1%, 1.5%, 2%,2.5%	Equilibrium; 0.0025; 0.005; 0.01
Sphero-cylinder	Long axis (a) = 3 Short axis (b) = 1	3	1%, 1.5%, 2%, 2.5%	Equilibrium; 0.0025; 0.005; 0.01
	Long Axis (a) = 11 Short Axis (b) = 1	11	0.1%, 0.5 %	Equilibrium

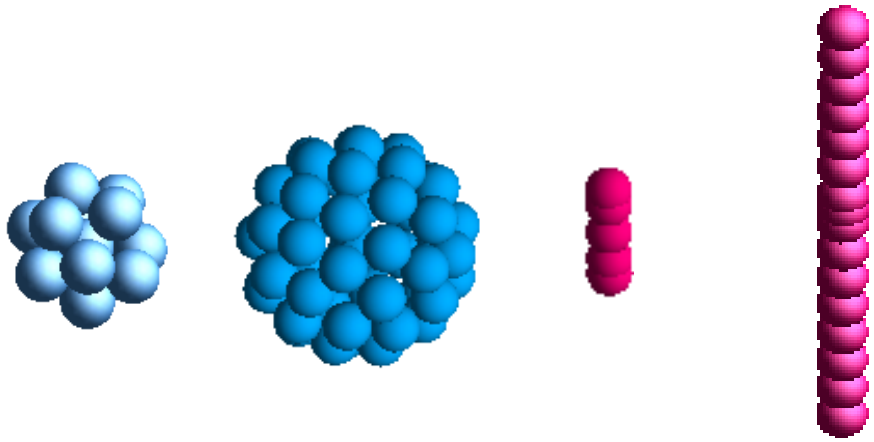

Figure 1-33 Suspending particles considered in this study. a) sphere, D=3 b) sphere, D=5 c) sphero-cylinder, aspect ratio 3, major axis length 3, minor axis length 1 d) sphero-cylinder, aspect ratio 11, major axis length 11, minor axis length 1

We were inspired by work from Petrich and Cohen,[20] where they related fiber orientation distribution in order to account for the stress-microstructure relationship. This work compared their experimental findings to theoretical predictions. To investigate the non-continuum effect on anisotropic particle systems, we would also like to compute the moments information from the orientation distribution, and then to relate these to the rheology predicted by continuum theory. These moments information are as follows:

$$< p_x^2 p_y^2 >, < p_x^3 p_y >, < p_x p_y^3 >, <p_x p_y p_z^2>$$

Shear stress, normal stress differences can be expressed in terms of particle moment information.

$$\sigma_{12} = \mu\dot{\gamma}(< p_x^2 p_y^2 >) \quad \text{1-43}$$

$$N_1 = \sigma_{11} - \sigma_{22} = \mu\dot{\gamma}(< p_x^3 p_y > - < p_x p_y^3 >) \quad \text{1-44}$$

$$N_2 = \sigma_{22} - \sigma_{33} = \mu\dot{\gamma}(< p_x p_y^3 > - < p_x p_y p_z^3 >) \quad \text{1-45}$$

It is worth noting that Petrich's results are for non-Brownian high aspect ratio suspesnsions and more general results can be found in Brenner, Leal and Hinch.

1.5 Conclusion

In our preliminary studies, we studied particulate suspension containing sphero-cylinder particles of a moderate aspect ratio of 3 at three volume fractions. We compared shear-induced particle alignment information at different volume fractions in order to understand the contribution of hydrodynamic forces to the particle alignment and how, in turn, this alignment affects the rheology. Using stress computation, direct visualization within the suspension allows us to explain the origin of shear thinning. Orientational distribution functions are used to observe the migration of particles when subjected to shear flow. With comparison to early work by Brenner based on dilute theory, we confirmed that the non-continuum effect does not necessarily exist for this particulate suspension system. Future work will be focused on microstructure- property relationship study on how orientation distribution, average moments can be associated with suspension's bulk behavior.

2 DYNAMICS OF *LIVING* PARTICLE SUSPENSIONS BY FLUID PARTICLE DYNAMICS

2.1 Introduction

Active suspensions have drawn drastic interest within the past several years. Examples of active suspensions are suspensions contain self-propelled microorganisms, swimming cells, and artificial micro-swimmers [49–51]. Self-motility results in new properties of active suspension comparing to passive particle suspensions [52]. Typical examples of active suspensions are suspensions of micro-algae, bacteria and sperm [53,54]. Study of such active systems has fundamental meaning [52], as well as in various technological applications[55–57], in ecology[58], and in medicine [59].

Depending on swimming mechanism of each type of micro-swimmers which results in hydrodynamic interaction between swimmers in suspensions, various interesting phenomena have been reported. Among them: complex rheological behavior of micro-swimmer suspensions [52,60,61]; pattern formation in bacterial suspensions [56,62]; complex motions, enhanced diffusion and spatial correlation in micro-swimmer suspensions [55,63,64]; phototaxis and bioconvection in suspensions of phototactic micro-swimmers [65,66]

2.1.1 Two types of microswimmers

There are two main categories of micro-swimmers: puller-type and pusher-type. One typical representative for puller-type micro-swimmers is Chlamydomonas Reinhardtii (CR), which is a type of green, micro-algae.,see Figure 2-1 (a) (b). Typical examples for pusher-type micro-swimmers are bacterias like Escherichia coli, bacillus subtilis; human spermatozoa, and artificial

microswimmers, see Figure 2-1 (c)-(g). Motility of pusher-type micro-swimmers are enabled by posterior anchored flagella.

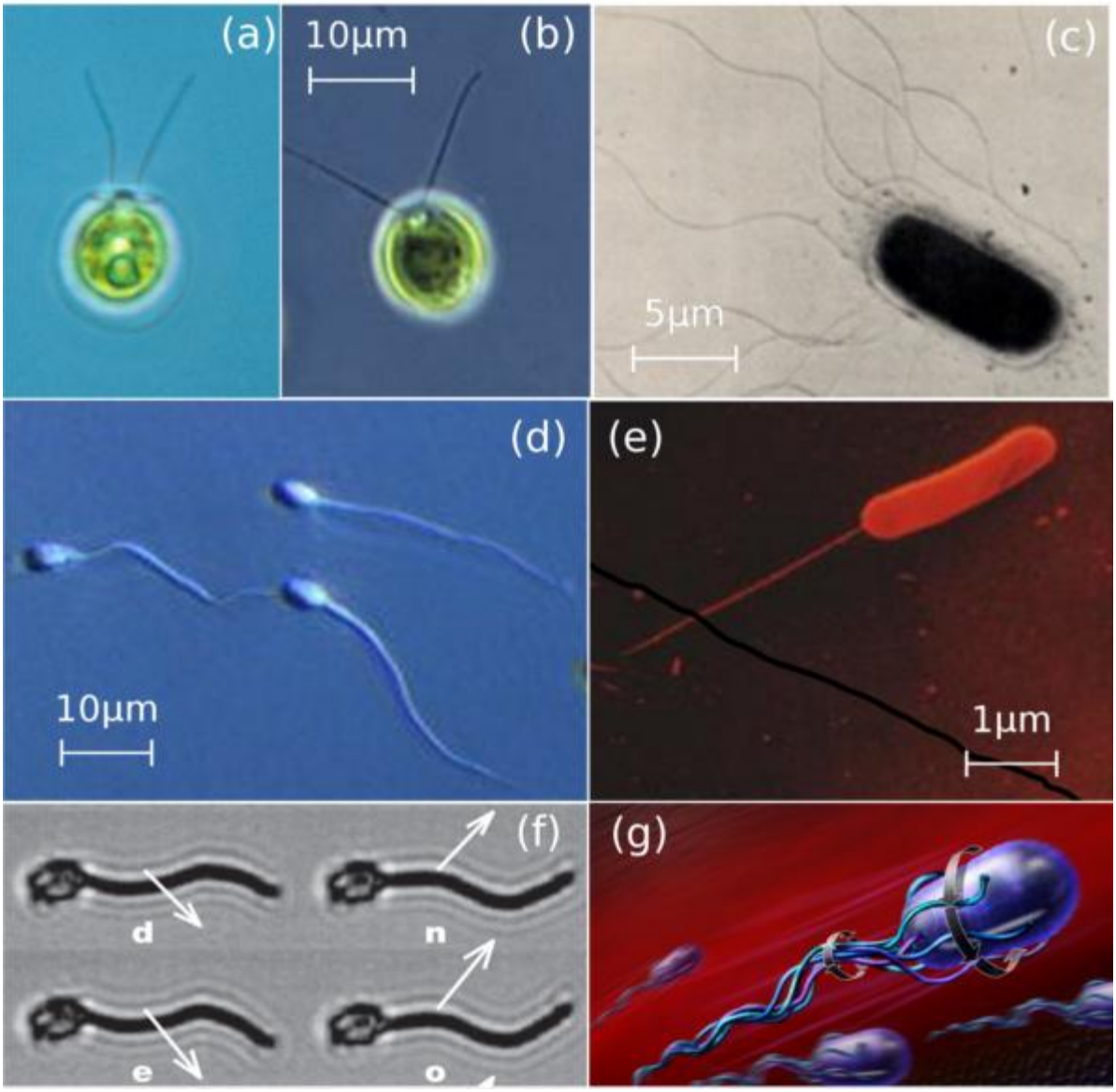

Figure 2-1 Examples of puller type and pusher type micro-swimmers. a) & b) Chlamydomonas Reinhardtii (CR) c) Escherichia coli d) human spermatozoa e) bactillus subtilis f) artificial swimmers g) schematic drawing of artificial swimmers

It is classified based on the how the forces are exerted by the flagella on the surrounding medium. Puller-type micro-swimmers pull the surrounding fluid backward with their front anchored flagella and hence accomplish the forward motion. On the other hand, pusher-type

micro-swimmers propel themselves forward by pushing the fluid backward with their posterior anchored flagella along their moving axis.

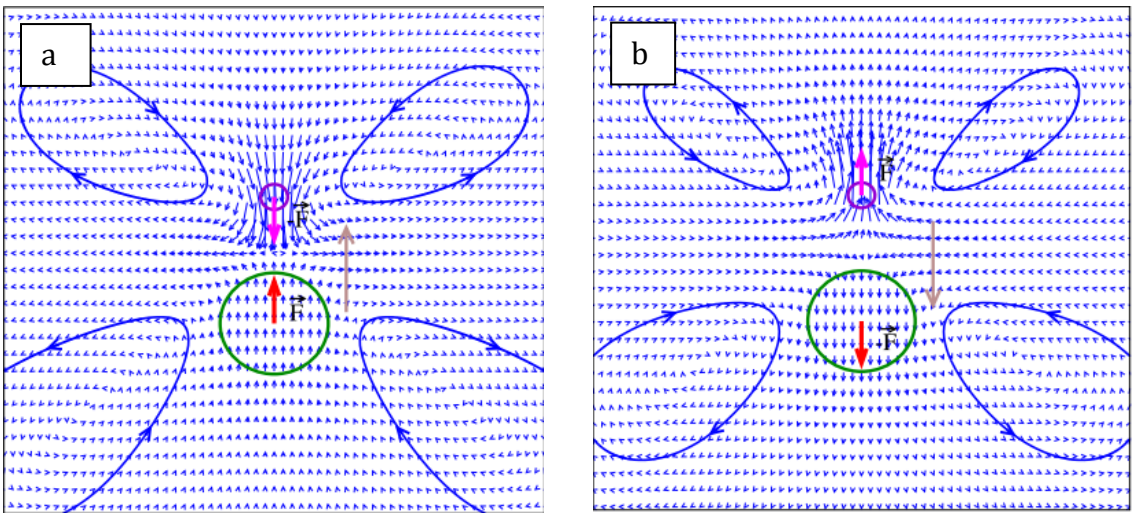

Figure 2-2 Velocity fields and streamlines of two types of micro-swimmers: a) puller-type; b) pusher-type. Brown arrows indicate the moving direction, force dipoles are indicated by the pink and red arrows [67] .

2.1.2 Experimental findings: control of microswimmer suspension using both flow and light [68]

In this study, Chlamydomonas Reinhardtii (CR) is studied, which is a type of microalgae. Other than the fact that it is a puller type microswimmer, it is also phototactic: the algae swim toward a light source. Currently, there is an emerging research involved with understanding how microswimmer can self-organize under external stimulus and flow.

Experiments were carried out where a suspension of micro-algae are subject to a Poiseuille flow as well as light exposure. Similar to what Kessler[69] has discovered in 1985, when he studied a suspension of gravitactic alga subject to gravity, he found the suspension experienced self-focusing of remixing depending on the vertical orientation of the Poiseuille flow; it is found that the phototactic nature of CR can be used to control the motion of the suspension when it is subject to Poiseuille flow. With the combination of flow vorticity and phototaxis, algae

suspension is found to be able to concentrate along the center of flow – a self-focusing phenomenon shown in Figure 2-3. A bright field microscope is used to collect the traces of microswimmers in a square channel of 1mm × 1mm. A light source can be placed either upstream or downstream as shown in Figure 2-4. Since the Reynolds number associated with swimming alga is about 2.5×10^{-4}, it is weak enough that for passive particles they are only able to rotate in a Poiseuille flow with no net migration cross-stream. However, it is not quite the case in microswimmers: when there is no light exposure, the microswimmers rotate responding to the flow, and as there is no preferred orientation, they oscillate in a very small scale and hence observed as no net translation cross stream; however, when there placed a light source upstream, the microswimmers are observed to migrate cross-stream and focus along the center of flow.

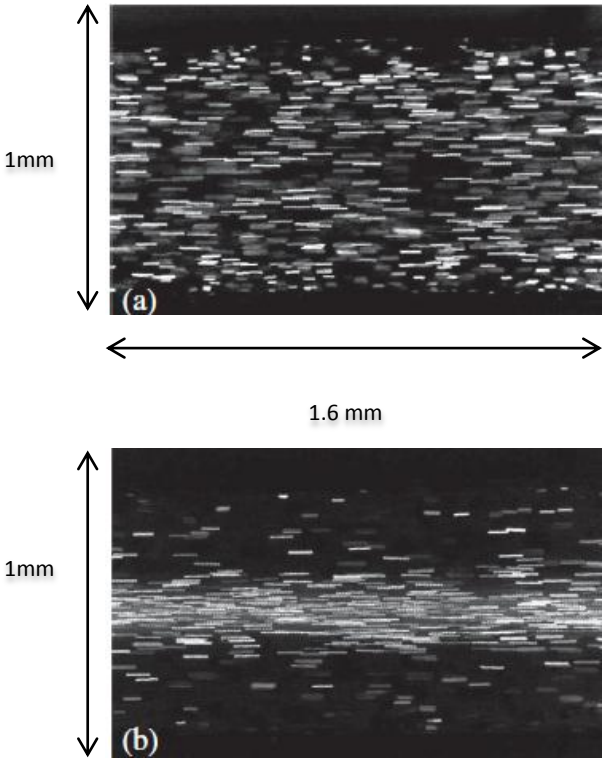

Figure 2-3 Self-focusing phenomenon of an algae suspension

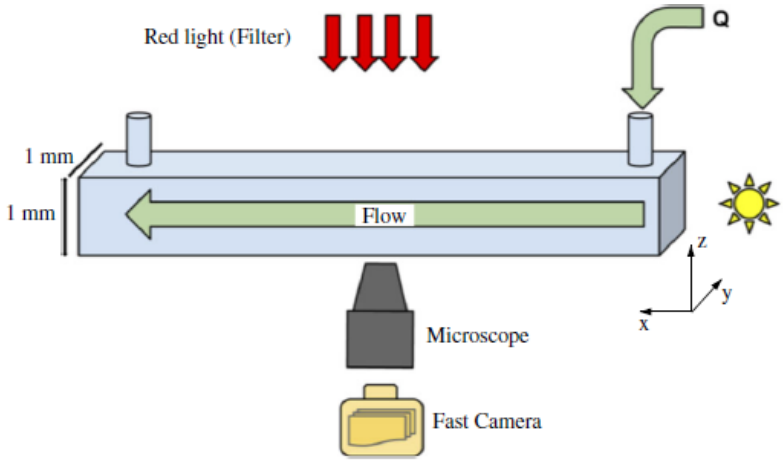

Figure 2-4 Experiment setup

Moreover, the self-focusing phenomenon is found to be flow rate sensitive. It is only observed within a flow rate range from 0.03 ml/min to 0.09 ml/min, which in terms of shear rate averaged between the center of the squared channel and the walls gives 1.0 s^{-1} to 3.0 s^{-1}, as shown in Figure 2-5. Beyond this range, the flow is either so low that is insufficiently strong for

microswimmers to concentrate or too high that microswimmers do not have time to reorient. To explain this physical fact, here we introduce a dimensionless number D_1, which is defined as the product of wall shear rate and cell reorientation time, refer to section 2.6.3 for more details. When D_1 is $\sim O(1)$, the self-focusing phenomenon can be observed. The experimental conditions that led to the observation of self-focusing fall into this regime, otherwise, self-focusing phenomenon is not observed.

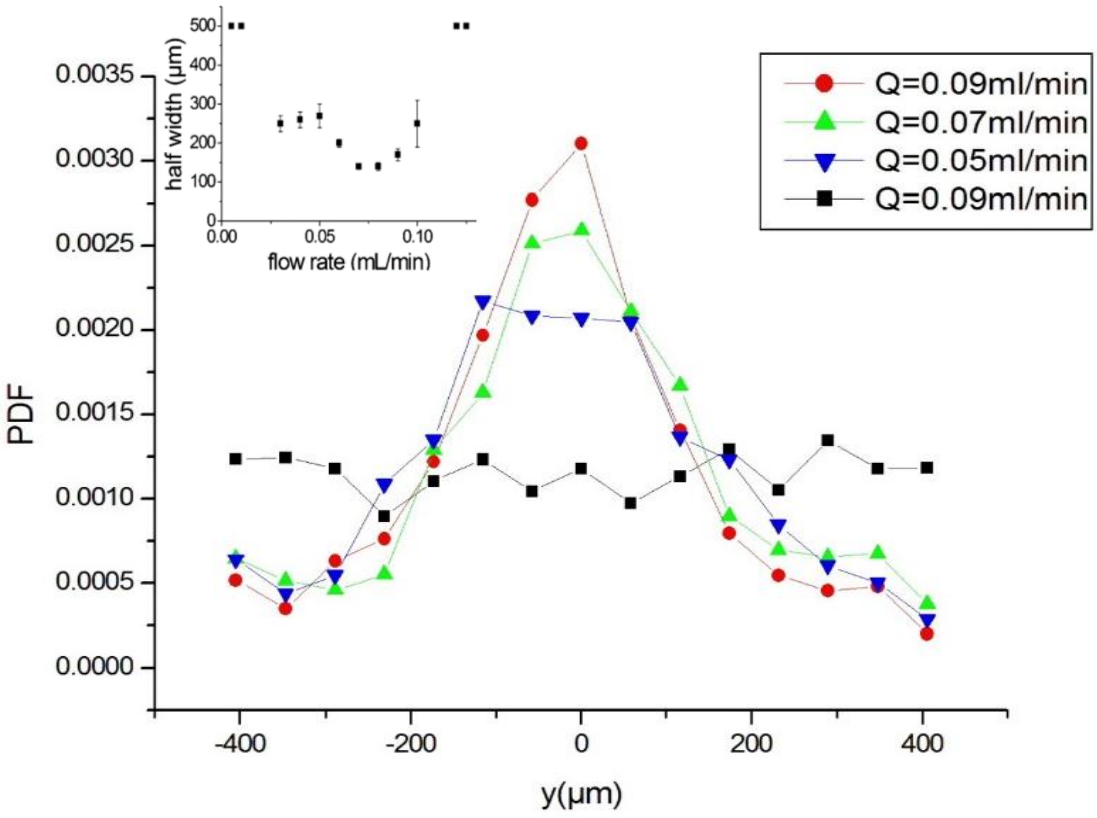

Figure 2-5 Probability distribution function of CR in the Poiseuille flow. Inlet: Half band width as function of the flow rate.

On the other hand, this self-focusing phenomenon is also reversible: when the light is switched on and off, self-focusing and remixing takes place alternatively responding to the external light source, as shown in a saw-tooth pattern. When self-focusing state takes place, hydrodynamic interaction is reinforced by the concentration of the cells around the center. However, when the light is turned off from the focusing state, hydrodynamic interactions and self-diffusivity between the cells then cause themselves to mix back in the fluid.

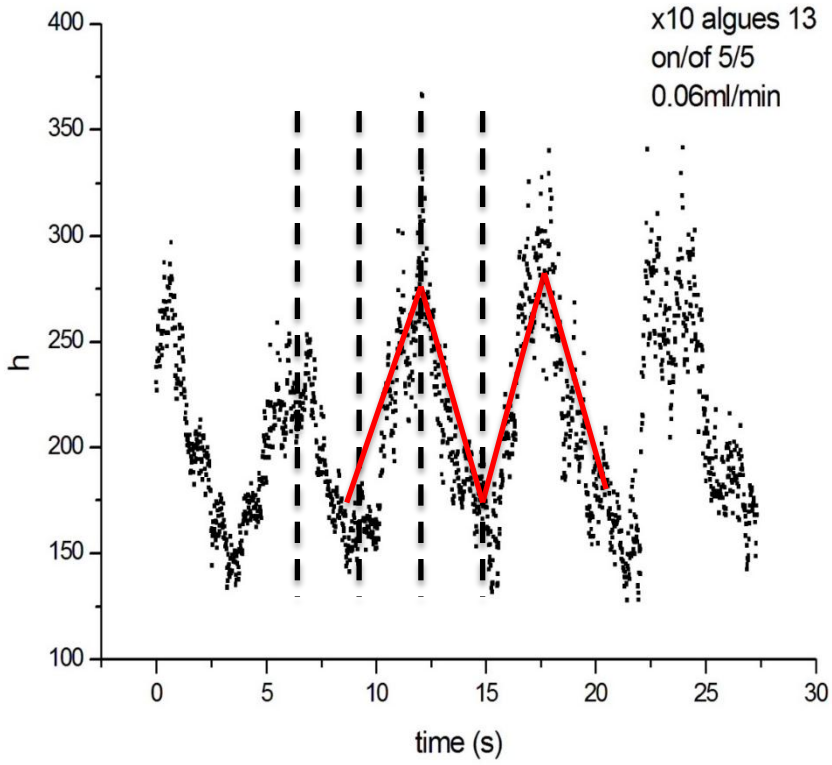

Figure 2-6 Band width of CR at a flow rate of 0.06 ml/min, with light exposure interval of 2.5 seconds.

The discovered self-focusing phenomenon from experiments is believed to be a promising solution to remove the excess water during biofuel algal production, which is the current bottleneck challenge for this process. However, to realize this goal, on the other hand, this discovery needs to experience the scaling-up challenge so as to succeed in industrial applications. Regardless of these challenges, it is still interesting to further understand the

underlying mechanisms so as to better contribute to the solution, in our group, we proposed a theoretical model and to approach this problem from numeric simulation. This work is from a theoretical perspective and hence targets at providing insightful explanation to the observed physical phenomenon.

2.2 Micro-swimmer Model and Light Effect Mechanism

2.2.1 Micro-swimmer Model - A dipole force model

The model we employed accounts for the propulsive forces exerted by a pair of front-anchored flagella onto the medium as a pair of downward pointing forces; and the drag force exerted by the body on the surroundings is represented by the upward pointing force[67]. Figure 2-7 demonstrates the model employed in this work.

The micro-swimmer particle is a force-free and torque-free particle due to the fact that each particle is an isolated body and neutrally buoyant due to absence of sedimentation, and therefore the viscous drag force has to be balanced by the self-propulsive force when the particle is in motion. However, even though the cell is torque-free, it can still change orientation due to light attraction.

To be able to reproduce exactly the behavior of flagella is very difficult due to the back-and-forth, non-reciprocal motion. Nonetheless, the beating frequency of the flagella is high enough that we can thus represent the forces exerted by the flagella onto the medium by a pair of downward pointing force, as shown in the model. It is hence a temporal average of a series of instantaneous beating motion of flagella in one single stroke.

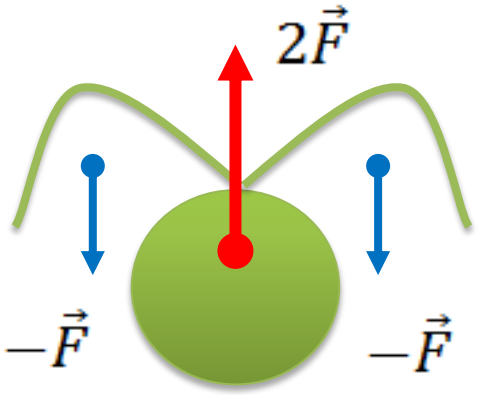

Figure 2-7 A force dipole model for micro-swimmer[67]

2.2.2 Light effect

Due to the photo-tactic nature of this micro-alga, it orients itself toward the direction of light after an internal response time. Each cell is initially assigned an internal response time in a random fashion from 0 to 50 τ. The reorientation time of each cell is set to be 50 τ. With τ being the simulation time unit. The time step size employed in this work is 0.001 τ. At every time step, actual simulation time is compared to the cell reorientation time. If the current simulation time is less than the cell internal reorientation time, then the internal reorientation time remains unchanged; In contrast, then the internal reorientation time is accumulated by another 50τ.The physical process of reorientation is realized by changing the relative position of flagella to the cell body. Therefore, being a torque-free and point particle, the cell changes its orientation and the direction of swimming without involving external torque exerting on the body.

2.3 Fluid Particle Dynamics

2.3.1 Introduction

The Fluid Particle Dynamics method (FPD) is used to simulate a suspension of colloidal or non-colloidal particles at low Reynolds number. It is one of the simulation methods among all the

other predominant ones, like Brownian Dynamics [33,70], Stokesian Dynamics [71] or Lattice Boltzmann method [72], that can be adopted in approaching particulate suspension problems on a continuum scale.

The concept of Fluid Particle Dynamics was initially devised by Tanaka [73] in two dimension suspension problems, and later developed by Peyla into three dimension scenarios [74,75]. What makes this concept easier to implement than the conventional approaches is that one can bypass the moving boundary conditions by considering the particle region to be higher viscosity fluid particle, while the surrounding fluid medium to be with a lower viscosity region. The contrast between particle region to the surrounding fluid region is set to be a ratio which is high enough that the particle region can be seen as if it were a solid particle [67]. This kind of method is also known as 'penalty method' [76]. Moreover, the hydrodynamic interaction is automatically included as the Navier-Stokes equation is solved over the entire domain rather than only on the fluid domain.

This method is efficient when one deals with suspension of rigid particles suspending in a Newtonian medium, while it is not sufficient if one approaches suspension problems containing deformable particles, like vesicle or red blood cell, whose shapes deform upon responding to the flow.

2.3.2 Theory of Fluid Particle Dynamics

The motion of incompressible fluid is described by the Navier-Stokes equation and the incompressibility condition:

$$\rho\left(\frac{\partial \boldsymbol{v}}{\partial t} + \boldsymbol{v} \cdot \nabla \boldsymbol{v}\right) = \nabla \cdot \boldsymbol{\sigma} + \boldsymbol{f} \qquad 2\text{-}1$$

$$\nabla \cdot \boldsymbol{v} = 0 \qquad 2\text{-}2$$

where $\boldsymbol{v}$ is the velocity field of the fluid, ρ is the fluid density which is assumed to be the same for the particles and the solvent. **f** represents the external and internal force field (for example exerted by a swimmer) per unit volume acting on the fluid. The stress tensor $\boldsymbol{\sigma}$ is given by the Newtonian law:

$$\sigma_{ij} = -p\delta_{ij} + \eta(\partial_i v_j + \partial_j v_i) \qquad 2\text{-}3$$

where η is the viscosity of the fluid and p the pressure of the pressure field.

Considering a colloidal suspension containing n particles, whose existences are denoted by the auxiliary field:

$$\varphi_n(\boldsymbol{r}) = \frac{1}{2}[1 + tanh(\frac{a - |\boldsymbol{r} - \boldsymbol{r}_n|}{\xi})] \qquad 2\text{-}4$$

With ξ represents the fluid-particle interface thickness where viscosity decays from the particle viscosity η_p to the solvent viscosity η_s, and a the size of the particles. So, the effective radius of the beads is $R_{eff} \simeq a + 2\xi$.

The particles are considered as more viscous fluid particle region by being assigned a higher viscosity η_p, and the fluid region is assigned a lower viscosity n_s . Literally, the solid particle effect will be achieved when the ratio $\frac{\eta_p}{\eta_s}$ is set to infinity. In this work, the solid particle effect can be achieved when this ratio is set to be 100, where no flow recirculation can be found inside the particle region at this ratio[67].

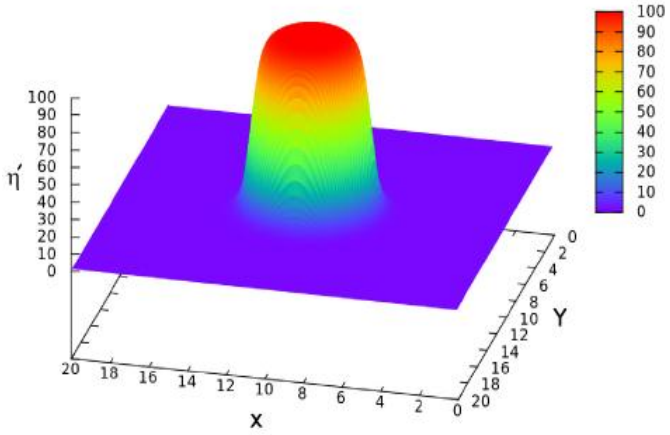

Figure 2-8 Viscosity field around one particle[67]

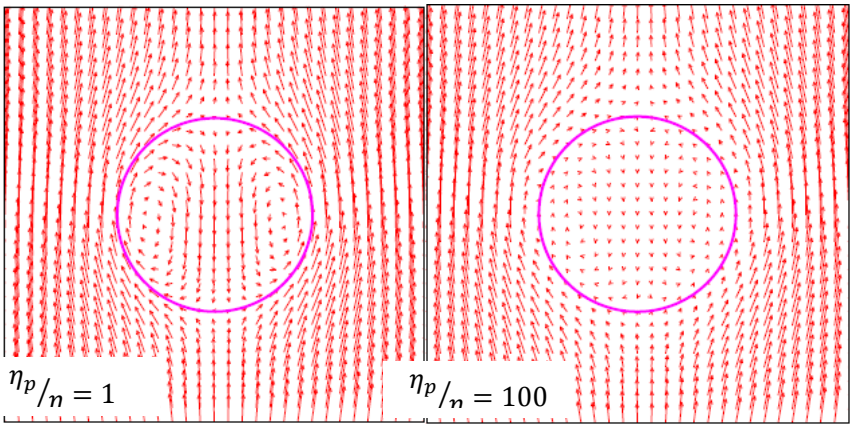

Figure 2-9 Velocity fields of stokes flow past around a sphere at different viscosity contrasts[67]

Hence, the viscosity field of the entire suspension domain can be described by a position dependent function

$$\eta'(\boldsymbol{r}) = \eta_s + (\eta_p - \eta_s) \sum_{n=1}^{N} \varphi_n(\boldsymbol{r}) \qquad 2\text{-}5$$

with which it guarantees that at a far enough distance, the local viscosity is the solvent viscosity η_s, while inside the particle, the local viscosity is η_p.

Therefore, the Navier-Stokes equation can be written in the following form, where $\eta(\boldsymbol{r})$ is the viscosity field on the whole domain.

$$\rho\left(\frac{\partial \boldsymbol{v}}{\partial t} + \boldsymbol{v}\cdot\nabla\boldsymbol{v}\right) = -\nabla P + \nabla\cdot[\eta(\boldsymbol{r})(\nabla\boldsymbol{v} + \nabla\boldsymbol{v}^T)] + \boldsymbol{f} \qquad 2\text{-}6$$

The Navier-Stokes equation along with the incompressibility condition $\boldsymbol{\nabla}\cdot\boldsymbol{v} = 0$ are solved numerically by the Projection Method on a three dimensional MAC grid.

2.4 The Projection Method

The 'Projection Method', which is an explicit, finite difference scheme is employed in this work to solve numerically the time-dependent Navier-Stokes equation under incompressibility condition. The explicit version of this method was proposed by Fortin et. al in 1971 based on the initial and original proposal by Chorin and Temam [77]. The method can be divided into three main steps, and the core idea is to break down the Navier–Stokes equation **2-1** into two equations by introducing an intermediate v^*. The first step is to calculate the intermediate velocity v^* after discretizing equation 2-6 in time by omitting the pressure term.

$$\frac{v^* - \boldsymbol{v}^n}{\delta t} + (\boldsymbol{v}\cdot\nabla)\boldsymbol{v} = \frac{\boldsymbol{\nabla}[\eta(r)(\boldsymbol{\nabla v} + (\boldsymbol{\nabla v})^T)]}{\rho} + \frac{\boldsymbol{f}}{\rho} \qquad 2\text{-}7$$

$$\boldsymbol{v}^* = \boldsymbol{v}^n + \delta t\left\{\frac{\boldsymbol{\nabla}[\eta(r)(\boldsymbol{\nabla v} + (\boldsymbol{\nabla v})^T)]}{\rho} + \frac{\boldsymbol{f}}{\rho} - (\boldsymbol{v}\cdot\nabla)\boldsymbol{v}\right\} \qquad 2\text{-}8$$

One then calculates the divergence free velocity field v^{n+1} at time step n+1 by

$$\frac{\boldsymbol{v}^{n+1} - \boldsymbol{v}^*}{\delta t} + \frac{\boldsymbol{\nabla}P}{\rho} = 0 \qquad 2\text{-}9$$

Note if we combine equation 2-7 and 2-9, the introduced intermediate $\boldsymbol{v}^*$ will cancel and we will again obtain equation 2-6 discretized in time.

By taking divergence of equation 2-9 and using the impressibility condition $\boldsymbol{\nabla}\cdot v^{n+1} = 0$, we get

$$\boldsymbol{\nabla} \cdot \left(\frac{\boldsymbol{\nabla} P}{\rho}\right) = (\nabla \cdot \boldsymbol{v}^*)\delta t \qquad 2\text{-}10$$

Or,

$$\Delta P = \rho(\boldsymbol{\nabla} \cdot \boldsymbol{v}^*)\delta t \qquad 2\text{-}11$$

We solve numerically Poisson equation, equation 2-11 to get pressure field P by using the intermediate velocity field $\boldsymbol{v}^*$, this is the second step of Projection Method. At last, one gets the velocity field at time step n+1, $\boldsymbol{v^{n+1}}$ by equation 2-8.

$$\boldsymbol{v^{n+1}} = \boldsymbol{v}^* - \frac{\delta t}{\rho}(\boldsymbol{\nabla} P) \qquad 2\text{-}12$$

Hence we obtain the velocity field $\boldsymbol{v^{n+1}}$, and pressure field P^{n+1} through Projection Method by introducing an intermediate velocity.

2.5 Simulation Details

To study the effect of flow rate and light on the flow behavior of the micro-swimmer particles, we simulate suspensions containing mono-disperse rigid spheres. A pair of force dipole is exerted on each particle, as shown in Figure 2-7. Particles are placed off lattice, while forces are placed on lattice. The micro-swimmer particles are initially distributed randomly in the simulation cell without any overlap. The simulation cell is $50\,\delta \times 50\,\delta \times 100\,\delta$, where δ is the mesh grid size. The diameter (D) of the suspended mono-disperse spherical particles is $6\,\delta$, therefore the simulation cell is 8.33D × 8.33D ×16.67D Periodic boundary conditions are applied only to the flow direction. Periodic boundary condition is applied to the flow direction, while no-slip boundary conditions are applied to the rest of the four walls of the channel.

The time step size is 0.001τ, with τ being 1 simulation time unit.

Initially each particle is assigned a random orientation distribution, as shown by the arrows in Figure 2-7. The arrows in this work indicate the direction of forces applied on the surrounding fluid, which is also the direction of self-locomotion.

The pressure gradient that has been investigated in this work varies from 0.2 to 0.8. Two suspensions containing 10 and 50 micro-swimmer particles have been carried out, corresponding to volume fraction 0.45% and 2.26% respectively.

Both continuous and intermittent light source have been employed in the investigation of light effect. The interval of intermittence for switching on and off the light source is four times the internal response time of each micro-swimmer particle.

In simulation units, the viscosity of the suspending medium is given to be 1. The amplitude applied on the body is 10. The density of particle is the same as that of the medium, and is set to be 1.

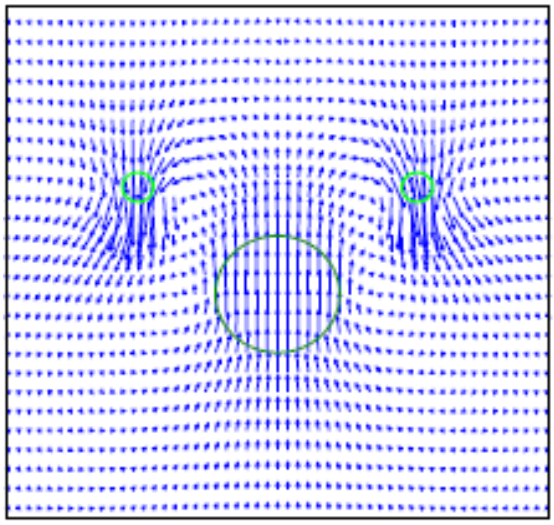

Figure 2-10 Velocity field around one micro-swimmer [67]

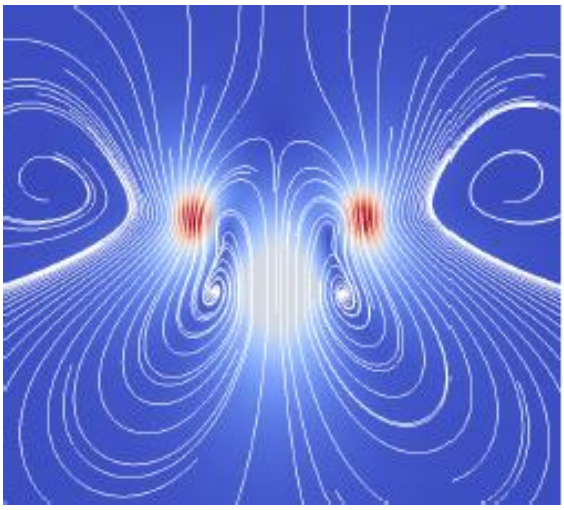

Figure 2-11 Streamlines around one micro-swimmer [67]

2.6 Evaluation of Properties

2.6.1 Lateral Cluster Size

To quantify the dynamic change associated with the suspension, we define the lateral direction cluster size as the product of average pair distance in x and y direction.

The average pair distance in x and y direction is defined as following:

$$\overline{x} = \frac{2}{N(N-1)} \sum_{i,j}^{N} \left| x_i - x_j \right|, i < j \tag{2-13}$$

$$\overline{y} = \frac{2}{N(N-1)} \sum_{i,j}^{N} \left| y_i - y_j \right|, i < j \tag{2-14}$$

Then the lateral cluster size is defined as:

$$Area = \overline{x} \times \overline{y} \tag{2-15}$$

Following the lateral cluster size definition, in this work, we further define lateral cluster width is defined as

$$\delta = \sqrt{Area} \tag{2-16}$$

For a fair comparison between experiments and simulation, we plot δ/D_p, with $D_p$being the diameter of the particle, against τ/τ_p.

2.6.2 Average number of clusters along flow direction

To quantify the flocculation and clustering effect along z-direction, a different method has been adopted to straightforwardly represent the local structure of the suspension.

Each bin has a size equal to 5δ, this value is comparable to the particle diameter. Therefore for a simulation cell with length equal to 100δ, there are 20 bins along the flow direction.

At each time step, the particles are binned accordingly into each bin based on their center-or-mass position. Hence, in this work, we define a cluster as regions containing consecutively non-zero binning. Therefore, the number of clusters are simply the number of non-zero binning zones.

We then average the data within every 500 timesteps, corresponding to every 50 τ.

2.6.3 Scaling and Dimensionless numbers

2.6.3.1 Scaling

The length scale in simulation is mapped back to experiments by matching the size of one single micro-alga whose typical size is 10 μm, with one simulation particle, whose size is 6 δ, with δ being the grid size, where $1\delta = 1.667\ \mu m$ The simulation is performed to have one particle placed in the center of the simulation channel with exposure to light only, and no pressure differential across the channel. Periodic boundary conditions are applied to the flow direction only.

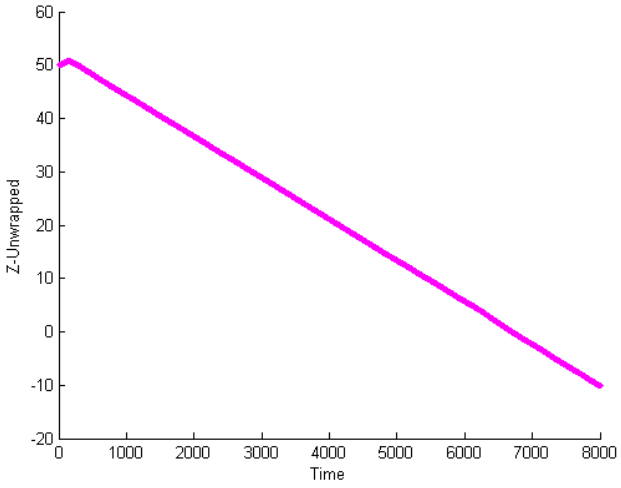

Figure 2-12 Single Particle Trace with only light exposure

The cell velocity in simulation is found to be 0.078 δ/τ, where τ is the simulation time unit. Hence, we found

$$1\tau = 0.0026 \text{ sec}$$

2.6.3.2 Dimensionless numbers

Based on the suspending medium viscosity and force amplitude exerted on the micro-swimmer, the swimming speed of micro-swimmer is found to be 0.0167. This results in a particle Reynolds number of 0.1.

$$Re^P = \frac{\rho v_p R}{\eta} \qquad 2\text{-}17$$

Based on the pressure gradient imposed on the fluid, and suspending medium of the fluid, channel Reynolds number for simulation and experiments at each pressure gradient or flow rates is tabulated as following:

$$Re^C = \frac{\rho \langle v \rangle D_H}{\eta} \qquad 2\text{-}18$$

where $< \boldsymbol{v} >$ being the mean velocity, $\boldsymbol{D_H}$ being hydraulic diameter; with the microchannel dimension being 1mm × 1 mm, $\boldsymbol{D_H}$ is 1mm.

Table 2-1 Simulation:Channel Reynolds number at each pressure gradient applied

Pressure Gradient	0.2	0.4	0.6	0.8
$\langle v \rangle$	0.176	0.351	0.527	0.702
Re^C	8.8	17.55	26.35	35.10

Table 2-2 Experiments: Channel Reynolds number at each flow rate applied

Flow Rate $(^{ml}/_{min})$	0.03	0.06	0.08	0.09
$\langle v \rangle\ (m/s)$	5×10^{-4}	1×10^{-3}	1.3×10^{-3}	1.5×10^{-3}
Re^C	5×10^{-7}	1×10^{-6}	1.3×10^{-6}	1.5×10^{-6}

To compare the results in each suspension in simulation and to compare simulation results to experiments, we hence introduce three groups of dimensionless number.

Without the presence of particles, the analytical solution for flow rate in a three dimensional rectangular channel is expressed as [78]

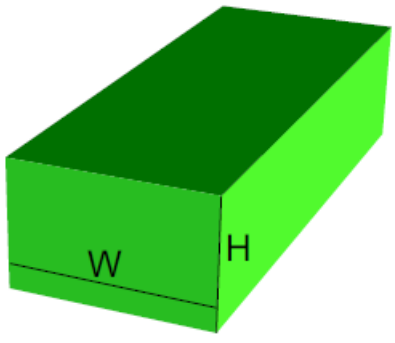

Figure 2-13 A rectangular pipe of width W and height H

$$Q = \frac{\nabla P}{12\eta}\rho W H^3 \left[1 - \sum_{n,odd}^{\infty} \frac{192}{\pi^5}\frac{H}{W}\frac{1}{n^5}\tanh\left(n\pi\frac{W}{2H}\right)\right] \quad 2\text{-}19$$

For a square channel, where W = H, the expression is then simplified as

$$Q = \frac{\nabla P}{12\eta}\rho H^4 \left[1 - \sum_{n,odd}^{\infty} \frac{192}{\pi^5}\frac{1}{n^5}\tanh(\frac{n\pi}{2})\right] \quad 2\text{-}20$$

For a square channel, mean fluid velocity is therefore

$$\langle v\rangle = \frac{Q}{H^2} \quad 2\text{-}21$$

Characteristic shear rate is therefore

$$\dot{\gamma} = \frac{\langle v\rangle}{\frac{H}{2}} \quad 2\text{-}22$$

D1 = characteristic shear rate × cell reorientation time = $\dot{\gamma}\tau_r$

D1 in simulation are tabulated as following

Table 2-3 D1 in simulation

Pressure Gradient	**0.2**	**0.4**	**0.6**	**0.8**
$\dot{\gamma}$	0.007	0.014	0.021	0.028
$\dot{\gamma}\tau_r$	0.35	0.7	1.05	1.4

The calculation for the series $\left[1 - \sum_{n,odd}^{\infty} \frac{192}{\pi^5}\frac{1}{n^5}\tanh(\frac{n\pi}{2})\right]$ converges when n $\leq$ 5 , resulting in a dimensionless number, which equals to 0.4218.

D1 in experiments are tabulated as following

Table 2-4 D1 in experiments

Flow Rate (ml/min)	**0.03**	**0.05**	**0.08**	**0.09**
$\dot{\gamma}$ (s^{-1})	1	1.67	2.5	3
$\dot{\gamma}\tau_r$	1	1.67	2.5	3

D2 = Mean fluid velocity / swimming velocity = $\frac{<v>}{v_p}$

Table 2-5 D2 in simulation

Pressure Gradient	**0.2**	**0.4**	**0.6**	**0.8**
$\langle v \rangle$	0.176	0.351	0.527	0.702
D2	10.539	21.018	31.556	42.035

Table 2-6 D2 in experiments

Flow rate (ml/min)	**0.03**	**0.05**	**0.08**	**0.09**
$\langle v \rangle$ ($\mu m/s$)	500	835	1250	1500
D2	10	16.7	25	30

D3 = Channel thickness/cell diameter = $\frac{H}{D}$

Table 2-7 D3 in comparison of experiment and simulation

	Experiment	**Simulation**
D3	20	8.3

In experiments, flow rate from 0.03 ml/min to 0.09 ml/min, corresponding to shear rate from 1 s to 3 s. Cell reorientation time in experiment is 1 s. Typical swimming velocity is 50 ± 20 $\mu m/s$

2.7 Results:

2.7.1 Particle Reynolds number and channel Reynolds number

2.7.2 Self-Focusing phenomenon and Instability

In order to validate the proposed model, we hence would like to reproduce the experimental findings.

Based on the current model, we are able to reproduce the self-focusing phenomenon. Moreover, we also discovered another phenomenon which has not yet been carried out from the experiments.

The snapshots demonstrate the two distinct dynamic states of a suspension containing 50 particles. Initially, the particles are randomly distributed in the simulation cell. Looking from the lateral direction, the cells cover a fairly large region in an overlapped fashion.After 1000 τ, a thin-long jet start to form along the center of the cell and the same time accompanied by shrinkage in cluster size in lateral direction, which stands for the self-focusing state. However, the formation of this thin-long jet is actually not a stable state, rather it breaks down into different clusters along the flow direction, and the clusters reform with each other due to hydrodynamic interaction, leading to a very dynamic clustering state.

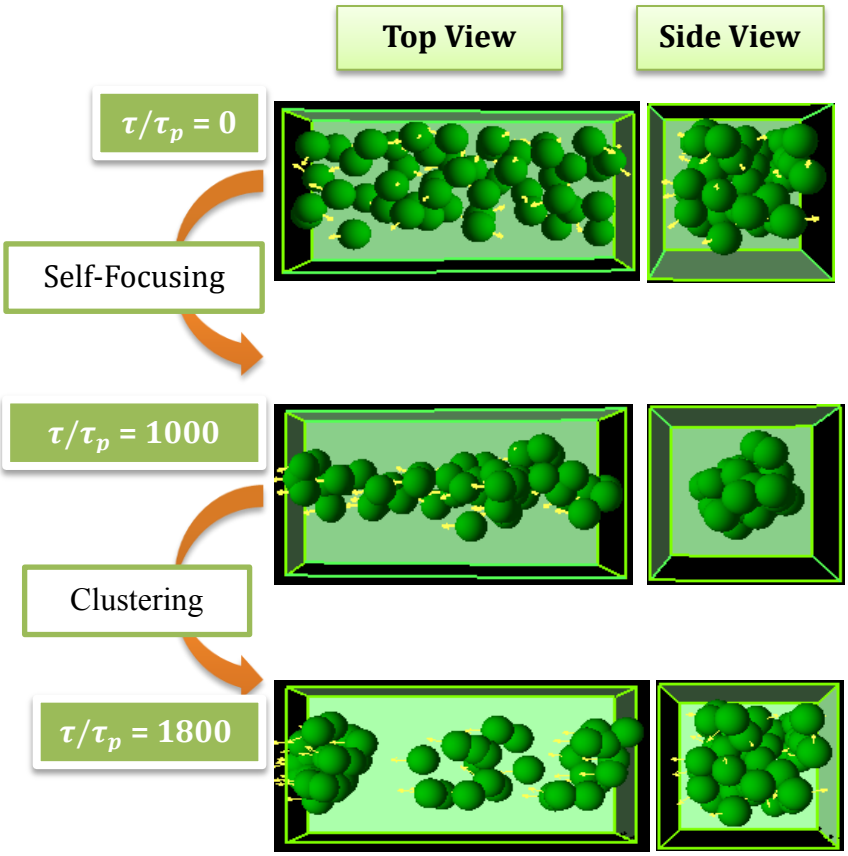

Figure 2-14 Self-focusing and clustering state of microswimmer suspension

In order to quantitatively analyze this phenomenon, we performed analysis of the lateral direction cluster size.

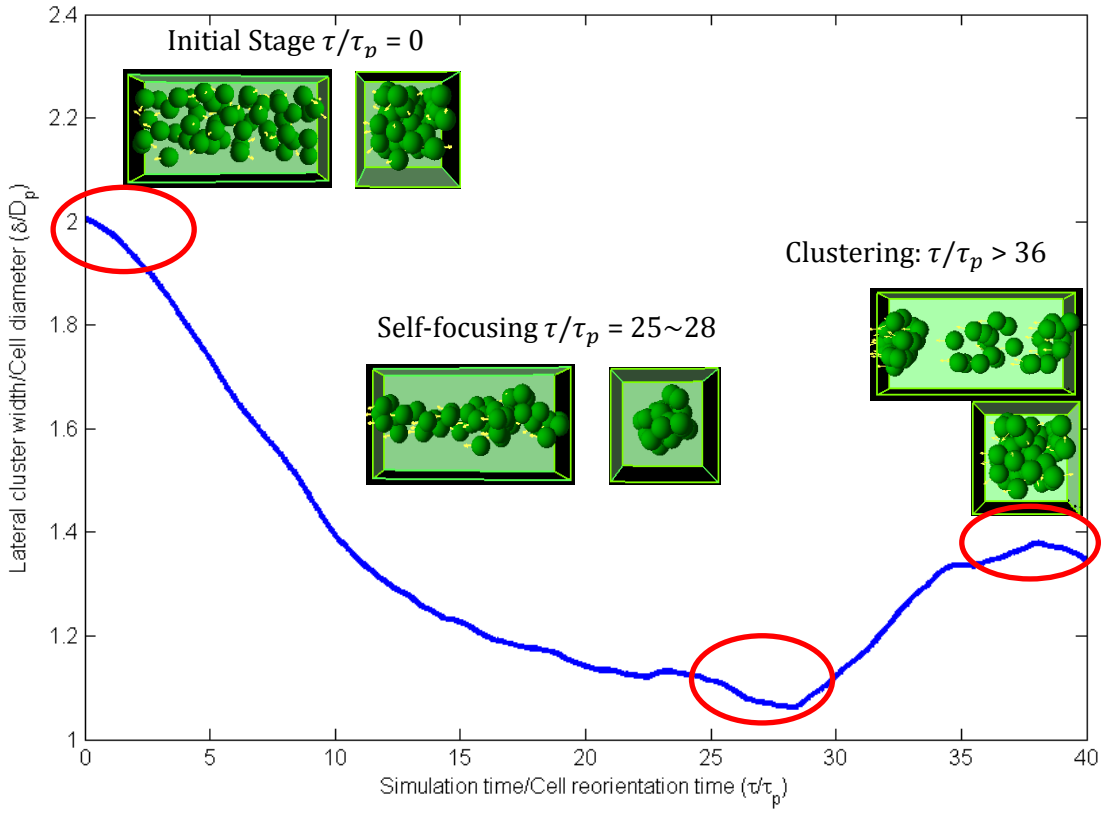

Figure 2-15 lateral direction cluster size

Nevertheless, from a quantitative point of view, the self-focusing state as well as the clustering state can be pinpointed as well.

Similarly, we can also quantify the dynamics by considering the number of clusters along the flow direction. The self-focusing state can be again pinpointed where on average there is one cluster, the thin long jet formed along the simulation cell; the clustering state on the other hand, can be identified by an average of three clusters along the simulation cell.

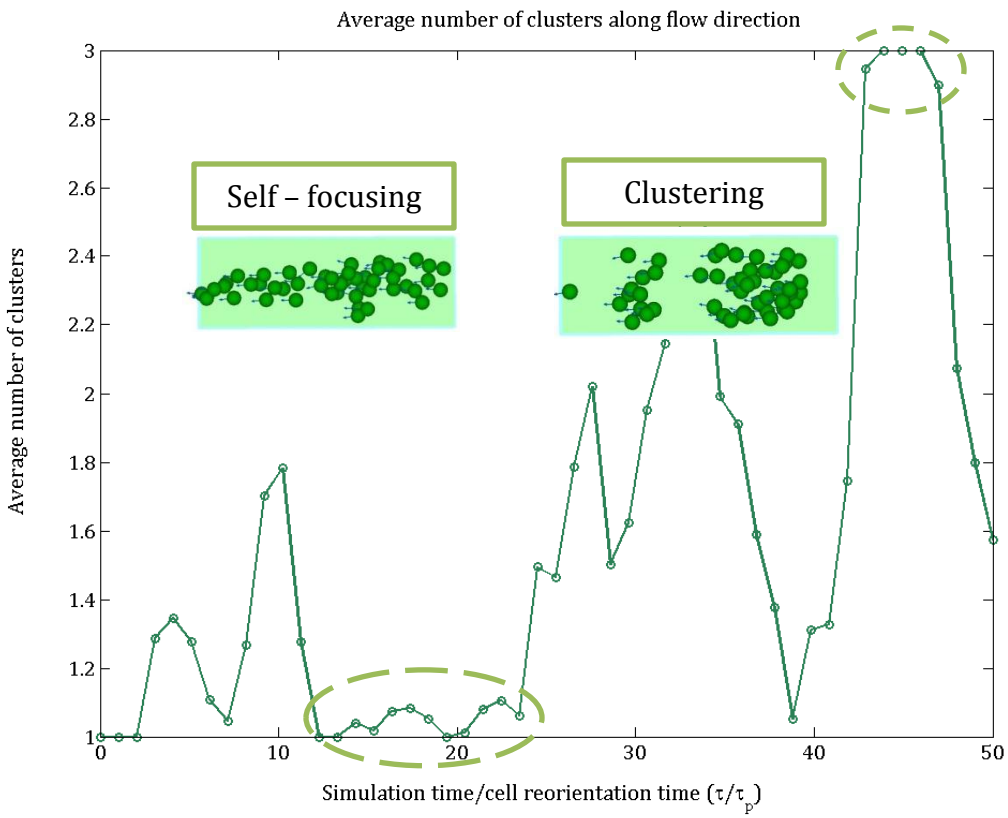

Figure 2-16 Average number of clusters along flow direction

As we can see from Table 2-1 and

Table 2-2 that channel Reynolds number in both simulation and experiments are small enough to give laminar single phase flow, and have little effect on the steady focusing state. Although hydrodynamic interactions between cells are considered primarily as the drive for the instability associated with clustering stage, the uneven density distribution in the clusters could also influence the instable dynamics during the dynamic process when clusters break and form.

2.7.3 Volume Fraction Effect

We investigated the effect of volume fraction on the dynamics of the particle suspension under exposure to both light and flow. Two systems, differing from each other by 1/5 of volume fraction have been carried out.

It can be found that both systems experienced the onset of self-focusing state at almost the same time, but the system with higher volume fraction showed richer dynamics in cluster formation. Over the same length scale, we observed more variations in clustering state at higher volume fraction. Since the cells interaction with each other through hydrodynamic interaction, a higher volume fraction would induce more pronounced effect in hydrodynamic interaction.

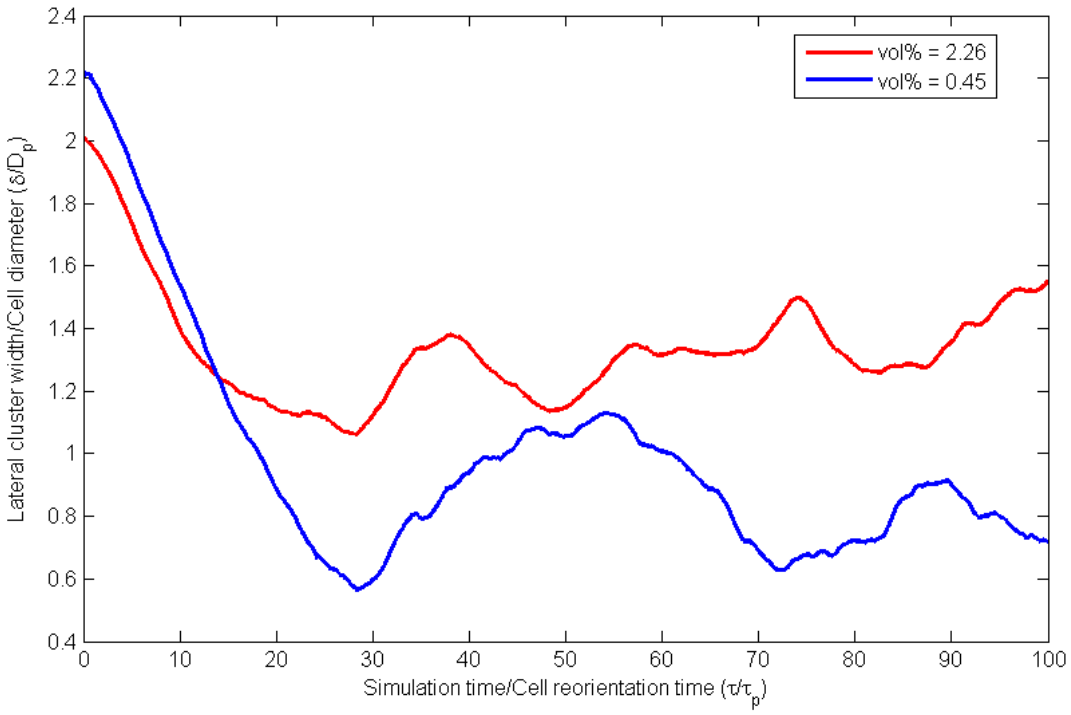

Figure 2-17 Volume fraction effect on self-focusing state and clustering state

2.7.4 Pressure Gradient Effect

If not the local flow vorticity induced by the Poiseuille flow, there would not be the self-focusing phenomenon. Hence, to further investigate what is the effect of pressure on the self-focusing state is of interest to both experiments and simulation.

Experimentally, the probability distribution function of cell distribution across the stream has been measured in a range of pressure gradient within which the self-focusing state is able to be

reached [68]. It is found experimentally the larger the pressure gradient the more distinct the self-focusing state is. The larger pressure gradient increases the probability for the particle to focus along the center of the flow.

Simulation wise, the pressure effect has been investigated on two systems with two volume fractions of particles by analyzing laterally the cluster size, where the decrement in the lateral cluster size indicates the onset of the self-focusing state, whereas the increment indicates the onset of clustering state.

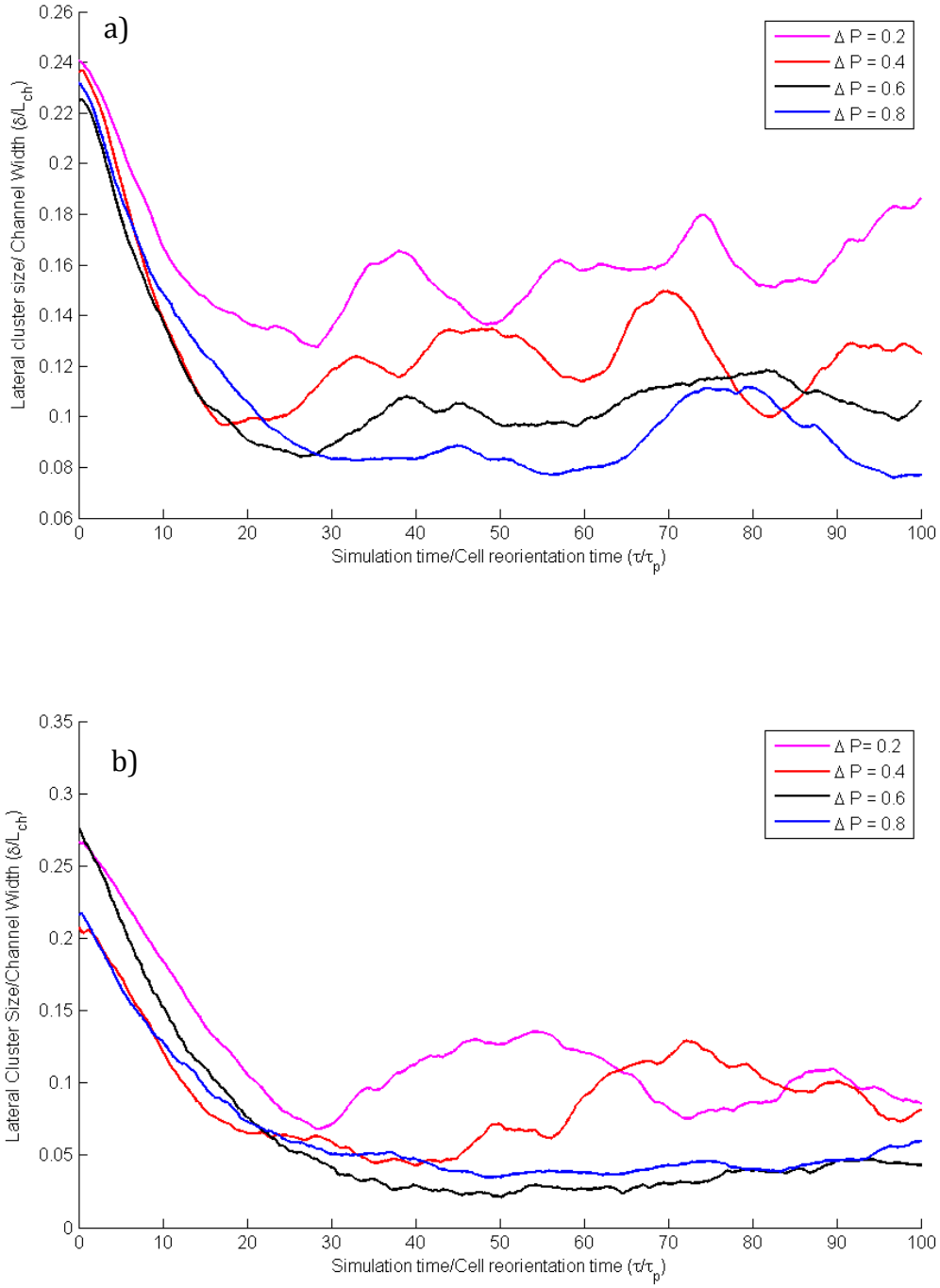

Figure 2-18 Pressure gradient effect on the dynamics of suspension of volume fraction a) 0.45% and b) 2.26%

It is found, regardless of the difference in volume fraction, that the self-focusing state is more stable under a higher pressure gradient, as shown in the plateau region. This fact is also in good agreement with experimental findings.

Meanwhile, the higher pressure gradient is found also as an 'inhibitor' for the clustering state, which is indicated by the peaks in the curves. The highest pressure gradient applied prolonged the self-focusing state while at the same time suppressed the breakage of this thin-long jet, indicating by the peaks in the curve.

We compare the dimensionless number D1 which is the product of characteristic shear rate produced by the flow and cell orientation time. In experiments, it is 1s, and in simulation, it is 50 τ.

In the reported experiment work, the flow rate range that is able to bring about the self-focusing phenomenon is from 0.03 ml/min to 0.09 ml/min, and the corresponding D1 ranges from 1 to 3, see Table 2-3and Table 2-4. However, in experimental results shown in the inlet in Figure 2-5, it is not clear whether there is actual self-focusing onset either from the flow rate 0.01 ml/min to 0.03 ml/min or from 0.10 ml/min to 0.13 ml/min.A more precise criterion for the stable self-focusing can be obtained from simulation study.

In simulation, the applied pressure gradient varies from 0.2 to 0.8, corresponding to D1 from 0.35 to 1.4. When D1 is at 0.35, corresponding to the lowest pressure gradient applied, one can see that the self-focusing stage lasts for only a short while, and then followed by an instable period of clustering forming. Comparing D1 at 0.35 situation to that when D1 at 1.05, one can see a much more stable self-focusing stage when D1 is 1.05.

However, currently there are no sufficient evidence to tell if the self-focusing stage would exist or not in simulation when the applied pressure gradient increases to even higher.

In addition, it is worth noticing that the dimensionless number D2, which is defined as ratio of mean fluid velocity to cell swimming velocity is comparable in both simulation and experiments.

2.7.5 Intermittent Light effect: reversible self-focusing phenomenon

The photo-tactic nature of this type of micro-swimmer plays a critical role on this interesting self-focusing phenomenon, as it is the origin which has caused the biased swimming motion toward the direction of light, and hence increased the higher probability of its existence around the center of flow.

A better understanding on the light effect of the flow behavior of the micro-algae suspension will no doubt lead to a better control of this suspension. In the experiments, an intermittent light source is in place of a continuous light source, and the on-off interval of this intermittent light source is about 5 times of the internal response time of the micro-swimmer to the light.

Interestingly, within the flow rate range for self-focusing state to take place, it is also found the self-focusing state presents a reversible nature, as shown clearly by this saw-tooth pattern.

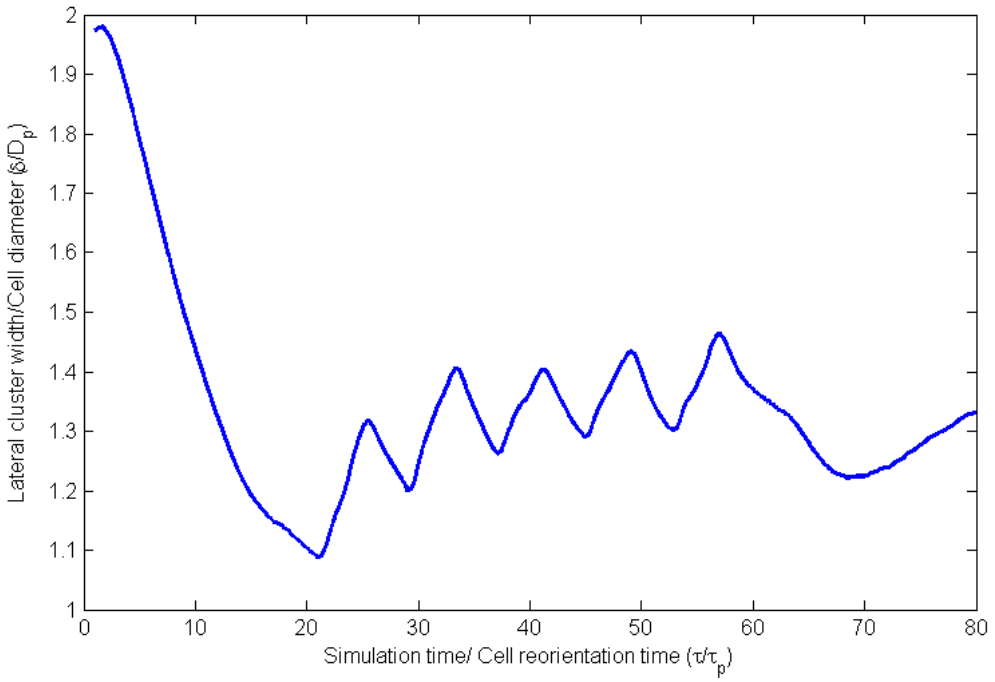

Figure 2-19 Simulation: saw-tooth pattern

Qualitatively, the same saw-tooth pattern can also be reproduced from the simulation based on our model. The light is turned off at the point when the self-focusing state is approaching a steady-state, roughlywhen $\frac{\tau}{\tau_p} = 20$, and the intermittent interval is 4 times the micro-swimmers' internal response time. In experiments, the light interval is 5 times the cells' reorientation time.

To further quantitatively compare simulation results to experimental evidence, we compare the ratio $d(h)/(v_c * t_{switch})$ in both simulation and experiments, where d(h) being the amplitude of saw-tooth pattern.

When the bias in orientation is the same, indicating by $\gamma\tau_{\mathrm{ori}}$, then the distance moved under this bias should also be comparable.

In the work, $\gamma\tau_{\mathrm{ori}}$ in experiment is about 6 times larger than simulation value, while the distance moved is about 10 times larger than the simulation. It could be due to several reasons:

1) The volume fraction studied in simulation is much higher than that in the experiments – higher volume fraction introduces more drastic hydrodynamic interaction between the cells, which could possibly retard the motion of the swimming cells.
2) In simulation, the light switch time is only 5 times the cell reorientation time rather being five times, therefore reducing the time for cells to travel across streamlines.
3) The channel width to cell diameter in simulation is about 2.5 times larger than that in simulation, this might reduce the effect of confinement effect on the cell motion.

2.8 Future Perspective

The mechanisms govern this interesting and complex dynamics involve with multiple factors intertwined together: self-motility of the micro-swimmers, hydrodynamic interaction induced by the swimming pattern, the combination of flow effect and biased swimming direction induced by light. To elucidate the mechanisms, experiment studies need to be designed to single out the factors. An ongoing study design currently introduces zero-vorticity environment by introducing a plug flow. Then the

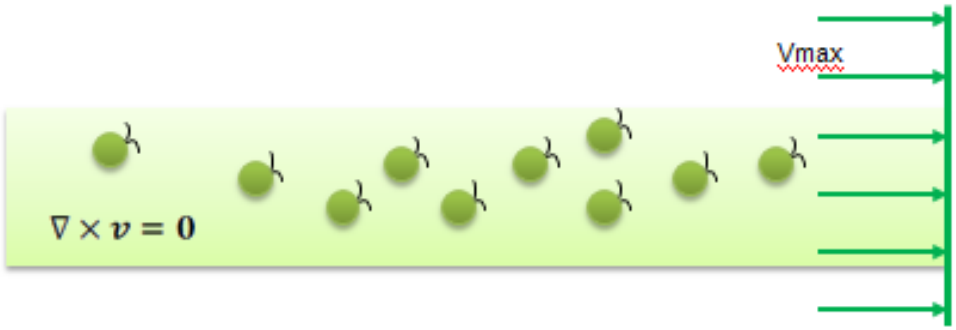

Figure 2-20 Schematic drawing of introducing plug flow to isolate swimming motility from flow vorticity

hydrodynamic interaction of microswimmers under purely light effect is being studied. Simulation wise, heuristic tests have been carried out to study instability by designing two scenarios, one with initial equal particle distribution, and the other with unequal distribution by introducing a slight shift.

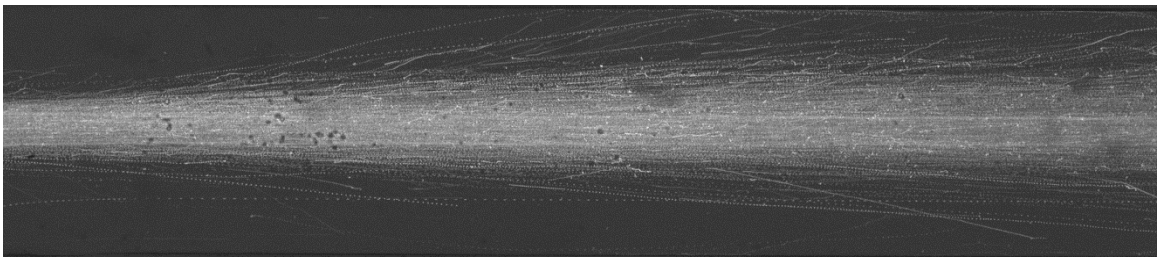

Figure 2-21 Hydrodynamic diffusion of algae suspension undergoing a plug flow

Preliminary results from experiments are shown here for observation of hydrodynamic diffusion.

END

REFERENCES

1. Madivala, B., Fransaer, J. & Vermant, J. Self-Assembly and Rheology of Ellipsoidal Particles at Interfaces. *Langmuir* **25,** 2718–2728 (2009).

2. Glotzer, S. C., Solomon, M. J. & Kotov, N. A. Self-assembly: From nanoscale to microscale colloids. *AIChE J.* **50,** 2978–2985 (2004).

3. Grzelczak, M., Vermant, J., Furst, E. M. & Liz-Marzán, L. M. Directed Self-Assembly of Nanoparticles. *ACS Nano* **4,** 3591–3605 (2010).

4. Nikoobakht, B., Wang, Z. L. & El-Sayed, M. A. Self-Assembly of Gold Nanorods. *J. Phys. Chem. B* **104,** 8635–8640 (2000).

5. Fu, S.-Y., Lauke, B., Mäder, E., Yue, C.-Y. & Hu, X. Tensile properties of short-glass-fiber- and short-carbon-fiber-reinforced polypropylene composites. *Compos. Part A Appl. Sci. Manuf.* **31,** 1117–1125 (2000).

6. Drzaic, P. S. *Liquid crystal dispersions*. **1220282863,** (World Scientific Singapore, 1995).

7. Huynh, W. U., Dittmer, J. J. & Alivisatos, A. P. Hybrid Nanorod-Polymer Solar Cells. *Science (80-.).* **295,** 2425–2427 (2002).

8. Jin, Y., Wang, J., Sun, B., Blakesley, J. C. & Greenham, N. C. Solution-Processed Ultraviolet Photodetectors Based on Colloidal ZnO Nanoparticles. *Nano Lett.* **8,** 1649–1653 (2008).

9. Kim, H.-M., Kang, T. W. & Chung, K. S. Nanoscale Ultraviolet-Light-Emitting Diodes Using Wide-Bandgap Gallium Nitride Nanorods. *Adv. Mater.* **15,** 567–569 (2003).

10. Yi, G.-C., Wang, C. & Park, W. Il. ZnO nanorods: synthesis, characterization and applications. *Semicond. Sci. Technol.* **20,** S22 (2005).

11. Bricker, J. M., Park, H.-O. & Butler, J. E. Rheology of semidilute suspensions of rigid polystyrene ellipsoids at high Peclet numbers. *J. Rheol. (N. Y. N. Y).* **52,** 941 (2008).

12. Hinch, B. E. J. & Leal, L. G. The effect of Brownian motion on the rheological properties of a suspension of non-spherical particles. **62,** 683–712 (1972).

13. Jeffery, G. B. The motion of ellipsoidal particles immersed in a viscous fluid. *Proc. R. Soc. London. Ser. A, Contain. Pap. a Math. Phys. Character* **102,** 161–179 (1922).

14. Boek, E. S., Coveney, P. V, Lekkerkerker, H. N. W. & van der Schoot, P. Simulating the rheology of dense colloidal suspensions using dissipative particle dynamics. *Phys. Rev. E* **55,** 3124 (1997).

15. Phung, T. N., Brady, J. F. & Bossis, G. Stokesian dynamics simulation of Brownian suspensions. *J. Fluid Mech.* **313,** 181–207 (1996).

16. Meng, Q. & Higdon, J. J. L. Large scale dynamic simulation of plate-like particle suspensions. Part I: Non-Brownian simulation. *J. Rheol. (N. Y. N. Y).* **52,** 1 (2008).

17. Foss, D. R. & Brady, J. F. Structure, diffusion and rheology of Brownian suspensions by Stokesian dynamics simulation. *J. Fluid Mech.* **407,** 167–200 (2000).

18. Iso, Y., Cohen, C. & Koch, D. L. Orientation in simple shear flow of semi-dilute fiber suspensions 2. Highly elastic fluids. *J. Nonnewton. Fluid Mech.* **62,** 135–153 (1996).

19. Stover, C. A., Koch, D. L. & Cohen, C. Observations of fibre orientation in simple shear flow of semi-dilute suspensions. *J. Fluid Mech* **238,** 277–296 (1992).

20. Petrich, M. P., Koch, D. L. & Cohen, C. An experimental determination of the stress–microstructure relationship in semi-concentrated fiber suspensions. *J. Nonnewton. Fluid Mech.* **95,** 101–133 (2000).

21. Claeyst, L., Ewald, T. & Fluid-particle, I. Suspensions of prolate spheroids in Stokes flow . Part 2 . Statistically homogeneous dispersions. **251,** (1993).

22. Cheng, X., McCoy, J. H., Israelachvili, J. N. & Cohen, I. Imaging the microscopic structure of shear thinning and thickening colloidal suspensions. *Science (80-.).* **333,** 1276–1279 (2011).

23. Meng, Q. & Higdon, J. J. L. Large scale dynamic simulation of plate-like particle suspensions. Part II: Brownian simulation. *J. Rheol. (N. Y. N. Y).* **52,** 37 (2008).

24. in't Veld, P. J., Petersen, M. K. & Grest, G. S. Shear thinning of nanoparticle suspensions. *Phys. Rev. E* **79,** (2009).

25. Kalra, V., Escobedo, F. & Joo, Y. L. Effect of shear on nanoparticle dispersion in polymer melts: A coarse-grained molecular dynamics study. *J. Chem. Phys.* **132,** 024901 (2010).

26. Okagawa, A., Cox, R. G. & Mason, S. G. The kinetics of flowing dispersions. VI. Transient orientation and rheological phenomena of rods and discs in shear flow. *J. Colloid Interface Sci.* **45,** 303–329 (1973).

27. Leal, L. G. & Hinch, E. J. The effect of weak Brownian rotations on particles in shear flow. *J. Fluid Mech.* **46,** 685 (2006).

28. Hinch, E. J. & Leal, L. G. Time-dependent shear flows of a suspension of particles with weak Brownian rotations. *J. Fluid Mech.* **57,** 753 (2006).

29. Jogun, S. M. & Zukoski, C. F. Rheology and microstructure of dense suspensions of plate-shaped colloidal particles. *J. Rheol. (N. Y. N. Y).* **43,** 847 (1999).

30. Varadan, P. & Solomon, M. J. Direct visualization of flow-induced microstructure in dense colloidal gels by confocal laser scanning microscopy. *J. Rheol.* **47,** (2003).

31. Biehl, R. & Palberg, T. Modes of motion in a confined colloidal suspension under shear. *EPL (Europhysics Lett.* **66,** 291 (2004).

32. Xu, X., Rice, S. a & Dinner, A. R. Relation between ordering and shear thinning in colloidal suspensions. *Proc. Natl. Acad. Sci. U. S. A.* **110,** 3771–6 (2013).

33. Foss, D. R. & Brady, J. F. Brownian Dynamics simulation of hard-sphere colloidal dispersions. *J. Rheol. (N. Y. N. Y).* **44,** 629 (2000).

34. Claeys, I. L. & Brady, J. F. Suspensions of prolate spheroids in Stokes flow. Part 1. Dynamics of a finite number of particles in an unbounded fluid. *J. Fluid Mech.* **251,** 411–442 (1993).

35. Yamane, Y., Kaneda, Y. & Dio, M. Numerical simulation of semi-dilute suspensions of rodlike particles in shear flow. *J. Nonnewton. Fluid Mech.* **54,** 405–421 (1994).

36. Yamamoto, S. & Matsuoka, T. Viscosity of dilute suspensions of rodlike particles: A numerical simulation method. *J. Chem. Phys.* **100,** (1994).

37. Löwen, H. Brownian dynamics of hard spherocylinders. *Phys. Rev. E* **50,** 1232–1242 (1994).

38. Plimpton, S. Fast Parallel Algorithms for Short-Range Molecular Dynamics. *J. Comput. Phys.* **117,** 1–19 (1995).

39. Marrink, S. J., de Vries, A. H. & Mark, A. E. Coarse Grained Model for Semiquantitative Lipid Simulations. *J. Phys. Chem. B* **108,** 750–760 (2004).

40. GAY, J. G. & BERNE, B. J. MODIFICATION OF THE OVERLAP POTENTIAL TO MIMIC A LINEAR SITE-SITE POTENTIAL. *J. Chem. Phys.* **74,** 3316–3319 (1981).

41. Groot, R. D. & Warren, P. B. Dissipative particle dynamics: Bridging the gap between atomistic and mesoscopic simulation. *J. Chem. Phys.* **107,** 4423 (1997).

42. Soddemann, T., Dünweg, B. & Kremer, K. Dissipative particle dynamics: A useful thermostat for equilibrium and nonequilibrium molecular dynamics simulations. *Phys. Rev. E* **68,** 46702 (2003).

43. Español, P. & Warren, P. Statistical Mechanics of Dissipative Particle Dynamics. *EPL (Europhysics Lett.* **30,** 191 (1995).

44. Tirado, M. M., Martínez, C. L. & de la Torre, J. G. Comparison of theories for the translational and rotational diffusion coefficients of rod-like macromolecules. Application to short DNA fragments. *J. Chem. Phys.* **81,** (1984).

45. Ganani, E. & Powell, R. L. Rheological Properties of Rodlike Particles in a Newtonian and a Non-Newtonian Fluid. *J. Rheol.* **30,** (1986).

46. Brenner, H. Rheology of a dilute suspension of axisymmetric Brownian particles. *Int. J. Multiph. flow* **1,** 195–341 (1974).

47. Claeys, I. L. & Brady, J. F. Suspensions of prolate spheroids in Stokes flow. Part 2. Statistically homogeneous dispersions. *J. Fluid Mech.* **251,** 443–477 (1993).

48. Goyal, S. & Escobedo, F. A. Structure and transport properties of polymer grafted nanoparticles. *J. Chem. Phys.* **135,** 184902 (2011).

49. Dreyfus, R. *et al.* Microscopic artificial swimmers. *Nature* **437,** 862–865 (2005).

50. Keaveny, E. E. & Maxey, M. R. Spiral swimming of an artificial micro-swimmer. *J. Fluid Mech.* **598,** 293–319 (2008).

51. Ogrin, F. Y., Petrov, P. G. & Winlove, C. P. Ferromagnetic microswimmers. *Phys. Rev. Lett.* **100,** (2008).

52. Hatwalne, Y., Ramaswamy, S., Rao, M. & Simha, R. A. Rheology of active-particle suspensions. *Phys. Rev. Lett.* **92,** (2004).

53. PURCELL, E. M. LIFE AT LOW REYNOLDS-NUMBER. *Am. J. Phys.* **45,** 3–11 (1977).

54. BRENNEN, C. & WINET, H. FLUID-MECHANICS OF PROPULSION BY CILIA AND FLAGELLA. *Annu. Rev. Fluid Mech.* **9,** 339–398 (1977).

55. Kim, M. J. & Breuer, K. S. Use of bacterial carpets to enhance mixing in microfluidic systems. *J. FLUIDS Eng. ASME* **129,** 319–324 (2007).

56. Dombrowski, C., Cisneros, L., Chatkaew, S., Goldstein, R. E. & Kessler, J. O. Self-concentration and large-scale coherence in bacterial dynamics. *Phys. Rev. Lett.* **93,** (2004).

57. Darnton, N., Turner, L., Breuer, K. & Berg, H. C. Moving fluid with bacterial carpets. *Biophys. J.* **86,** 1863–1870 (2004).

58. Durham, W. M., Kessler, J. O. & Stocker, R. Disruption of Vertical Motility by Shear Triggers Formation of Thin Phytoplankton Layers. *Science (80-.).* **323,** 1067–1070 (2009).

59. Parsek, M. R. & Singh, P. K. Bacterial biofilms: An emerging link to disease pathogenesis. *Annu. Rev. Microbiol.* **57,** 677–701 (2003).

60. Rafai, S., Jibuti, L. & Peyla, P. Effective Viscosity of Microswimmer Suspensions. *Phys. Rev. Lett.* **104,** (2010).

61. Sokolov, A. & Aranson, I. S. Reduction of Viscosity in Suspension of Swimming Bacteria. *Phys. Rev. Lett.* **103,** (2009).

62. Soni, G. V, Ali, B. M. J., Hatwaine, Y. & Shivashankar, G. V. Single particle tracking of correlated bacterial dynamics. *Biophys. J.* **84,** 2634–2637 (2003).

63. Underhill, P. T., Hernandez-Ortiz, J. P. & Graham, M. D. Diffusion and spatial correlations in suspensions of swimming particles. *Phys. Rev. Lett.* **100,** (2008).

64. Garcia, M., Berti, S., Peyla, P. & Rafai, S. Random walk of a swimmer in a low-Reynolds-number medium. *Phys. Rev. E* **83,** (2011).

65. Vincent, R. V & Hill, N. A. Bioconvection in a suspension of phototactic algae. *J. Fluid Mech.* **327,** 343–371 (1996).

66. Torney, C. & Neufeld, Z. Phototactic clustering of swimming microorganisms in a turbulent velocity field. *Phys. Rev. Lett.* **101,** (2008).

67. Jibuti, L. Locomotion et écoulements dans les fluides complexes confinés. (2011).

68. Garcia, X., Rafaï, S. & Peyla, P. Light Control of the Flow of Phototactic Microswimmer Suspensions. *Phys. Rev. Lett.* **110,** 138106 (2013).

69. Taylor, P. & Kessler, J. O. phenomena of swimming micro- organisms. 37–41

70. ERMAK, D. L. & MCCAMMON, J. A. BROWNIAN DYNAMICS WITH HYDRODYNAMIC INTERACTIONS. *J. Chem. Phys.* **69,** 1352–1360 (1978).

71. PHILLIPS, R. J., BRADY, J. F. & BOSSIS, G. HYDRODYNAMIC TRANSPORT-PROPERTIES OF HARD-SPHERE DISPERSIONS .1. SUSPENSIONS OF FREELY MOBILE PARTICLES. *Phys. FLUIDS* **31,** 3462–3472 (1988).

72. Kromkamp, J., van den Ende, D., Kandhai, D., van der Sman, R. & Boom, R. Lattice Boltzmann simulation of 2D and 3D non-Brownian suspensions in Couette flow. *Chem. Eng. Sci.* **61,** 858–873 (2006).

73. Tanaka, H. & Araki, T. Simulation method of colloidal suspensions with hydrodynamic interactions: Fluid particle dynamics. *Phys. Rev. Lett.* **85,** 1338–1341 (2000).

74. Davit, Y. & Peyla, P. Intriguing viscosity effects in confined suspensions: A numerical study. *EPL* **83,** (2008).

75. Peyla, P. Rheology and dynamics of a deformable object in a microfluidic configuration: A numerical study. *EPL* **80,** (2007).

76. Maury, B. NUMERICAL ANALYSIS OF A FINITE ELEMENT/VOLUME PENALTY METHOD. *SIAM J. Numer. Anal.* **47,** 1126–1148 (2009).

77. Chorin, A. J. Numerical Solution of the Navier-Stokes Equations. *Math. Comput.* **22,** 745 (1968).

78. Azzouz, H. The dependence of the cross-sectional shape on the hydraulic resistance of microchannels. (2004).